THE MINISTRY OF SCIENCE AND HIGHER EDUCATION OF THE RUSSIAN FEDERATION

ST. PETERSBURG STATE POLYTECHNICAL UNIVERSITY

JOURNAL

Physics and Mathematics

VOLUME 15, No.1, 2022

Peter the Great St. Petersburg
Polytechnic University
2022

ST. PETERSBURG STATE POLYTECHNICAL UNIVERSITY JOURNAL. PHYSICS AND MATHEMATICS

The journal is included in the List of leading peer-reviewed scientific journals and other editions to publish major findings of theses for the research degrees of Doctor of Sciences and Candidate of Sciences.

The publications are presented in the VINITI RAS Abstract Journal and Ulrich's Periodical Directory International Database.

The journal is published since 2008 as part of the periodical edition 'Nauchno-tekhnicheskie vedomosti SPb-GPU'.

The journal is registered with the Federal Service for Supervision in the Sphere of Telecom, Information Technologies and Mass Communications (ROSKOMNADZOR). Certificate ПИ № ФС77-52144 issued December 11, 2012.

The journal is distributed through the CIS countries catalogue, the «Press of Russia» joint catalogue and the «Press by subscription» Internet catalogue. The subscription index is **71823.**

The journal is in the **Web of Science** (Emerging Sources Citation Index), **Scopus**, the **Russian Science Citation Index** (RSCI) and the **Directory of Open Access Journals** (DOAJ) databases.

© Scientific Electronic Library (http://www.elibrary.ru).

Address: 195251 Politekhnicheskaya St. 29, St. Petersburg, Russia.

Phone: (812) 294-22-85.
http://ntv.spbstu.ru/physics

МИНИСТЕРСТВО НАУКИ И ВЫСШЕГО ОБРАЗОВАНИЯ РОССИЙСКОЙ ФЕДЕРАЦИИ

НАУЧНО-ТЕХНИЧЕСКИЕ ВЕДОМОСТИ

САНКТ-ПЕТЕРБУРГСКОГО ГОСУДАРСТВЕННОГО ПОЛИТЕХНИЧЕСКОГО УНИВЕРСИТЕТА

Физико-математические науки

ТОМ 15, №1

2022

Санкт-Петербургский политехнический
университет Петра Великого
2022

НАУЧНО-ТЕХНИЧЕСКИЕ ВЕДОМОСТИ САНКТ-ПЕТЕРБУРГСКОГО ГОСУДАРСТВЕННОГО ПОЛИТЕХНИЧЕСКОГО УНИВЕРСИТЕТА. ФИЗИКО-МАТЕМАТИЧЕСКИЕ НАУКИ

Журнал с 2002 г. входит в Перечень ведущих рецензируемых научных журналов и изданий, в которых должны быть опубликованы основные результаты диссертаций на соискание ученых степеней доктора и кандидата наук.

Сведения о публикациях представлены в Реферативном журнале ВИНИТИ РАН, в международной справочной системе «Ulrich's Periodical Directory».

С 2008 года выпускается в составе сериального периодического издания «Научно-технические ведомости СПбГПУ».

Журнал зарегистрирован Федеральной службой по надзору в сфере информационных технологий и массовых коммуникаций (Роскомнадзор). Свидетельство о регистрации ПИ № ФС77-52144 от 11 декабря 2012 г.

Распространяется по Каталогу стран СНГ, Объединенному каталогу «Пресса России» и по Интернет-каталогу «Пресса по подписке». Подписной индекс **71823**.

Журнал индексируется в базе данных **Web of Science** (Emerging Sources Citation Index), **Scopus**, а также включен в базы данных **«Российский индекс научного цитирования»** (РИНЦ), размещенную на платформе Научной электронной библиотеки на сайте http://www.elibrary.ru, и **«Directory of Open Access Journals»** (DOAJ)

Адрес редакции и издательства:
Россия, 195251, Санкт-Петербург, ул. Политехническая, д. 29.
Тел. редакции (812) 294-22-85.
http://ntv.spbstu.ru/physics

Contents

Содержание

Original article
DOI: https://doi.org/10.18721/JPM.15101

DIELECTRIC PROPERTIES OF THE POTASSIUM NITRATE – CAESIUM NITRATE FERROELECTRIC COMPOSITE

S. V. Baryshnikov [1], *A. Yu. Milinskiy* [1], *E. V. Stukova* [2] ✉, *A. A. Zeeva* [2]

[1] Blagoveshchensk State Pedagogical University, Blagoveshchensk, Russia;

[2] Amur State University, Blagoveshchensk, Russia

✉ lenast@bk.ru

Abstract: Some samples of the $(KNO_3)_{1-x}/(CsNO_3)_x$ composite with different x values have been prepared, and their temperature dependences of the differential thermal analysis signal, of the dielectric constant, and the amplitude of the third harmonic (to find an existence domain of the polar phase) were studied. The sample surfaces were investigated by scanning electron microscopy. An increase in the proportion of $CsNO_3$ was revealed to lead to a decrease in the coefficient of nonlinearity of the composite and to narrowing of the existence domain's temperature range of the KNO_3 ferroelectric phase III. Also it was found that the composite properties nonlinearity at x beyond 0.5 was determined by the $CsNO_3$ properties.

Keywords: composite, ferroelectric, permittivity, third harmonic coefficient, phase transition

Citation: Baryshnikov S. V., Milinskiy A. Yu., Stukova E. V., Zeeva A. A., Dielectric properties of the potassium nitrate − caesium nitrate ferroelectric composite, St. Petersburg Polytechnical State University Journal. Physics and Mathematics. 15 (1) (2022) 7–15. DOI: https://doi.org/10.18721/JPM.15101

Научная статья
УДК 537.226
DOI: https://doi.org/10.18721/JPM.15101

ДИЭЛЕКТРИЧЕСКИЕ СВОЙСТВА СЕГНЕТОЭЛЕКТРИЧЕСКОГО КОМПОЗИТА НИТРАТ КАЛИЯ – НИТРАТ ЦЕЗИЯ

С. В. Барышников [1], *А. Ю. Милинский* [1], *Е. В. Стукова* [2] ✉, *А. А. Зеева* [2]

[1] Благовещенский государственный педагогический университет, г. Благовещенск, Россия;

[2] Амурский государственный университет, г. Благовещенск, Россия;

✉ lenast@bk.ru

Аннотация. Изготовлены образцы композита $(KNO_3)_{1-x}/(CsNO_3)_x$, и для них исследованы температурные зависимости сигнала дифференциального термического анализа, диэлектрической проницаемости и амплитуды третьей гармоники (для определения области существования полярной фазы). Поверхности образцов изучались методом растровой электронной микроскопии. Обнаружено, что увеличение доли $CsNO_3$ приводит как к уменьшению коэффициента нелинейности композита, так и к сужению температурной области существования III сегнетоэлектрической фазы нитрата калия. Установлено, что при значениях x свыше 0,5 нелинейность свойств композита $(KNO_3)_{1-x}/(CsNO_3)_x$ определяется характеристиками $CsNO_3$.

Ключевые слова: композит, сегнетоэлектрик, диэлектрическая проницаемость, коэффициент третьей гармоники, фазовый переход

Для цитирования: Барышников С. В., Милинский А. Ю., Стукова Е. В., Зеева А. А. Диэлектрические свойства сегнетоэлектрического композита нитрат калия – нитрат цезия // Научно-технические ведомости СПбГПУ. Физико-математические науки. 2022. Т. 15. № 1. С. 7–15. DOI: https://doi.org/10.18721/ JPM.15101

Introduction

Potassium nitrate (KNO_3) is characterized by a rectangular hysteresis loop, low dielectric losses and relatively high spontaneous polarization, making this material promising for non-volatile memory cells [1]. The polar phase in potassium nitrate is only stable under cooling from 397 to 373 K. The ferroelectric state of this compound is metastable, allowing to adjust its temperature range by modifying different external factors. Previous studies confirmed this possibility by synthesizing solid solutions and composite, based on potassium nitrate [2–5]. For example, it was found for ferroelectric $(KNO_3)_{(1-x)}/(BaTiO_3)_x$ [2] and $(KNO_3)_{(1-x)}/(KNbO_3)_x$ [3] composites that the temperature range, where the ferroelectric phase of potassium nitrate existed, extended, which could be explained by dipole-dipole interaction of particles. In addition, the ferroelectric phase in KNO_3, contained in the composites, can be affected by the volume fraction of inclusion particles, their sizes, spontaneous polarization, etc. An expansion of the domain where the ferroelectric phase exists in KNO_3 was also observed upon doping with sodium ions (Na^+) [4, 5].

In this paper we consider the influence of inclusion particles of cesium nitrate ($CsNO_3$) on the formation of the ferroelectric state in potassium nitrate (KNO_3) making up the $(KNO_3)_{1-x}/(CsNO_3)_x$ composite.

Samples and experimental procedure

KNO_3 has an orthorhombic space group *Pmcn* [6] (phase II) at about 300 K. Potassium nitrate undergoes a transition to trigonal structure $R\bar{3}m$ (phase I) upon cooling to 401 K. Phases I and II are paraelectric. The ferroelectric trigonal phase III of potassium nitrate only emerges upon cooling in the range of 397–373 K. The maximum value of spontaneous polarization in the ferroelectric phase is 8–10 μC/cm² [6]. The temperature range where the ferroelectric phase exists in potassium nitrate depends on the maximum heating temperature and the cooling rate [7, 8]. For example, the polar phase range is 22–24 degrees for a polycrystalline KNO_3 sample heated to 473 K with a cooling rate of 1–2 K/min.

Cesium nitrate ($CsNO_3$) has trigonal symmetry at about 300 K. The cesium atoms form a pseudocubic sublattice with nine pseudocubes per unit cell. The crystal structure of the low-temperature phase was determined to be polar trigonal [9] with spontaneous polarization P_s equal to 1–2 μK/cm² (at 410–420 K) [10]. $CsNO_3$ has a cubic structure above the Curie temperature (T_C = 427 K).

We used KNO_3 and $CsNO_3$ powders to obtain $(KNO_3)_{1-x}/(CsNO_3)_x$ composites. The average particle size in the powders was 5–10 μm. The volume fraction of cesium nitrate in the composites was x = 0, 0.1, 0.2, 0.3, and 0.5. Powders of potassium and cesium nitrates were mixed in an agate mortar for about 30 min. The obtained powders were then pressed at $8 \cdot 10^3$ kg/cm² to produce disk-shaped samples 10 mm in diameter and 1.5 mm thick.

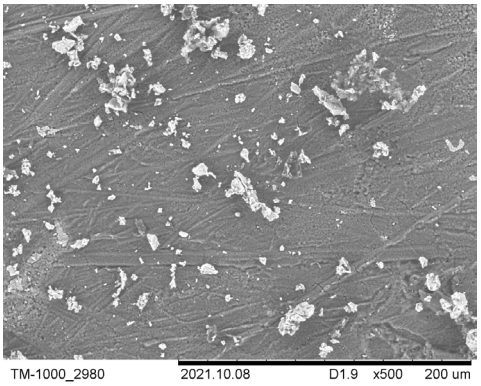

Fig. 1. Surface micrograph of $(KNO_3)_{0.8}/(CsNO_3)_{0.2}$ composite

An E7-25 meter was used to study the dielectric properties. In-Ga paste was applied as electrodes. The temperature was measured by a TC-6621 thermocouple calibrator with a type K thermocouple. The $(KNO_3)_{1-x}/(CsNO_3)_x$ composites were measured by nonlinear dielectric spectroscopy in accordance with the technique, described in [11, 12]. To determine the region of polar phase existence, the third-harmonic coefficient $\gamma_{3\omega} = U_{3\omega}/U_{\omega}$ was used.

A Linseis STA PT 600 was used for differential thermal analysis of (DTA) of $(KNO_3)_{1-x}/(CsNO_3)_x$ composites. The temperature was varied at a rate of about 1 K/min during measurements of the DTA signal. The temperature range in the studies covered the phase transitions in KNO_3 and $CsNO_3$. To remove adsorbed water, the samples were heated at 420 K for 30 min before the measurements.

Experimental results and discussion

As follows from the data obtained by DTA and scanning electron microscopy (SEM), mixing of the KNO_3 and $CsNO_3$ components does not produce solid solutions. The polar particles of cesium nitrate in the $(KNO_3)_{1-x}/(CsNO_3)_x$ composite are grouped together and form agglomerates (Fig. 1), while the DTA curves exhibit superposition of phase transitions in KNO_3 and $CsNO_3$ nitrates (Fig. 2).

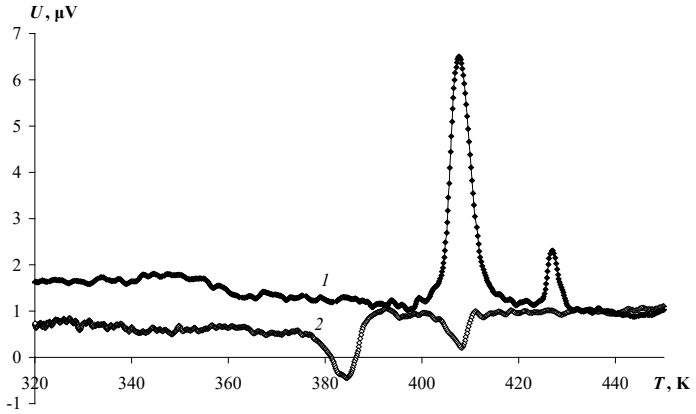

Fig. 2. Signals obtained for the $(KNO_3)_{0.8}/(CsNO_3)_{0.2}$ composite by differential thermal analysis (DTA) upon heating (*1*) and cooling (*2*) of the sample

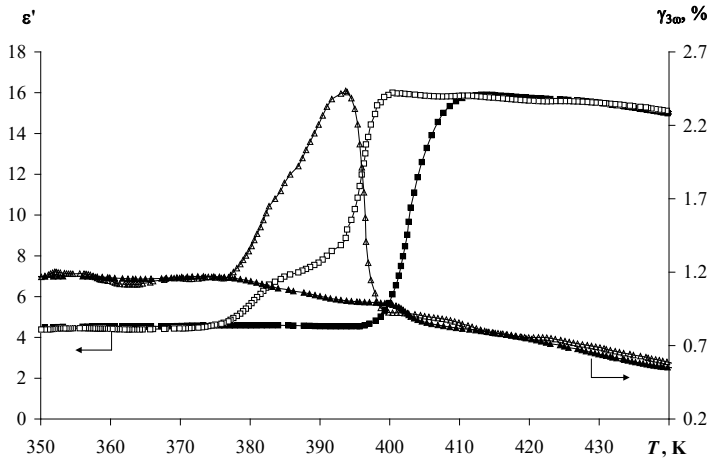

Fig. 3. Temperature dependences of dielectric constant ε′ (at a frequency of 2 kHz) and third-harmonic coefficient $\gamma_{3\omega}$ (at an electric field strength of 25 V/mm) for KNO_3; The data were obtained upon heating (filled symbols) and cooling (empty symbols)

The experimental results, obtained by measuring the temperature dependences of the relative permittivity $\varepsilon'(T)$ and the third-harmonic coefficient $\gamma_{3\omega}(T)$ for polycrystalline potassium nitrate, are shown in Fig. 3. As the sample is cooled from 453 K, two anomalies are observed on the $\varepsilon'(T)$ curve. At $T = 401$ K, KNO_3 transfers from trigonal paraelectric phase I to trigonal ferroelectric phase III, and at T = 377 K, it transfers from phase III to paraelectric orthorhombic phase II.

Analyzing the $\gamma_{3\omega}(T)$ and $\varepsilon'(T)$ dependences (see Fig. 3), we can see that the polar phase in potassium nitrate, emerging upon cooling, lies within the temperature range of 24 K, which corresponds to the data, known from the literature [6]. The third-harmonic coefficient $\gamma_{3\omega}$ for KNO_3 takes a maximum value of about 2.4% at an electric field strength $E = 25$ V/mm and of about 4.7% at $E = 53$ V/mm.

Fig. 4 shows the $\varepsilon'(T)$ and $\gamma_{3\omega}(T)$ dependences for cesium nitrate. As evident from the analysis of these results, the ferroelectric phase is observed in $CsNO_3$ below 427 K, which is confirmed by the $\gamma_{3\omega}(T)$ temperature dependence. However, the maximum value of $\gamma_{3\omega}(T)$ at $E = 25$ V/mm is about 1.2%, which is explained by the low spontaneous polarization of the $CsNO_3$ compound [10].

For $(KNO_3)_{(1-x)}/(CsNO_3)_x$ composite samples with increasing x, a decrease in the effective permittivity ε' is observed due to the emergence of the interlayer polarization. The temperature of phase transitions somewhat decreases. (Fig. 5). The dielectric loss tangent tgδ in the ferroelectric phase with $T = 391$ K at a frequency of 20 kHz equals ~0.11 for KNO_3; ~0.35 for $(KNO_3)_{0.9}/(CsNO_3)_{0.1}$; ~0.60 for $(KNO_3)_{0.7}/(CsNO_3)_{0.3}$; ~0.51 for $(KNO_3)_{0.5}/(CsNO_3)_{0.5}$; ~0.06 for pure $CsNO_3$.

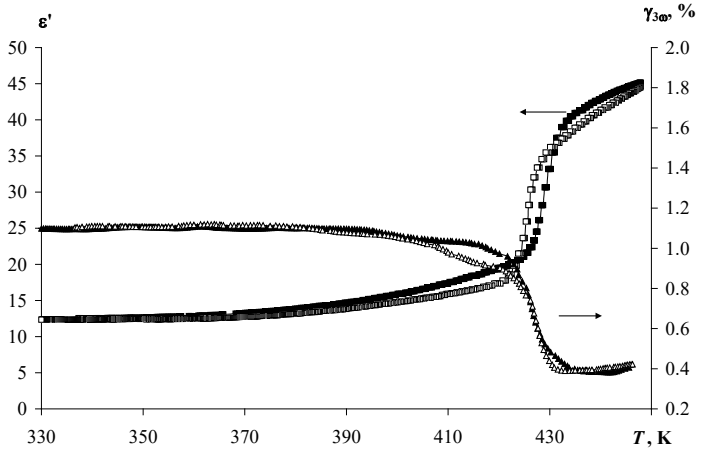

Fig. 4. Temperature dependences of dielectric constant ε' (at a frequency of 2 kHz) and third-harmonic coefficient $\gamma_{3\omega}$ (at an electric field strength of 25 V/mm) for $CsNO_3$
The data were obtained upon heating (filled symbols) and cooling (empty symbols)

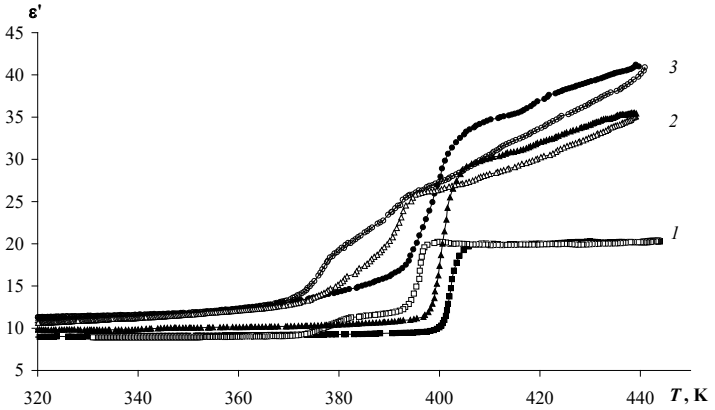

Fig. 5. Temperature dependences of permittivity ε' upon heating (filled symbols) and cooling (empty symbols) of KNO_3 (*1*), $(KNO_3)_{0.9}/(CsNO_3)_{0.1}$ (*2*) and $(KNO_3)_{0.7}/(CsNO_3)_{0.3}$ (*3*) composites at a frequency of 20 kHz

Fig. 6 shows the temperature evolution of $\gamma_{3\omega}$ in $(KNO_3)_{(1-x)}/(CsNO_3)_x$ composite samples with different values of x ($CsNO_3$ content). As follows from the graphs, the third-harmonic coefficient decreases with increasing x from 4.7% for pure KNO_3 to 0.41% for the $(KNO_3)_{0.7}/(CsNO_3)_{0.3}$ composite, while the temperature range of the ferroelectric phase for KNO_3 is narrowed down from 24 to 12 K, respectively. If $x = 0.5$ (Fig. 7), a phase transition is observed at 396 K under heating and at 380 K upon cooling. The ferroelectric phase is no longer detected on the $\gamma_{3\Omega}(t)$ curve in potassium nitrate upon cooling, and the $\gamma_{3\omega}$ maxima have smaller values than in pure KNO_3 or $CsNO_3$ compounds.

The results obtained can be interpreted by referring to [2, 3], where it was shown that adding titanates [2] and niobates [3] with large spontaneous polarization to potassium nitrate leads to expansion in the temperature range of phase III corresponding to the ferroelectric state. The degree of mutual influence of the composite components depends on the values of spontaneous polarization, permittivity, and also on the volume ratio of these components.

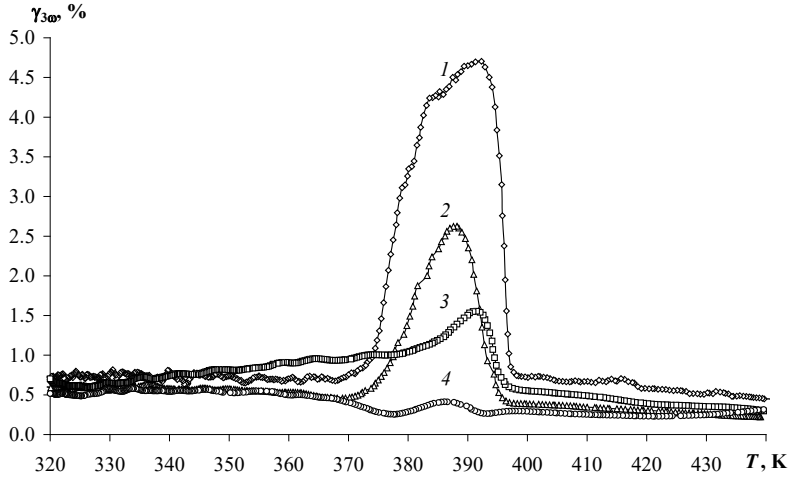

Fig. 6. Temperature dependence of the third-harmonic coefficient $\gamma_{3\omega}$ in $(KNO_3)_{(1-x)}/(CsNO_3)_x$ composite at $x = 0.0$ (*1*); 0.1 (*2*); 0.2 (*3*); 0.3 (*4*) upon cooling; the electric field strength is 25 V/mm

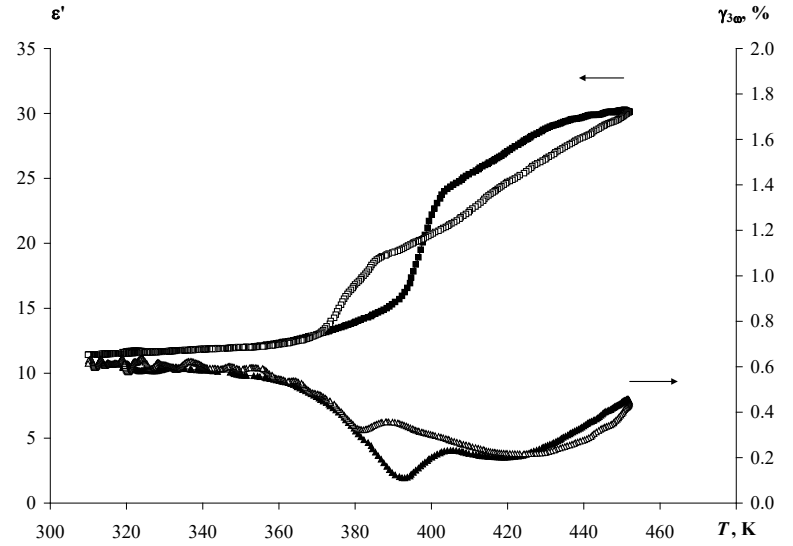

Fig. 7. Temperature dependences of ε′ at a frequency of 20 kHz and $\gamma_{3\omega}$ upon heating (filled symbols) and cooling (empty symbols) in the $(KNO_3)_{0.5}/(CsNO_3)_{0.5}$ composite

Our findings indicate that adding cesium nitrate, which has small spontaneous polarization, to potassium nitrate during the making of the $(KNO_3)_{(1-x)}/(CsNO_3)_x$ composite material results in destabilizing the ferroelectric state of (KNO_3). Similar narrowing of the temperature range where the polar state exists was also observed for solid solutions of $Rb_xK_{1-x}NO_3$ [15]. It was found in this study that spontaneous polarization of the $Rb_xK_{1-x}NO_3$ solid solutions decreased within increasing content of rubidium ions, and the ferroelectric state disappeared upon reaching the fraction $x > 0.5$. The cooperative behavior of particles during the III → I phase transition was reported in [14] for granular and powder potassium nitrates. This narrowed the temperature range where phase III was stable. Individual KNO_3 particles behaved like separate ferroelectric domains, so that a phase transition in each particle occurred independently of the expected Curie temperature. KNO_3 particles in close contact exhibited a trend towards cooperative behavior (as a single large ferroelectric domain), towards making more pronounced phase transitions characteristic of single crystals. Adding silicon carbide powder (SiC), which is not a ferroelectric compound, to KNO_3 powder caused the disappearance of the III → I phase transition in the KNO_3 powder, this is explained by a decrease in the interaction between potassium nitrate particles.

Conclusion

To summarize, if the temperature range of the ferroelectric phase is observed to expand in composites based on potassium nitrate, obtained by adding ferroelectrics with large spontaneous polarization, adding ferroelectrics with a smaller spontaneous polarization than that of KNO_3 tends to destabilize its polar state.

REFERENCES

1. **Scott J. F.,** Ferroelectric memories; Springer Series in Advanced Microelectronics, Springer, Berlin. 3 (26) (2000).

2. **Stukova E. V., Baryshnikov S. V.,** Stabilization of the ferroelectric phase in $(KNO_3)_{1-x}$-$(BaTiO_3)_x$ composites, Inorg. Mater. Appl. Res. 2 (5) (2011) 434–438.

3. **Stukova E. V., Baryshnikov S. V.,** Dielektricheskiye issledovaniya segnetoelektricheskikh kompozitov na osnove $(KNO_3)_{1-x}$-$(BaNbO_3)_x$ [Dielectric research of ferroelectic composites based on $(KNO_3)_{1-x}$-$(BaNbO_3)_x$], Perspektivnyye materialy. (S13) (2011) 801–805 (in Russian).

4. **Shimada S., Aoki T.,** Stabilization of the ferroelectric phase of KNO_3 by doping with Na^+, determined by the acoustic emission method, Chem. Lett. 25 (5) (1996) 393–394.

5. **Baryshnikov S. V., Charnaya E. V, Milinskiy A. Yu., et al.,** Phase transitions in $K_{1-x}Na_xNO_3$ embedded into molecular sieves, J. Phys. Cond. Mat. 21 (32) (2009) 325902.

6. **Chen A., Chernow A.,** Nature of feroelectricity in KNO_3, Phys. Rev. 154 (2) (1967) 493–505.

7. **Deshpande V. V., Karkhanavala M. D., Rao U. R. K.,** Phase transitions in potassium nitrate, J. Therm. Anal. Calorim. 6 (6) (1974) 613–621.

8. **Nimmo J. K., Lucas B. W.,** The crystal structures of γ- and β-KNO_3 and the α ← γ ← β phase transformations, Acta Cryst. B. B32 (7) (1976) 1968–1971.

9. **Lucas B. W.,** The structure (neutron) of phase II caesium nitrate at 298 K, $CsNO_3$, Acta Cryst. C. C39 (12) (1983) 1591–1594.

10. **Takagi Y., Kimura S., Takeuchi Y.,** Structural phase transition of $CsNO_3$ crystal. Spontaneous polarization, Ferroelectrics. 284 (1) (2003) 129–135.

11. **Ikeda S., Kominami H., Koyama K., Wada Y. J.,** Nonlinear dielectric constant and ferroelectric-to-paraelectric phase transition in copolymers of vinylidene fluoride and trifluoroethylene, Appl. Phys. 62 (8) (1987) 3339–3342.

12. **Yudin S. G., Blinov L. M., Petukhova N. N., Palto S. P.,** Ferroelectric phase transition in Langmuir – Blodgett films of copper phthalocyanine, J. Exp. Theor. Phys. Lett. 70 (9) (1999) 633–640.

13. **Burmakin E. I.,** Tverdyye elektrolity s provodimost'yu po kationam shchelochnykh metallov [Solid electrolytes conducting by alkali metal cations], Nauka, Moscow, 1992 (in Russian).

14. **Westphal M. J.,** Cooperative behavior during ferroelectric transitions in KNO_3 powder, J. Appl. Phys. 74 (5) (1993) 3131–3137.

15. **Kawabe U., Yanagi T., Sawada S.,** Dielectric and X-ray studies of KNO_3-series mixed crystals, J. Phys. Soc. Jap. 20 (11) (1965) 2059–2073.

СПИСОК ЛИТЕРАТУРЫ

1. **Scott J. F.** Ferroelectric memories. Springer Series in Advanced Microelectronics. Vol. 3. No. 26. Berlin: Springer, 2000. 248 p.

2. **Стукова Е. В., Барышников С. В.** Стабилизация сегнетоэлектрической фазы в композитах $(KNO_3)_{1-x}$-$(BaTiO_3)_x$ // Перспективные материалы. 2011. № 2. С. 28–33.

3. **Стукова Е. В., Барышников С. В.** Диэлектрические исследования сегнетоэлектрических композитов на основе $(KNO_3)_{1-x}$-$(KNbO_3)_x$// Перспективные материалы. 2011. № 13. С. 801–805.

4. **Shimada S., Aoki T.** Stabilization of the ferroelectric phase of KNO_3 by doping with Na^+, determined by the acoustic emission method // Chemistry Letters. 1996. Vol. 25. No. 5. Pp. 393–394.

5**. Baryshnikov S. V., Charnaya E. V, Milinskiy A. Yu., Stukova E. V., Tien Cheng, Michel D.** Phase transitions in $K_{1-x}Na_xNO_3$ embedded into molecular sieves // Journal of Physics: Condensed Matter. 2009. Vol. 21. No. 32. P. 325902.

6. **Chen A., Chernow A.** Nature of feroelectricity in KNO_3 // Physical Review. 1967. Vol. 154. No. 2. Pp. 493–505.

7. **Deshpande V. V., Karkhanavala M. D., Rao U. R. K.** Phase transitions in potassium nitrate // Journal of Thermal Analysis and Calorimetry. 1974. Vol. 6. No. 6. Pp. 613–621.

8. **Nimmo J. K., Lucas B. W.** The crystal structures of γ- and β-KNO_3 and the α ← γ ← β phase transformations // Acta Crystallografica. B. 1976. Vol. B32. Part 7. Pp. 1968–1971.

9. **Lucas B. W.** The structure (neutron) of phase II caesium nitrate at 298 K, $CsNO_3$ // Acta Crystallografica. C. 1983. Vol. C39. Part 12. Pp. 1591–1594.

10. **Takagi Y., Kimura S., Takeuchi Y.** Structural phase transition of $CsNO_3$ crystal. Spontaneous polarization // Ferroelectrics. 2003. Vol. 284. No. 1. Pp. 129–135.

11. **Ikeda S., Kominami H., Koyama K., Wada Y. J.** Nonlinear dielectric constant and ferroelectric-to-paraelectric phase transition in copolymers of vinylidene fluoride and trifluoroethylene // Applied Physics. 1987. Vol. 62. No 8. Pp. 3339–3342.

12. **Юдин С. Г., Блинов Л. М., Петухова Н. Н., Палто С. П.** Сегнетоэлектрический фазовый переход в пленках Ленгмюра – Блоджетт фталоцианина меди // Письма в Журнал экспериментальной и теоретической физики. 1999. Т. 70. № 9. С. 625–631.

13. **Бурмакин Е. И.** Твердые электролиты с проводимостью по катионам щелочных металлов. М.: Наука, 1992. 264 с.

14. **Westphal M. J.** Cooperative behavior during ferroelectric transitions in KNO_3 powder // Journal of Applied Physics. 1993. Vol. 74. No. 5. Pp. 3131–3137.

15. **Kawabe U., Yanagi T., Sawada S.** Dielectric and X-ray studies of KNO_3-series mixed crystals // Journal of the Physical Society of Japan. 1965. Vol. 20. No. 11. Pp. 2059–2073.

THE AUTHORS

BARYSHNIKOV Sergey V.
Blagoveshchensk State Pedagogical University
104, Lenin St., Blagoveshchensk, 675000, Russia
svbar2003@list.ru
ORCID: 0000-0002-3362-8975

MILINSKIY Alexey Yu.
Blagoveshchensk State Pedagogical University
104, Lenin St., Blagoveshchensk, 675000, Russia
a.milinskiy@mail.ru
ORCID: 0000-0001-7525-4396

STUKOVA Elena V.
Amur State University
21, Ignatievskoe RTe., Blagoveshchensk, 675027, Russia
lenast@bk.ru
ORCID: 0000-0002-7981-7456

ZEEVA Anna A.
Amur State University
21, Ignatievskoe RTe., Blagoveshchensk, 675027, Russia
anutka_2010.1997@mail.ru
ORCID: 0000-0001-7216-3931

СВЕДЕНИЯ ОБ АВТОРАХ

БАРЫШНИКОВ Сергей Васильевич – *доктор физико-математических наук, профессор кафедры физического и математического образования Благовещенского государственного педагогического университета.*
675000, Россия, г. Благовещенск, ул. Ленина, 104
svbar2003@list.ru
ORCID: 0000-0002-3362-8975

МИЛИНСКИЙ Алексей Юрьевич – *доктор физико-математических наук, доцент кафедры физического и математического образования Благовещенского государственного педагогического университета.*
675000, Россия, г. Благовещенск, ул. Ленина, 104
a.milinskiy@mail.ru
ORCID: 0000-0001-7525-4396

СТУКОВА Елена Владимировна – *доктор физико-математических наук, заведующая кафедрой физики Амурского государственного университета.*
675027, Россия, г. Благовещенск, Игнатьевское шоссе, 21
lenast@bk.ru
ORCID: 0000-0002-7981-7456

ЗЕЕВА Анна Анатольевна – *аспирантка кафедры физики Амурского государственного университета.*
675027, Россия, г. Благовещенск, Игнатьевское шоссе, 21
anutka_2010.1997@mail.ru
ORCID: 0000-0001-7216-3931

Received 20.12.2021. Approved after reviewing 24.01.2022. Accepted 24.01.2022.
Статья поступила в редакцию 20.12.2021. Одобрена после рецензирования 24.01.2022. Принята 24.01.2022.

Original article
DOI: https://doi.org/10.18721/JPM.15102

AN ALGEBRAIC TRANSITION MODEL FOR SIMULATION OF TURBULENT FLOWS BASED ON A DETACHED EDDY SIMULATION APPROACH

A. S. Stabnikov ✉, *A. V. Garbaruk*

Peter the Great St. Petersburg Polytechnic University, St. Petersburg, Russia

✉ an.stabnikov@gmail.com

Abstract: A new hybrid RANS/LES method DDES SST KD is proposed, aimed at computations of flows with separation and laminar-turbulent transition in the attached boundary layer. The method is based on a new transition model which uses the SST turbulence model and k-ω KD transition model as a basis. The resulting approach is then tested on a drag crisis problem flows around a circular cylinder and a sphere. The results show that the proposed method is an improvement relative to DDES SST.

Keywords: turbulence, hybrid RANS/LES, DDES, laminar-turbulent transition model, drag crisis

Funding: The reported study was funded by RFBR, project number 19-31-90046.

Citation: Stabnikov A. S., Garbaruk, A. V., An algebraic transition model for simulation of turbulent flows based on a Detached Eddy Simulation approach, St. Petersburg Polytechnical State University Journal. Physics and Mathematics. 15 (1) (2022) 16–29. DOI: https://doi.org/10.18721/JPM.15102

Научная статья
УДК 532.517.4
DOI: https://doi.org/10.18721/JPM.15102

АЛГЕБРАИЧЕСКАЯ МОДЕЛЬ ЛАМИНАРНО-ТУРБУЛЕНТНОГО ПЕРЕХОДА ДЛЯ РАСЧЕТА ТУРБУЛЕНТНЫХ ТЕЧЕНИЙ НА ОСНОВЕ МЕТОДА МОДЕЛИРОВАНИЯ ОТСОЕДИНЕННЫХ ВИХРЕЙ

А. С. Стабников ✉, *А. В. Гарбарук*

Санкт-Петербургский политехнический университет Петра Великого, Санкт-Петербург, Россия

✉ an.stabnikov@gmail.com

Аннотация. Предложен новый глобальный гибридный вихреразрешающий подход DDES SST KD, предназначенный для расчета отрывных течений при наличии перехода в присоединенном пограничном слое. Подход базируется на разработанной авторами модели перехода, основанной на полуэмпирической модели турбулентности SST и алгебраической модели перехода k-ω KD. На примере задачи об обтекании цилиндра и сферы в широком диапазоне чисел Рейнольдса продемонстрировано преимущество предложенного подхода над оригинальным методом DDES SST.

Ключевые слова: турбулентность, вихреразрешающий метод, RANS/LES, DDES, модель ламинарно-турбулентного перехода, кризис сопротивления

Финансирование: Исследование выполнено при финансовой поддержке РФФИ в рамках научного проекта № 90046-31-19.

Для цитирования: Стабников А. С., Гарбарук А. В. Алгебраическая модель ламинарно-турбулентного перехода для расчета турбулентных течений на основе метода моделирования отсоединенных вихрей // Научно-технические ведомости СПбГПУ. Физико-математические науки. 2022. Т. 15. № 1. С. 16–29. DOI: https://doi.org/10.18721/JPM.15102

Introduction

As increasingly efficient computational resources become available, global hybrid eddy-resolving approaches combining the Reynolds-averaged Navier–Stokes equations (RANS) and the Large Eddy Simulation (LES) methods are gaining widespread popularity for simulation of turbulent flows. Some of the most successful are the methods of the DES family (Detached Eddy Simulation), using a standard semi-empirical turbulence model in RANS subdomains of the flow including the attached boundary layers, and a derived subgrid-scale model in the LES-subdomains including the flow recirculation zones. Switching between RANS and LES is performed dynamically during the solution based on the local flow characteristics and the computational mesh. The general consensus [1] is that Delayed Detached Eddy Simulation (DDES) is the method from this family best suited for solving applied problems [2].

Since the Shear Stress Transport (SST) model [3] is considered one of the best, if not the best semi-empirical turbulence model, the methods based on it may prove more accurate than those based on other models. However, the semi-empirical models used to construct hybrid approaches including the SST model typically do not include mechanisms for describing the laminar-turbulent transition in the boundary layer. This can decrease the computational accuracy, since the entire length of the boundary layer is not turbulent in most flows. The turbulent region is generally preceded by a laminar region of some extent, which can significantly affect the overall characteristics of the flow. This effect appears not only at moderate but also at high Reynolds numbers, especially upon separation from a smooth surface. A classic example of the transition effect on separation flow is the drag crisis in bluff bodies, described in detail by Loitsyansky [4]. The crisis is that vortex shedding occurs until the attached boundary layer separates as the Reynolds number increases, which leads to a shift in the separation point and a sharp drop in the drag coefficient.

Thus, the accuracy of hybrid approaches can be improved in some cases by using RANS models capable of accounting for the laminar-turbulent transition (so-called transition models) as a basis.

To date, a large number of transition models have been formulated. Most of them are based on solving differential equations for transport of auxiliary quantities, such as the intermittency γ, the critical Reynolds number Re_θ, the laminar kinetic energy k_l or others. Notably, the existing transition models are still far from perfect, while the SST γ-Re_θ model [5] is regarded as the most accurate, yielding acceptable accuracy for predicting the transition position in diverse types of flows. Four differential equations are solved within this model (two for turbulence characteristics k and ω, as well as two for auxiliary quantities, the intermittence γ and the critical Reynolds number Re_θ). Although the SST γ-Re_θ model offers superior accuracy compared to the standard SST model, as it is capable of describing the transition by different scenarios, it carries higher computational costs necessary to obtain a convergent solution, and in fact sometimes the convergence of the iterative process cannot be achieved at all [6, 7]. These problems are not a specific drawback of the γ-Re_θ model: they are also characteristic of other, less accurate differential transition models. Interestingly, these drawbacks are, so to speak, inherited by hybrid eddy-resolving approaches based on differential transition models as standard RANS models. The same as in the case of RANS, this can lead to computational problems manifesting as the lack of iterative convergence at each time step and increased computational time.

Recently, more and more efforts have been made to develop algebraic transition models, which allow to avoid solving additional differential equations for transition characteristics. These models seem very promising, since they are simpler to use than differential models, provide better convergence and take a relatively small number of additional computations compared to the standard turbulence models on which they are based. Therefore, as algebraic transition models show potential for hybrid approaches, we have concentrated on this subject in the study.

We propose a new hybrid DDES SST KD method combining an algebraic transition model and the transport equations for k and ω as a basis (this approach has been formulated for the first time). The proposed approach comprises the DDES method combined with the shear-layer-adapted (ΔSLA) subgrid length scale, allowing to accelerate the transition to resolved turbulent structures in the separated shear layers, and the SST model complemented with algebraic relations for determining the position of the laminar-turbulent transition from the Kubacki–Dick (KD) k-ω model. Since the ratios of the KD model given in the original study [8] were formulated for Wilcox's k-ω turbulence model [9], they were modified considerably to be used together with the SST model (for details, see the section 'Formulation of the proposed method' below). The

advantages of the approach proposed over the original DDES SST method are illustrated by computational problems on the drag crisis for flow around a sphere and a circular cylinder.

The model and the method were implemented within the framework of the NTS (Numerical Turbulence Simulation), an in-house finite-volume code [10] using the Rogers–Kwak flux-difference splitting [11] to solve incompressible equations of motion, combining a flux-difference splitting scheme for vectors of gas-dynamic flows and the Yanenko–Chorin method for introducing artificial compressibility [12]. The NTS code runs on structured multi-block overset grids (Chimera technique), allowing to adopt schemes with increased approximation order and simulate flows with complex geometry.

The method for approximating non-viscous components of flux vectors in transport equations plays the central role in computations using hybrid RANS-LES approaches. This method determines the dissipative properties of the scheme, which have different requirements in different regions of the flow: the scheme must ensure the stability of the solution in the RANS subdomain, while low-dissipation schemes capable of resolving small-scale turbulence should be introduced in LES subdomains. This study has adopted a hybrid scheme for this purpose [13], functioning as a 3rd-order upwind-biased scheme in the RANS-subdomains and a 4th-order central-difference scheme in the LES-subdomains of the flow.

Formulation of the proposed method

SST KD algebraic transition model. This model is based on modified transport equations for turbulence of the SST model [3]:

$$\begin{cases} \dfrac{\partial k}{\partial t}+\dfrac{\partial\left(u_k k\right)}{\partial x_k}=\gamma P_k+(1-\gamma)P_{sep}-\beta^*\omega k+\dfrac{\partial}{\partial x_k}\left[\left(\nu+\sigma_k\nu_t\right)\dfrac{\partial k}{\partial x_k}\right], \\ \dfrac{\partial \omega}{\partial x_k}+\dfrac{\partial\left(u_k \omega\right)}{\partial x_k}=P_k-\beta\omega^2+\dfrac{\partial}{\partial x_k}\left[\left(\nu+\sigma_\omega\nu_t\right)\dfrac{\partial \omega}{\partial x_k}\right]+2\left(1-F_1\right)\dfrac{\sigma_{\omega 2}}{\omega}\dfrac{\partial k}{\partial x_k}\dfrac{\partial \omega}{\partial x_k}, \end{cases} \tag{1}$$

where k, $m^2 \cdot s^{-2}$, is the turbulent kinetic energy; ω, s^{-1}, is the specific dissipation rate; ν, $m^2 \cdot s^{-1}$, is the kinematic viscosity; ν_t, $m^2 \cdot s^{-1}$, is the turbulent viscosity; u_k, $m \cdot s^{-1}$, are the velocity components; x_k, m, are the coordinate components; t, s, is the time. The explanation for the quantities P_k, P_{sep} will be given below (see Eqs. (8) and (11)).

The function F_1 is found by the expression

$$F_1=\tanh\left(\arg_1^4\right),\ \ \arg_1=\min\left[\max\left(\frac{\sqrt{k}}{\beta^*\omega d_w},\frac{500\nu}{\omega d_w^2}\right),\frac{2k\omega}{d_w^2\left(\nabla k\right)\cdot\left(\nabla\omega\right)}\right], \tag{2}$$

where d_w is the distance to the wall, and the constants of the SST model have the following values:

$$\begin{gathered} \sigma_k=F_1\sigma_{k1}+\left(1-F_1\right)\sigma_{k2},\ \sigma_{k1}=0.85,\ \sigma_{k2}=1.0, \\ \sigma_\omega=F_1\sigma_{\omega 1}+\left(1-F_1\right)\sigma_{\omega 2},\ \sigma_{\omega 1}=0.5,\ \sigma_{\omega 2}=0.856, \\ \beta=F_1\beta_1+\left(1-F_1\right)\beta_2,\ \beta_1=0.075,\ \beta_2=0.0828, \\ \beta^*=0.09,\ \alpha=\beta/\beta^*-\sigma_\omega\kappa^2/\sqrt{\beta^*}. \end{gathered} \tag{3}$$

Eqs. (1) have three differences from the equations of the original SST model; these differences were introduced so that the model could be used together with the KD transition model, where the turbulent viscosity ν_t is divided into two components: small-scale ν_s and large-scale ν_l. Therefore,

$$\nu_t=\nu_s+\nu_l. \tag{4}$$

and $\nu_s = a_s k_s/\max[a_s\omega, F_2 S]$, $\nu_l = a_l k_l/\max[a_l\omega, F_2 S]$;

here

$$k_S = f_{SS}k;\ k_l = k - k_S;\ f_{SS} = \exp\left(-\left(\frac{C_{SS}\nu\Omega}{k}\right)^4\right), \tag{5}$$

$$C_{SS} = C_S\left(1.0 + C_A f_W \psi\right);\ f_W = 1 - \tanh\left(\frac{k}{C_W \nu\omega}\right);$$
$$\psi = \tanh\left(\frac{-\Omega\left(S-\Omega\right)}{C_\psi\left(\beta^*\omega\right)^2}\right), \tag{6}$$

$$F_2 = \tanh\left(\arg_2^2\right),\ \arg_2 = \max\left(2\sqrt{k}\Big/\left(0.09\omega d_w\right), 500\nu\Big/\left(d_w^2\omega\right)\right). \tag{7}$$

(S, Ω are the magnitudes of the strain and swirl velocity tensors, respectively).

The differences mentioned above consist in the following.

1. Generation of turbulent kinetic energy P_k is calculated using small-scale viscosity and kinetic energy:

$$P_k = \min\left(-\overline{u_i'u_j'}\,\partial U_i/\partial x_j, 10\cdot\beta^* k\omega\right), \tag{8}$$

$$\overline{u_i'u_j'} = \frac{2}{3}k_S\delta_{ij} - 2\nu_S S_{ij}. \tag{9}$$

2. The generative term in Eq. (1) for k is multiplied by the intermittency factor γ:

$$P_k \to \gamma P_k. \tag{10}$$

3. The transition to turbulence in the separated laminar boundary layer is described by introducing an additional term $(1-\gamma)P_{sep}$ to Eq. (1) for k, where the quantity P_{sep}, borrowed in a simplified form from the differential model [14], is calculated by the following formulas:

$$P_{sep} = C_{sep}F_{sep}\nu S^2; \tag{11}$$

$$F_{sep} = \min\left(\max\left(\frac{R_V}{2.2A_V} - 1.0, 0.0\right)1.0\right);\ R_V = \frac{d_w^2 S}{\nu}. \tag{12}$$

The intermittency factor included in the model is determined by the following expression:

$$\gamma = \min\left(\max\left(\frac{k}{\nu A_\gamma \Omega} - 1.0, 0.0\right), 1.0\right). \tag{13}$$

The main difference between the algebraic relations used in the proposed method and the original KD model [8] consists in changing the criterion in Eqs. (5) for f_{SS} and (13) for intermittency γ. Furthermore, the model constants were optimized for problems on the transition boundary layer with a T3C-series pressure gradient [15]:

$$A_\gamma = 1.3,\ C_S = 2.0,\ C_A = 1.0,\ C_\psi = 10.0,\ C_W = 5.0,$$
$$C_{sep} = 2.0,\ A_V = 550.0,\ a_1 = 0.31\ \ a_2 = 0.45. \tag{14}$$

The SST KD model constructed was tested in RANS simulations for 2D problems, where the laminar-turbulent transition plays a major role, confirming that the model proposed yields significantly better accuracy than the original KD k-ω model [8].

DDES SST KD method. The proposed algebraic model of the SST KD transition was combined with the DDES method [2] to make up a basis for the DDES SST KD method, intended for computing separated flows in the presence of a laminar-turbulent transition in the attached boundary layer. The proposed method uses the DDES version introducing a shear-layer-adapted subgrid length scale (DDES ΔSLA [16]). This modification of the subgrid scale is aimed at accelerating the transition to well-developed three-dimensional turbulence in the initial regions of the shear layers and allows significantly increasing the simulation accuracy for separated flows without increasing the computational mesh and, as a result, the computational costs.

The transition model was additionally modified to function within the eddy-resolving method, restricting the transition model outside the boundary layer:

$$\gamma = 1.0 \text{ for } F_1 < 0.9, \tag{15}$$

where F_1 is the function of the SST model (see Eq. (2)).

Application of the developed approach to predicting the drag crisis

Drag resistance for flow around a cylinder. We consider unsteady cross-flow of incompressible fluid around a circular cylinder in the range of Reynolds numbers from $5.0 \cdot 10^4$ to $1.2 \cdot 10^6$; the number is constructed from the diameter D_c of the cylinder and the freestream velocity U_0 ($\mathrm{Re} = D_c U_0/\nu$).

This interval completely covers the drag crisis, which is observed within the range $1.3 \cdot 10^5 < \mathrm{Re} < 10 \cdot 5.0^5$ [17].

Table 1

Boundary conditions for turbulence characteristics in the problem on flow around a cylinder

Re, 10^4	ν_t/ν	Tu, %
5.0	0.30	0.40
8.0	0.30	0.55
10	0.36	0.60
13	0.45	0.64
17	0.56	0.73
20	0.65	0.77
25	0.79	0.95
30	0.94	1.00
40	1.25	1.02
50	1.55	1.15
70	2.16	1.35
90	2.75	1.55
120	3.65	1.70

Notations: Re is the Reynolds number, ν_t is the turbulent viscosity, ν is the kinematic viscosity, Tu is the turbulent intensity.

The computational domain is a cylinder with a radius of $25D_c$, where D_c is the diameter of the streamlined cylinder, centered at $(x, y) = (0.0, 0.0)$. The length of the computational domain in the transverse direction z is $L_z = 5\ D_c$, which is greater than the quantity πD_c commonly used in such computations (see, for example, [18, 19]), and should not adversely affect the result.

Because the SST model assumes that the turbulent kinetic energy decreases (dissipates) in homogeneous turbulent flow, generally, so that the turbulent characteristics in the vicinity of the streamlined body correspond to certain required values, the boundary conditions for the equations of the turbulence model have to be adjusted. Such values can be obtained at the inlet to the computational domain from the analytical solution to the equations of the SST model in homogeneous flow by the following formulas:

$$k = c_2 \left(\beta x + c_1\right)^{\frac{\beta^*}{\beta}}, \tag{16}$$

$$\omega = \frac{1}{\beta x + c_1}, \tag{17}$$

where x is the coordinate along the flow in free stream; c_1, c_2 are the integration constants obtained from boundary values; the values of constants β and β^* are given above.

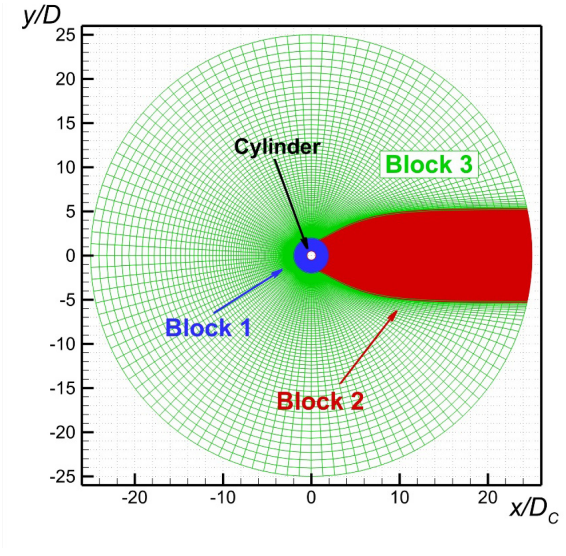

Fig. 1. Three blocks of the computational meshes (shown in different colors) in the problem of flow around a circular cylinder (section $z = 0$)

The equations do not have a finite analytical solution for sufficiently large longitudinal dimensions of the computational domain. In such cases, the turbulence characteristics are 'frozen' to a certain point upstream of the body, then 'released' and dissipated to the required values.

The turbulent intensity Tu = 0.45% (Tu = $100[(2/3)P_k]1/2/U_0$) is generated in this problem in the vicinity of the cylinder's middle section, the turbulence characteristics were frozen to the section $x = 2–D_c$ and their inlet values were calculated by Eqs. (16), (17) (Table 1).

Constant pressure was given at the outlet boundary, and no-slip and impermeability conditions $u_w = v_w = w_w = 0$ were imposed on the cylinder surface. Standard conditions for the SST model were imposed for turbulent characteristics on the wall:

$$k_w = 0,\ \omega_w = 10\frac{6\nu}{\beta_1\Delta_1^{\,2}},$$

where Δ_1 is the size of the first near-wall spacing of the mesh.

Finally, periodic boundary conditions were imposed in the transverse direction.

The computational meshes consisted of three blocks (Fig. 1). The first block contained a refined mesh for computing high gradients of the quantities near the cylinder surface, the second one was refined for computing the wake behind the cylinder. The third block contained unperturbed homogeneous flow without unsteady fluctuations and the coarsest mesh.

A total of three meshes were constructed for computations with different ranges of Reynolds numbers, characterized by the magnitude of the first near-wall spacing: I, II, and III (Table 2).

The time step Δt was equal to $5\cdot10^{-3}\cdot D_c/U_0$, maintaining the value of the Courant–Friedrichs–Lewy (CFL) criterion below unity in the separation zone in the cylinder wake. The solution was averaged after the flow was stabilized over time intervals of about $50\cdot D_c/U_0$.

Fig. 2 compares the simulated dependences obtained for the drag coefficient $C_D = F_x/[(5/2)\rho U_0^2]$ (F_x is the drag force acting on the cylinder, ρ is the density) versus the Reynolds number with the experimental data [20–26].

Table 2

Parameters of computational meshes in the problem on flow around a cylinder

#	Re range, 10^4	Block size			Total number of cells
		Block 1	Block 2	Block 3	
I	5.0–20	512×161×60	200×184×256	131×101×52	56,270,732
II	25–60	512×191×560	200×184×256	131×101×52	64,872,332
III	70–120	512×221×560	200×184×256	131×101×52	73,473,932

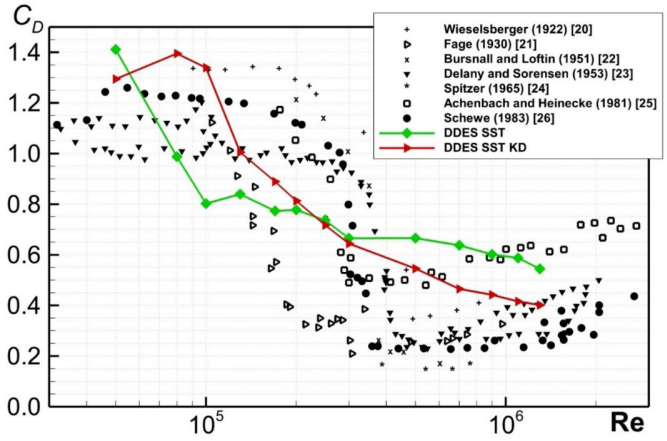

Fig. 2. Simulated curves (solid lines) of the drag coefficient in a circular cylinder as a function of the Reynolds number compared with the experimental data (symbols) [20–26]

This flow clearly confirms the advantage of the proposed hybrid method over the original DDES SST approach. Evidently, the computed drag coefficients obtained by the transition model turn out to be closer to the experimental values. However, complete agreement with the experimental data could not be achieved; in particular, the decrease in the computed drag coefficient in the vicinity of the critical Reynolds number is much slower than in the experimental dependences. The reasons for this behavior require further study and are beyond the scope of our paper.

Drag crisis for flow around a sphere. We consider unsteady cross-flow of incompressible fluid around a sphere in the range of Reynolds numbers from $5.0 \cdot 10^4$ to $4.0 \cdot 10^5$; the number is constructed from the diameter D_s of the sphere and the freestream velocity U_0 ($\mathrm{Re} = D_s U_0/\nu$)

The computational domain is a sphere with a radius of $20D_s$. The boundary conditions were imposed similarly to the solution of the problem on the flow around a cylinder. The only difference was in the inlet values chosen for the turbulence characteristics: they were tailored to provide a turbulence intensity of 0.45% in the vicinity of the sphere's middle section (Table 3).

Table 3

Boundary conditions for turbulence characteristics in the problem on flow around a sphere

Re, 10^4	ν_t/ν	Tu, %
5.0	0.35	1.2
10	0.70	1.2
20	1.40	1.4
40	2.8	1.6
60	4.2	1.7
100	7.0	1.9

The notations are identical to those given in Table 1

The computational mesh consisted of six blocks (Fig. 3). Blocks from 1 to 3 were adjacent to the surface of the sphere and are characterized by small mesh spacings (514 cells per sphere circumference), while the mesh spacings were about 3 times larger in the outer blocks (4 to 6). Blocks 1 and 4 have a cylindrical shape and are characterized by axial symmetry relative to the axis x (Fig. 3,*b*). The remaining mesh blocks have the shape of a truncated pyramid, allowing to avoid unreasonable clustering in the vicinity of the symmetry axis of the 1st and 4th blocks (Fig. 4).

The mesh spacings were refined to the surface of the sphere and in the vicinity of the wake. The same as in the solution to the problem on flow around a cylinder, we constructed a series of meshes for computations at different Reynolds numbers, varying by the first near-wall spacing. The total number of cells in the mesh was about 16 million. A series of preliminary computations carried out by the DDES SST and DDES SST KD methods at $\mathrm{Re} = 1.0 \cdot 10^5$ indicate that refining the mesh by 1.5 times in each direction (this mesh contains is about 46 million cells) does not change the time-averaged solution.

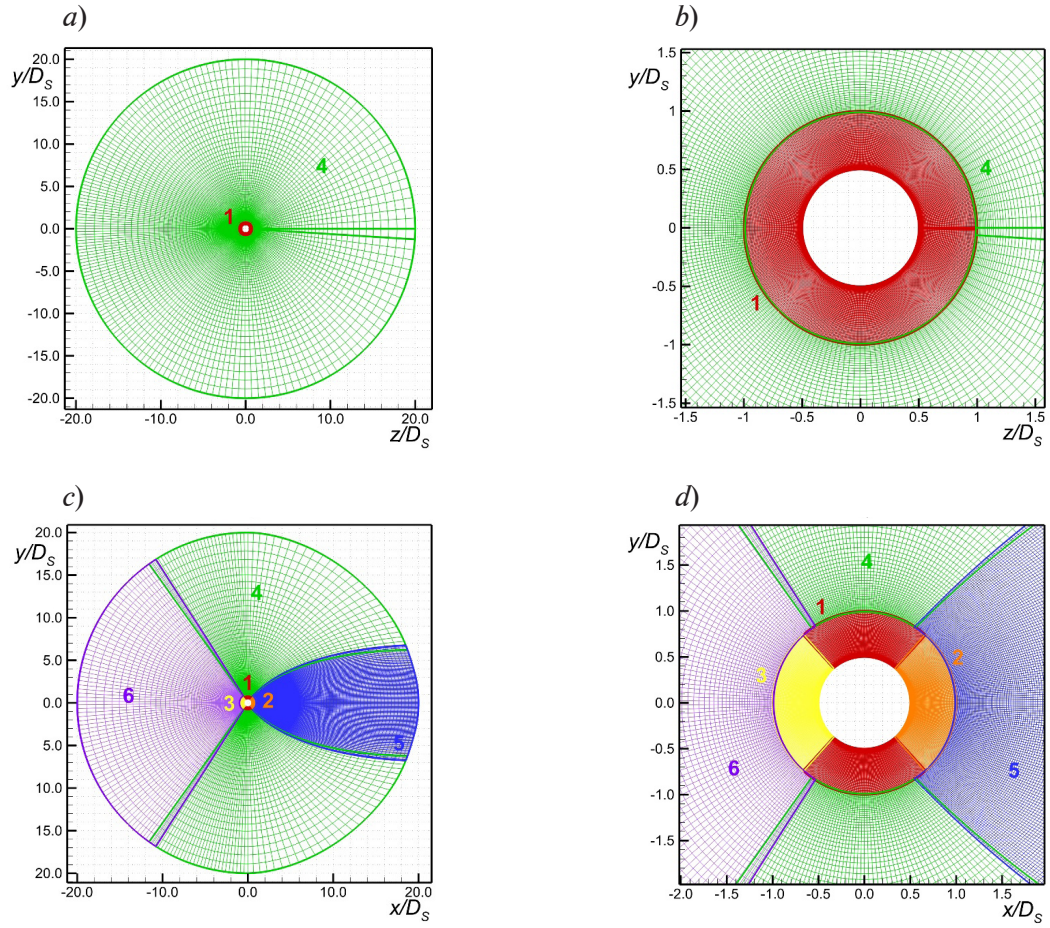

Fig. 3. Blocks of computational meshes (numbered and marked by different colors) for the problem on flow around a sphere. The figure shows sections $z = 0$ (*a*, *b*) and $x = 0$ (*c*, *d*); *b*, *d* are enlarged images of the middle sections in graphs *a* and *c*, respectively

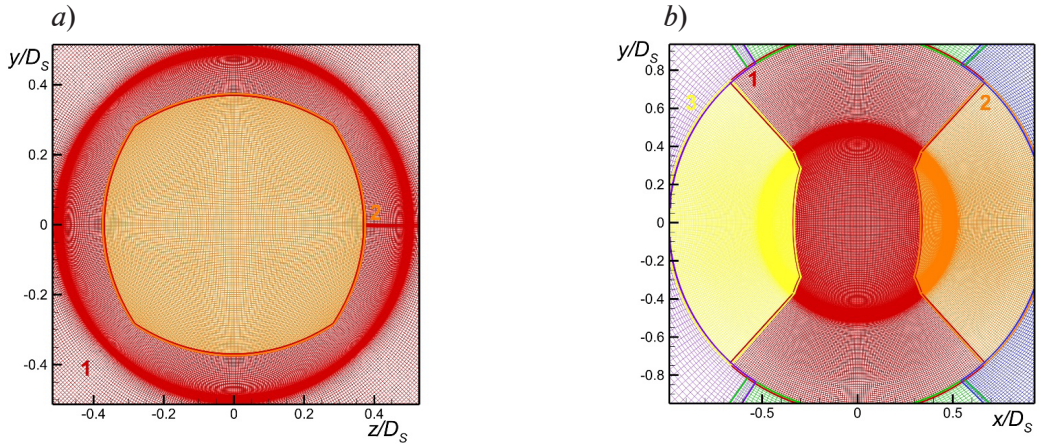

Fig. 4. Computational meshes in sections $x = 0$ (*a*) and $z = 0$ (*b*) for the problem on flow around a sphere. Surface meshes are projected on the corresponding sections

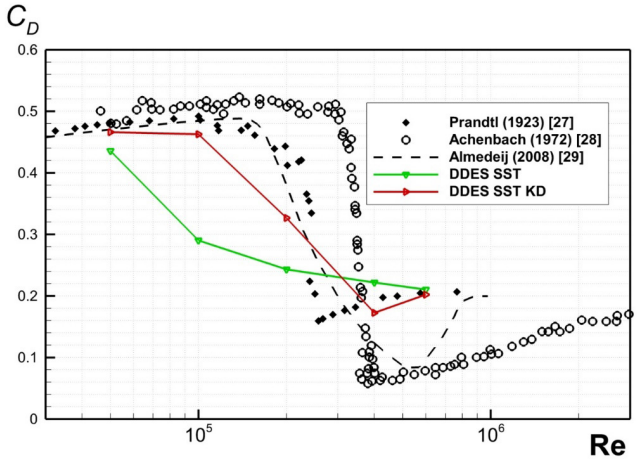

Fig. 5. Simulated curves (solid lines) of the sphere's drag coefficient as a function of the Reynolds number compared with the experimental data (symbols) [27–28] and empirical correlations [29]

The time step was taken equal to $\Delta t = 10{\cdot}5^{-3} D_s/U_0$, providing, the same as in the problem of the cylinder, the value of the Courant number CFL < 1 in the separation zone behind the sphere. Additional computations confirmed that refining the time step does not change the time-averaged solution. The solution was averaged after the flow was stabilized over time intervals of about $50{\cdot}D_s/U_0$.

Fig. 5 compares the simulated dependences obtained for the drag coefficient $C_D = F_x/[(1/2)\rho U_0^2 \cdot (4/1)\pi D_s^2]$ versus the Reynolds number with the experimental data (F_x is the drag force acting on the sphere).

The computational results were compared with the experimental data presented in [27–28] and empirical correlations in [29].

First of all, we should note that the proposed method considerably improves the computational accuracy for all the values of the Reynolds number considered. The original DDES SST method predicts virtually no decrease in the drag coefficient associated with the drag crisis as the Reynolds number increases in the range $1{\cdot}10^5 < \mathrm{Re} < 10{\cdot}4^5$, while the proposed method offers a qualitative description. At the same time, the computational results obtained by the proposed method differed somewhat from the experimental data, which is primarily manifested (the same as in the problem of on flow around a cylinder), in a slower decrease in the computed drag coefficient in the vicinity of the critical value of the Reynolds number.

Conclusion

We have proposed a new global hybrid eddy-resolving approach intended for computing separated flows with a transition in the attached boundary layer. The approach is based on the transition model we have formulated, based on the semi-empirical SST turbulence model and the k-ω KD algebraic transition model.

The advantages of the proposed approach over the original DDES SST method were illustrated by test problems on flow around a cylinder and a sphere in a wide range of Reynolds numbers.

REFERENCES

1. **Garbaruk A. V.**, Sovremennyye podkhody k modelirovaniyu turbulentnosti [Modern approaches to the turbulence simulation], Polytechnic University Publishing, St. Petersburg, 2016.

2. **Spalart P. R., Deck S., Shur M. L., et al.,** A new version of Detached-Eddy Simulation, resistant to ambiguous grid densities, Theoret. Comput. Fluid Dynamics. 20 (3) (2006) 181–195.

3. **Menter F. R., Kuntz M., Langtry R.,** Ten years of industrial experience with the SST turbulence model, Heat & Mass Transfer. 2003. Vol. 4 (January) (2003).

4. **Loytsyanskiy L.G.,** Mekhanika zhidkosti i gaza [Fluids and gas mechanics], Gostechizdat, Moscow-Leningrad, 1950 (in Russian).

5. **Langtry R. B., Menter F. R.,** Correlation-based transition modeling for unstructured parallelized computational fluid dynamics codes, AIAA Journal. 2009. Vol. 47 (12) (2009) 2894–2906.

6. **Wauters J., Degroote J.,** On the study of transitional low-Reynolds number flows over airfoils operating at high angles of attack and their prediction using transitional turbulence models, Prog. Aerosp. Sci. 103 (November) (2018) 52–68.

7. **Lopes R., Eça L., Vaz G.,** On the numerical behavior of RANS-based transition models, J. Fluids Eng. 142 (5) (2020) 051503.

8. **Kubacki S., Dick E.,** An algebraic model for bypass transition in turbomachinery boundary layer flows, Int. J. Heat Fluid Flow. 58 (April) (2016) 68–83.

9. **Wilcox D. C.,** Formulation of the k-ω turbulence model revisited, AIAA Journal. 46 (11) (2008) 2823–2838.

10. **Shur M., Strelets M., Travin A.,** High-order implicit multi-block Navier –Stokes code: Ten-years experience of application to RANS/DES/LES/DNS of turbulent flows (invited lecture), In: Proceeding of the 7th Symposium on Overset Composite Grids and Solution Technology, Oct. 5–7, Huntington Beach, USA, 2004.

11. **Rogers S., Kwak D.,** An upwind differencing scheme for the time-accurate incompressible Navier – Stokes equations, In: Proceeding of the 6th Applied Aerodynamics Conference, American Institute of Aeronautics and Astronautics, Williamsburg, USA.1988, November, Rep. No. NASA-TM-101051.

12. **Chorin A. J.,** A numerical method for solving incompressible viscous flow problems, J. Comput. Phys. 2 (1) (1967) 12–26.

13. **Travin A., Shur M., Strelets M., Spalart P. R.,** Physical and numerical upgrades in the Detached-Eddy Simulation of complex turbulent flows, In book: Advances in LES of Complex Flows, Vol. 65. Ed. by Friedrich R., Rodi W., Springer Netherlands, Dordrecht (2002) 239–254.

14. **Menter F. R., Smirnov P. E., Liu T., Avancha R.,** A one-equation local correlation-based transition model, Flow, Turb. Combust. 95 (4) (2015) 583–619.

15. **Savill A. M.,** Evaluating turbulence model predictions of transition: An ERCOFTAC special interest group project, Appl. Sci. Res. 51 (1–2) (1993) 555–562.

16. **Probst A., Schwamborn D., Garbaruk A., et al.,** Evaluation of grey area mitigation tools within zonal and non-zonal RANS-LES approaches in flows with pressure induced separation, Int. J. Heat Fluid Flow. 68 (December) (2017) 237–247.

17. **Smith A. M. O., Gamberoni N.,** Transition, pressure gradient and stability theory, Techn. Rep. ES-26388, Douglas Aircraft Company, El Segundo Division, Santa Monica, California, USA, 1956.

18. **Pereira F. S., Vaz G., Eca L.,** An assessment of scale-resolving simulation models for the flow around a circular cylinder, In: Proc. Eighth Int. Symp. Turbulence, Heat and Mass Transfer (THMT-15), Sept. 15–18, Begellhouse, Sarajevo, Bosnia and Herzegovina (2015) 295–298.

19. **Pereira F. S., Vaz G., Eça L.,** Flow past a circular cylinder: A comparison between RANS and hybrid turbulence models for a low Reynolds number, In: Proc. ASME 2015: 34th Int. Conf. Ocean, Offshore & Arctic Eng., May 31–June 5, 2015, St. John's, Newfoundland, Canada. Vol. 2: CFD and VIV, ASME, 2015. P. No. OMAE2015-41235, V002T08A006.

20. **Wieselsberger C.,** New data on the laws of fluid resistance, Tech. Rep. Number NACA-TN-84, NACA, 1922, March 1, ID 19930080855.pdf.

21. **Fage A.,** The drag of circular cylinders and spheres at high values of Reynolds number (Tech. Rep.), Reports & Memoranda, No. 1370, Aeronautical Research Commettee, London, May, 1930.

22. **Bursnall W., Loftin L. K. Jr.,** Experimental investigation of the pressure distribution about a yawed circular cylinder in the critical Reynolds number range, Tech. Rep. NACA-TN-2463, NACA, Washington, September, 1951.

23. **Delany N., Sorensen N.** Low-speed drag of cylinders of various shapes // Tech. Rep. NACA TN-3038, NACA, Washington, 1953.

24. **Spitzer R.,** Measurements of unsteady pressures and wake fluctuations for flow over a cylinder at supercritical Reynolds number, Ph.D. thesis, California Institute of Technology, Pasadena, USA,1965.

25. **Achenbach E., Heinecke E.,** On vortex shedding from smooth and rough cylinders in the range of Reynolds numbers 6×10^3 to 5×10^6, J. Fluid Mech. 109 (August) (1981) 239–251.

26. **Schewe G.,** On the force fluctuations acting on a circular cylinder in crossflow from subcritical up to transcritical Reynolds numbers, J. Fluid Mech. 133 (1983) 265–285.

27. **Prandtl L.,** Ergebnisse der Aerodynamischen Versuchsanstalt zu Götingen, II. Lieferung. Der induzierte Widerstand von Mehrdeckern (1923) 9–16.

28. **Achenbach E.,** Experiments on the flow past spheres at very high Reynolds numbers, J. Fluid Mech. 54 (3) (1972) 565–575.

29. **Almedeij J.,** Drag coefficient of flow around a sphere: Matching asymptotically the wide trend, Powder Technol. 186 (3) (2008) 218–223.

СПИСОК ЛИТЕРАТУРЫ

1. **Гарбарук А. В.** Современные подходы к моделированию турбулентности. СПб.: Изд-во Политехнического ун-та, 2016. 233 с.

2. **Spalart P. R., Deck S., Shur M. L., Squires K., Strelets M., Travin A.** A new version of Detached-Eddy Simulation, resistant to ambiguous grid densities // Theoretical Computational Fluid Dynamics. 2006. Vol. 20. No. 3. Pp. 181–195.

3. **Menter F. R., Kuntz M., Langtry R.** Ten years of industrial experience with the SST turbulence model // Heat and Mass Transfer. 2003. Vol. 4. January.

4. **Лойцянский Л. Г.** Механика жидкости и газа. Москва-Ленинград: Гостехиздат, 1950. 676 с.

5. **Langtry R. B., Menter F. R.** Correlation-based transition modeling for unstructured parallelized computational fluid dynamics codes // AIAA Journal (American Institute of Aeronautics and Astronautics). 2009. Vol. 47. No. 12. Pp. 2894–2906.

6. **Wauters J., Degroote J.** On the study of transitional low-Reynolds number flows over airfoils operating at high angles of attack and their prediction using transitional turbulence models // Progress in Aerospace Sciences. 2018. Vol. 103. November. Pp. 52–68.

7. **Lopes R., Eça L., Vaz G.** On the numerical behavior of RANS-based transition models // Journal of Fluids Engineering. 2020. Vol. 142. No. 5. P. 051503.

8. **Kubacki S., Dick E.** An algebraic model for bypass transition in turbomachinery boundary layer flows // International Journal of Heat and Fluid Flow. 2016. Vol. 58. April. Pp. 68–83.

9. **Wilcox D. C.** Formulation of the k-ω turbulence model revisited // AIAA Journal. (American Institute of Aeronautics and Astronautics). 2008. Vol. 46. No. 11. Pp. 2823–2838.

10. **Shur M., Strelets M., Travin A.** High-order implicit multi-block Navier–Stokes code: Ten-years experience of application to RANS/DES/LES/DNS of turbulent flows (invited lecture) // Proceeding of the 7th Symposium on Overset Composite Grids and Solution Technology. October 5–7, Huntington Beach, USA. 2004.

11. **Rogers S., Kwak D.** An upwind differencing scheme for the time-accurate incompressible Navier – Stokes equations // Proceeding of the 6th Applied Aerodynamics Conference. Williamsburg, USA.: American Institute of Aeronautics and Astronautics, 1988, November. Report No. NASA-TM-101051.

12. **Chorin A. J.** A numerical method for solving incompressible viscous flow problems // Journal of Computational Physics. 1967. Vol. 2. No. 1. Pp. 12–26.

13. **Travin A., Shur M., Strelets M., Spalart P. R.** Physical and numerical upgrades in the Detached-Eddy Simulation of complex turbulent flows // Advances in LES of Complex Flows. Vol. 65. Edited by Friedrich R., Rodi W. Dordrecht: Springer Netherlands, 2002. Pp. 239–254.

14. **Menter F. R., Smirnov P. E., Liu T., Avancha R.** A one-equation local correlation-based transition model // Flow, Turbulence and Combustion. 2015. Vol. 95. No. 4. Pp. 583–619.

15. **Savill A. M.** Evaluating turbulence model predictions of transition: An ERCOFTAC special interest group project // Applied Scientific Research. 1993. Vol. 51. No. 1–2. Pp. 555–562.

16. **Probst A., Schwamborn D., Garbaruk A., Guseva E., Shur M., Strelets M., Travin A.** Evaluation of grey area mitigation tools within zonal and non-zonal RANS-LES approaches in flows with pressure induced separation // International Journal of Heat and Fluid Flow. 2017. Vol. 68. December. Pp. 237–247.

17. **Smith A. M. O., Gamberoni N.** Transition, Pressure Gradient and Stability Theory. Technical Report ES-26388. Santa Monica, California, USA: Douglas Aircraft Company, El Segundo Division, 1956. 59 p.

18. **Pereira F. S., Vaz G., Eca L.** An assessment of scale-resolving simulation models for the flow around a circular cylinder // Proceeding of the Eighth International Symposium on Turbulence Heat and Mass Transfer (THMT-15), September 15–18. Sarajevo, Bosnia and Herzegovina: Begellhouse, 2015. Pp. 295–298.

19. **Pereira F. S., Vaz G., Eça L.** Flow past a circular cylinder: A comparison between RANS and hybrid turbulence models for a low Reynolds number // Proceeding of the ASME 2015: 34th International Conference on Ocean, Offshore and Arctic Engineering, May 31–June 5, 2015, St. John's, Newfoundland, Canada. Vol. 2: CFD and VIV. American Society of Mechanical Engineers, 2015. Paper No. OMAE2015-41235, V002T08A006 (11 p.).

20. **Wieselsberger C.** New data on the laws of fluid resistance. Tech. Rep. Number NACA-TN-84. Work of the US Gov. Public Use Permitted, 1922, March 1. ID 19930080855.pdf.

21. **Fage A.** The drag of circular cylinders and spheres at high values of Reynolds number // Tech. Rep., Reports & Memoranda, No. 1370. London: Aeronautical Research Commettee, May, 1930. 12 p.

22. **Bursnall W., Loftin L. K. Jr.** Experimental investigation of the pressure distribution about a yawed circular cylinder in the critical Reynolds number range // Tech. Rep. NACA-TN-2463. Washington: National Advisory Committee for Aeronautics (NACA), September, 1951. 34 p.

23. **Delany N., Sorensen N.** Low-speed drag of cylinders of various shapes // Tech. Rep. NACA TN-3038, Washington: National Advisory Committee for Aeronautics (NACA), 1953. 36 p.

24. **Spitzer R.** Measurements of unsteady pressures and wake fluctuations for flow over a cylinder at supercritical Reynolds number. Ph.D. thesis, Pasadena (USA): California Institute of Technology, 1965. 93 p.

25. **Achenbach E., Heinecke E.** On vortex shedding from smooth and rough cylinders in the range of Reynolds numbers 6×10^3 to 5×10^6 // Journal of Fluid Mechanics. 1981. Vol. 109. August. Pp. 239–251.

26. **Schewe G.** On the force fluctuations acting on a circular cylinder in crossflow from subcritical up to transcritical Reynolds numbers // Journal of Fluid Mechanics. 1983. Vol. 133. Pp. 265–285.

27. **Prandtl L.** Ergebnisse der Aerodynamischen Versuchsanstalt zu Götingen. II. Lieferung. Der induzierte Widerstand von Mehrdeckern, 1923. S. 9–16.

28. **Achenbach E.** Experiments on the flow past spheres at very high Reynolds numbers // Journal of Fluid Mechanics. 1972. Vol. 54. No. 3. Pp. 565–575.

29. **Almedeij J.** Drag coefficient of flow around a sphere: Matching asymptotically the wide trend // Powder Technology. 2008. Vol. 186. No. 3. Pp. 218–223.

THE AUTHORS

STABNIKOV Andrey S.
Peter the Great St. Petersburg Polytechnic University
29 Politechnicheskaya St., St. Petersburg, 195251, Russia
an.stabnikov@gmail.com
ORCID: 0000-0001-7011-6197

GARBARUK Andrey V.
Peter the Great St. Petersburg Polytechnic University
29 Politechnicheskaya St., St. Petersburg, 195251, Russia
agarbaruk@cfd.spbstu.ru
ORCID: 0000-0002-2775-9864

СВЕДЕНИЯ ОБ АВТОРАХ

СТАБНИКОВ Андрей Сергеевич – *аспирант высшей школы математики и вычислительной физики Санкт-Петербургского политехнического университета Петра Великого, Санкт-Петербург, Россия.*

195251, Россия, г. Санкт-Петербург, Политехническая ул., 29
an.stabnikov@gmail.com
ORCID: 0000-0001-7011-6197

ГАРБАРУК Андрей Викторович – *доктор физико-математических наук, доцент высшей школы математики и вычислительной физики Санкт-Петербургского политехнического университета Петра Великого, Санкт-Петербург, Россия.*

195251, Россия, г. Санкт-Петербург, Политехническая ул., 29
agarbaruk@mail.ru
ORCID: 0000-0002-2775-9864

Received 29.09.2021. Approved after reviewing 29.12.2021. Accepted 10.11.2022.
Статья поступила в редакцию 29.09.2021. Одобрена после рецензирования 29.12.2021. Принята 10.11.2022.

ATOM PHYSICS AND PHYSICS OF CLUSTERS AND NANOSTRUCTURES

Original article
DOI: https://doi.org/10.18721/JPM.15103

CRYSTALLIZATION OF POTASSIUM TITANOSILICATE GLASS UNDER THERMAL POLING USING A PROFILED ANODE

I. V. Reshetov [1,4] ✉, *A. V. Redkov* [1,2], *V. G. Melehin* [3], *V. V. Zhurikhina* [1,4], *A. A. Lipovskii* [1,4]

[1] Alferov University, St. Petersburg, Russia;

[2] Institute of Problems of Mechanical Engineering of the Russian Academy of Sciences, St. Petersburg, Russia;

[3] Ioffe Institute of the Russian Academy of Sciences, St. Petersburg, Russia;

[4] Peter the Great St. Petersburg Polytechnic University, St. Petersburg, Russia

✉ reshetov_iv@spbstu.ru

Abstract: This paper is devoted to in-depth study of the crystallization process in the K_2O-TiO_2-SiO_2 glass under thermal poling using a profiled anode and heating temperature below the glass transition temperature. The crystallization was investigated by Raman scattering and mechanical profilometry at the specified conditions. It was found that the glass remained transparent without crystallization signs on the electrode-glass contact surface (profile peaks at the electrode) whereas the glass surface became frosted over other areas where there was an air gap between the electrode and glass (it was shown to be caused by the formation of a nanocrystalline anatase layer). A transition zone a few tens of micrometers wide and a few micrometers high was formed between frosted and transparent glass areas, i. e. at the edges of the electrode-glass contact surface. The mechanism of formation of the crystalline phase and relief was discussed.

Keywords: glass, thermal poling, profiled anode, crystallization, Raman scattering

Funding: the work was done within the framework of a State assignment "Studies in micro- and nanophotonics structures formed in the amorphous dielectrics under the action of strong fields" (subject code FSRM -2020-001).

Citation: Reshetov I. V., Redkov A. V., Melehin V. G., Zhurikhina V. V., Lipovskii A. A., Crystallization of potassium titanosilicate glass under thermal poling using a profiled anode, St. Petersburg Polytechnical State University Journal. Physics and Mathematics. 15 (1) (2022) 30–40. DOI: https://doi.org/10.18721/JPM.15103

Научная статья
УДК 538.9
DOI: https://doi.org/10.18721/JPM.15103

КРИСТАЛЛИЗАЦИЯ КАЛИЕВО-ТИТАНОСИЛИКАТНОГО СТЕКЛА ПРИ ТЕРМИЧЕСКОЙ ПОЛЯРИЗАЦИИ С ИСПОЛЬЗОВАНИЕМ РЕЛЬЕФНОГО АНОДА

И. В. Решетов [1,4] ✉, *А. В. Редьков* [1,2], *В. Г. Мелехин* [3], *В. В. Журихина* [1,4], *А. А. Липовский* [1,4]

[1] Санкт-Петербургский академический университет имени Ж. И. Алферова РАН, Санкт-Петербург, Россия;

[2] Институт проблем машиноведения РАН, Санкт-Петербург, Россия;

[3] Физико-технический институт им. А. Ф. Иоффе РАН, Санкт-Петербург, Россия

[4] Санкт-Петербургский политехнический университет Петра Великого, Санкт-Петербург, Россия

✉ reshetov_iv@spbstu.ru

Аннотация. Работа посвящена детальному анализу процесса формирования кристаллических структур в стекле системы K_2O-TiO_2-SiO_2 при полинге с использованием рельефного анода и температуры нагрева ниже температуры стеклования. Кристаллизация стекла при указанных условиях изучена методами комбинационного рассеяния света и механической профилометрии. Обнаружено, что в областях механического контакта электрода со стеклом (выступы профиля на электроде) стекло остается прозрачным без признаков кристаллизации, тогда как в остальных областях, где между электродом и стеклом существует воздушный промежуток, поверхность становится матовой (показано, что это вызвано образованием слоя нанокристаллического анатаза). Между матовой и прозрачной областями, т. е. на краях областей контакта с электродом, формируется переходная область шириной несколько десятков микрометров и высотой несколько микрометров. Обсуждается механизм образования кристаллической фазы и рельефа.

Ключевые слова: стекло, термическая поляризация, профилированный анод, кристаллизация, комбинационное рассеяние света

Финансирование: работа выполнена в рамках Государственного задания «Исследование структур микро- и нанофотоники, формируемых в аморфных диэлектриках под действием сильных полей» (код темы FSRM -2020-001).

Для цитирования: Решетов И. В., Редьков А. В., Мелехин В. Г., Журихина В. В., Липовский А. А. Кристаллизация калиево-титаносиликатного стекла при термической поляризации с использованием рельефного анода // Научно-технические ведомости СПбГПУ. Физико-математические науки. 2022. Т. 15. № 1. С. 30–40. DOI: https://doi.org/10.18721/ JPM.15103

Introduction

The procedure for thermal polarization of glass in an electric field is commonly referred to as thermal poling. This procedure consists of heating a glass plate about 1 mm thick (placed between two metal electrodes or other Class 1 conductors) to a temperature sufficient for activating pronounced conductivity, subsequently applying a DC potential of the order of several hundred volts to the electrodes. The heating temperature for standard soda lime glasses is 250–300 °C, which is significantly lower than the glass transition temperature equal to approximately 550 °C. As the electric field forces the most mobile, positively charged cations (alkali metal ions) to drift from the surface into the bulk of the plate, the composition and structure of the subanodic region of the glass are modified, and a layer of negative space charge appears, generating a strong electric field [1–3].

It is well known that the electric field exerts a considerable influence on the thermodynamics and kinetics of such processes in nanocrystals as phase separation, nucleation and growth, which may serve to either enhance or inhibit crystallization [4–7], in particular by altering the crystalline motifs of the glass [8]. Several papers reported on the surface crystallization of glasses observed under poling and subsequent heat treatment at temperatures above the glass transition: crystallization of barium titanate ($BaTiO_3$) in BaO-TiO_2-TeO_2 system glasses [9], as well as crystobalite (SiO_2) [10], monoclinic dicalcium silicate (β-Ca_2SiO_4) and diopside ($CaMgSi_2O_6$) in silicate glasses [11, 12]. Crystallization of anatase (TiO_2) was also detected in K_2O-TiO_2-SiO_2 system glass under poling below the glass transition temperature but without the additional heat treatment [13] commonly used to produce crystalline nuclei in the glasses [14].

The goal of this study consisted in detailed analysis of the evolution of crystalline structures in K_2O-TiO_2-SiO_2 system glass under poling using a patterned anode at a heating temperature below the glass transition.

Patterned electrodes providing local crystallization of glass under poling offer an alternative to the laser irradiation method generally used to induce local crystallization. We selected a coin to illustrate local crystallization for a surface relief of an imprinted electrode with a rather complex structure.

Crystallization was analyzed by Raman spectroscopy (RS) using a spectrometer equipped with a confocal microscope; the morphology of the glass surface was studied with a mechanical profilometer.

Experimental

The experiment was performed with 4 mm thick plates of commercial LF9 glass with a glass transition temperature T_g = 485 °C and the composition given in Table.

Table

Composition of the glasses used in the experiment

Chemical composition, mol%					
SiO_2	TiO_2	K_2O	Al_2O_3	B_2O_3	As_2O_3
61.80	16.63	16.33	2.06	3.00	0.18

The anode electrode was a coin 16 mm in diameter with a relief height on the surface of the pattern equal to 15 μm. Poling for 60 min was carried out in air at a DC voltage of 850 V and a temperature of 440 °C. The charge that passed through the sample during poling amounted to 3.7 C. The RS spectra were excited with a continuous laser operating at 532 nm and recorded using a Witec Alpha 300R spectrometer equipped with a confocal microscope. The morphology of the sample surface was analyzed with a mechanical Ambios XP-1 Stilus Profiler.

Results and discussion

Fig. 1,*a* shows an optical image for a fragment of the coin imprinted on the glass subjected to poling. The imprint mirrors the pattern on the coin (digits '2006'); the glass remains transparent in the regions where it contacts the protrusions on the coin surface and outside the coin, while the surface becomes frosted in other regions under the coin.

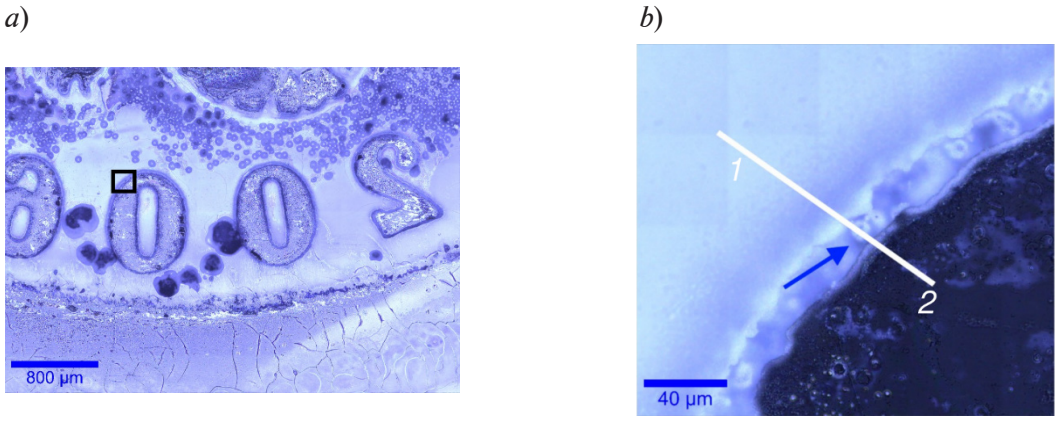

Fig. 1. Optical images of coin fragments imprinted on glass subjected to poling; data are presented in different scales: Fig 1,*b* corresponds to a fragment of glass surface near the digit '0', marked by the square in Fig. 1,*a*. The white line between the frosted (*1*) and transparent (*2*) regions corresponds to the scan line (see Figs. 2–4); the arrow indicates the transition region between *1* and *2*

Fig 1,*b* corresponds to a fragment of glass surface near the digit '0', marked by the square in Fig. 1.*a*. Fig. 1.*b* also shows a transition region containing optical inhomogeneities.

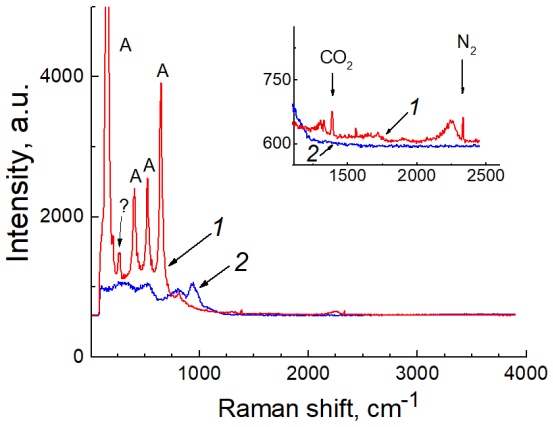

Fig. 2. RS spectra measured in the frosted (*1*) and transparent (*2*) regions of poled glass (see Fig. 1,*b*): peaks of nanocrystalline anatase (A) and lines of atmospheric gases (in the inset) are visible

Fig. 2 shows the RS spectra measured in the frosted (*1*) and transparent (*2*) regions (non-contacting and contacting, respectively, see Fig. 1,*b*).

Spectrum *2* in Fig. 2 is typical for potassium titanosilicate glasses and contains the following broad bands, cm^{-1}:

250–350, 450–550, 700–800,
900–1000, 950–1050;

among these, the bands at 450–550, 950–1050 cm^{-1} correspond to Si–O bonds, and the rest to Ti–O bonds. The bands at 700–800 and 900–1000 cm^{-1} are associated with octahedral and tetrahedral coordination of titanium ions, respectively [15]. Spectrum *1* in Fig. 2 contains several narrow lines belonging to nanocrystalline TiO_2, as well as one line of an unidentified impurity phase (labeled by a question mark) and lines of trace species (see the inset in Fig. 2) [16, 17]. The positions of the lines corresponding to nanocrystalline anatase on the frequency scale and their widths depend on the average size of nanocrystals as well as on the mechanical stresses in the glass [16].

Notably, monocrystalline anatase has six Raman-active fundamentals, cm^{-1} [17]:

144 (E_g), 197 (E_g), 399 (B_{1g}), 516 (A_{1g}), 519 (B_{1g}) and 639 (E_g).

The position of the most intense spectral line of anatase (144 cm^{-1}) and its width (15 cm^{-1}), which depends on the size of the structure where Raman scattering occurs, can be used to estimate the average size of nanocrystals (without taking into account the mechanical stresses) [16].

According to the estimates in [16], the position of the line equal to 150 cm^{-1} corresponds to an average nanocrystal size of 7–10 nm for a spectral width of 15 cm^{-1}. In our case, we can assume that the size of the nanocrystals lies in approximately the same range.

Analyzing the RS spectra in Fig. 3, obtained by scanning the surface along the straight line between the regions *1* and *2* (see Fig. 1,*b*), we can conclude that crystallization occurs before the edge of the digit '0' (including the transition region), where the crystalline phase is represented by TiO_2; after this border is crossed, the glass does not contain signs of crystallization. Notably, no crystallization is observed outside the coin. Surface morphology studies indicate that the transition region forms along the edges of each imprinted digit and consists of protrusions several tens of micrometers wide and several micrometers high.

Fig. 4 shows as an example a profile of the glass surface in the transition region at the border of the digit 0 obtained by a mechanical profiler. Evidently, the transition region is a protrusion about 45 μm wide and 1.5 μm high in this case. Our experiments have revealed that neither a relief nor a crystalline phase are produced under heat treatment in the same mode and using a coin but without applying an electric field.

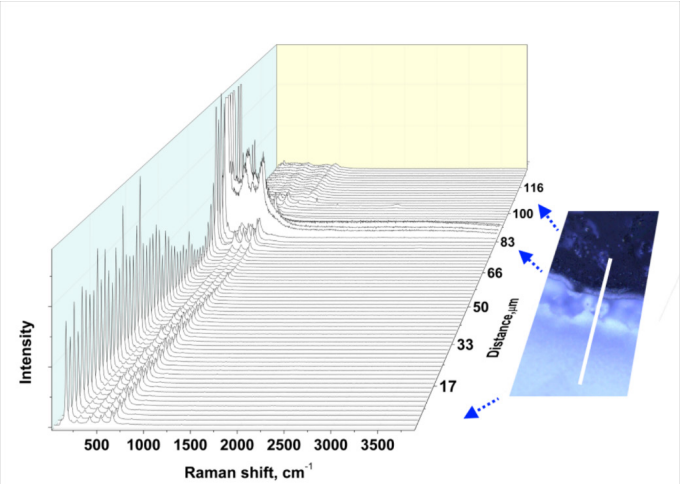

Fig. 3. RS spectra in poled glass for surface scans along a straight line between regions *1* and *2* (see Fig. 1,*b*). Scanning step and range are shown

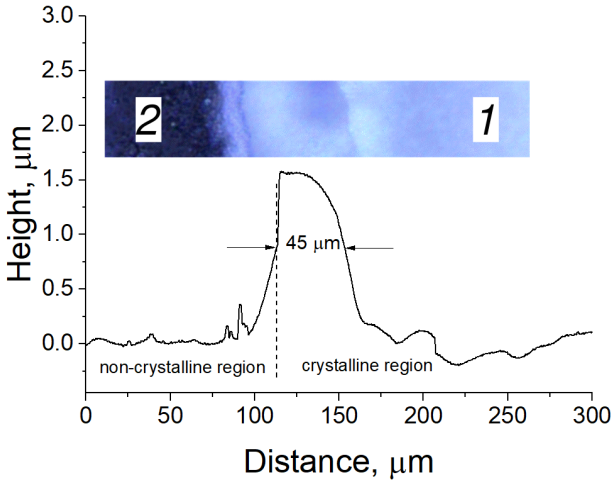

Fig. 4. Surface profile of poled glass in the transition region at the borders of the digit '0' (see Fig. 1,*b*), obtained with a mechanical profiler

We can offer the following explanation for the results obtained. The electric field is applied to the entire region under the coin (electrode) during poling, reaching the highest values in the region where the electrode directly contacts the glass. Alkaline ions from the near-surface region migrate deep into the glass, so that the composition of the glass changes: instead of alkaline ions drifting deeper under the influence of an electric field, hydronium ions (H_3O^+) are injected into the glass from the ambient. Interestingly, hydronium penetrates the region where the electrode contacts the glass less effectively than the region outside the contact. As alkaline ions are removed from the near-surface layer, the ternary $K_2O-TiO_2-SiO_2$ system observed near the glass transition is transformed into a binary TiO_2-SiO_2 system falling into the region of metastable liquid-liquid phase separation (LLPS). It is known that the region below the liquidus occupies almost the entire range of the compositions in the TiO_2-SiO_2 system [18], so that introducing even a small amount of titanium oxide into the silicate system triggers the metastable LLPS. Phase separation into silicon and titanium oxides, as well as crystallization of the latter follow the mechanism of diffusion-controlled phase decomposition within the metastable LLPS region. The crystallization process is affected not only by temperature but also by the molar ratio of the oxides (the higher the silicon oxide content, the higher the required temperature) [19, 20].

In this case, a third parameter, namely, the electric field strength, is added to temperature and molar ratio of oxides. As already noted, the electric field can both enhance and inhibit the phase separation and crystallization processes [4–7]. These processes are enhanced in the TiO_2-SiO_2 system, and the viscosity of the glass is reduced, which may lead to a decrease in the crystallization temperature. Crystallization is likely preceded by LLPS because the surface becomes frosted and starts to scatter light strongly. Strong scattering is due to the large difference in refractive indices between the SiO_2 ($n = 1.46$) and TiO_2 ($n = 2.55$) phases.

In this case, TiO_2 develops under poling at 440 °C, while it only appears at temperatures above 600 °C under thermal annealing of binary TiO_x-SiO_{1-x} glasses ($x = 0.20-0.65$) and films of similar composition ($x = 0.15-0.90$) [19, 20]. The question here is why crystallization is observed at the glass-air interface and is absent at the glass-anode interface. We believe that the difference in the kinetics of ion diffusion at these interfaces plays a central role in this case, because, as it is easier for hydronium to penetrate the glass-air interface, this largely serves to reduce the glass transition temperature, which promotes crystallization. Therefore, the glass does not have sufficient time to crystallize in the experimental conditions due to the low crystallization rate in the region where it contacts the electrode. Our experiments indicate that if the temperature is increased to 460 °C (instead of 440 °C) with the same poling voltage and duration, crystallization extends to the entire region under the coin; this confirms the role played by the kinetic factor in the crystallization process.

Now let us discuss the hypothetical mechanism causing protrusions to appear on the surface of the glass near the interface with the region where it contacts the electrode. The protrusions forming point to a local increase in the glass volume of glass within the given region. The increase in the glass volume is observed as ions with a smaller radius are replaced by ions with a larger radius, for example, during ion exchange, when sodium ions are replaced by potassium ions [21] or during hydrothermal treatment of glass, when vapor bubbles are formed in it [22–24].

It was established in [22–24] that the glass transition temperature T_g of the glasses subjected to hydrothermal treatment is highly dependent on the water content and can decrease to $0.8T_g$ at 1–2 wt.% H_2O and to $0.5T_g$ at 10 wt.% (the temperature T_g is measured in °C). This, in turn, leads to a decrease in the crystallization temperature and a decrease in the viscosity of the glass, additionally affecting the phase separation of vapor [25].

Water vapor bubbles appear in the glasses prepared by the hydrothermal method under annealing at a temperature above the glass transition (as already noted above), and the volume of the glass increases substantially as a result (glass foaming). Therefore, hydrothermal treatment can be used to synthesize porous glasses (see [26] and references therein). Water can also condense in the near-surface region of the glass under poling. The negatively charged non-bridging oxygen atoms O^-, remaining after potassium cations escape, react with H_3O^+ to produce water:

$$\sim Si{-}O^- + H_3O^+ \rightarrow \sim Si{-}OH + H_2O.$$

Replacing potassium cations with hydronium ions cannot lead to an increase in the volume of the glass because of the slight difference in their ionic radii; however, if the glass transition temperature decreases due to increased water content accompanying the penetration of hydronium and turns out to be below the poling temperature, regions with high hydronium contents may favor the generation of vapor bubbles. Since the electric field reaches maximum strength along the perimeter of the electrode relief (edge effect), bubble generation is the most effective along the perimeters of the digits. The most likely reason why protrusions appear on the glass is that vapor bubbles are generated along the borders of the digits.

Thus, a considerable decrease in the glass crystallization temperature with TiO_2 evolving in the near-surface region of the glass under poling can be explained by the effects of the electric field and the water formed in the glass on the thermodynamics and kinetics of crystallization, while the process itself can be characterized as surface crystallization in the electric field.

Conclusion

Considering the poling of $K_2O-TiO_2-SiO_2$ glasses at temperatures below the glass transition of the material with the initial composition and using a patterned anode (imprint), we have discovered that crystalline structures from anatase (TiO_2) nanocrystals, mirroring the pattern on the anode, develop on the surface of the glass. Protrusions appear at the interface between non-crystalline and crystalline regions.

Our findings may be of interest to researchers in the structures with photocatalytic properties and coatings with anatase nanocrystals on the surfaces of titanosilicate glasses.

REFERENCES

1. **Myers R. A., Mukherjee N., Brueck S. R. J.,** Large second-order nonlinearity in poled fused silica, Opt. Lett. 16 (22) (1991) 1732–1734.

2. **Qiu M., Pi F., Orriols G., Bibiche M.,** Signal damping of second-harmonic generation in poled soda-lime silicate glass, J. Opt. Soc. Am. B. 15 (4) (1998) 1362–1365.

3. **Garcia F. C., Carvalho I. C. S., Hering E.,** Inducing a large second-order optical nonlinearity in soft glasses by poling, Appl. Phys. Lett. 72 (25) (1998) 3252–3254.

4. **De Vekey R. C., Majumdar A. J.,** Effect of electric field on phase separation of glass, Nature. 225 (5228) (1970) 172–173.

5. **Kashchiev D.,** Nucleation in external electric field, J. Cryst. Growth. 13–14 (1972), Third International Conference on Crystal Growth (May) 128–130.

6. **Liu W., Liang K. M., Zheng Y. K., et al.,** The effect of an electric field on the phase separation of glasses, J. Phys. D: Appl. Phys. 30 (24) (1997) 3366–3370.

7. **An H., Fleming S.,** Electric field enhanced nanocrystal formation in thermally poled optical fibres, Electron. Lett. 41 (10) (2005) 584–586.

8. **Lipovskii A. A., Tagantsev D. K., Tatarintsev B. V., Vetrov A. A.,** The origin of electrooptical sensitivity of glassy materials: Crystal motifs in glasses, J. Non. Cryst. Solids. 318 (3) (2003) 268–283.

9. **Narazaki A., Tanaka K., Hirao K.,** Poling-induced crystallization of tetragonal BaTiO3 and enhancement of optical second-harmonic intensity in $BaO-TiO_2-TeO_2$ glass system, Appl. Phys. Lett. 75 (21) (1999) 3399–3401.

10. **An H., Fleming S.,** Second-order optical nonlinearity and accompanying near-surface structural modifications in thermally poled soda-lime silicate glasses, J. Opt. Soc. Am. B. 23 (11) (2006) 2303–2309.

11. **Redkov A. V., Melehin V. G., Raskhodchikov D. V., et al.,** Modifications of poled silicate glasses under heat treatment, J. Non. Cryst. Solids. 503–504 (15 January) (2019) 279–283.

12. **Dergachev A., Kaasik V., Lipovskii A., et al.,** Control of soda-lime glass surface crystallization with thermal poling, J. Non. Cryst. Solids. 533 (1 April) (2020) 119899.

13. **Lipovskii A. A., Melehin V. G., Redkov A. V., et al.,** Crystallization of $K_2O-TiO_2-SiO_2$ glass below glass transition by poling, J. Non. Cryst. Solids. 571 (1 November) (2021) 121081.

14. **Malyarevich A. M., Savitsky V. G., Denisov I. A., et al.,** PbS(Se) Quantum dot doped glass applications as laser passive *Q*-switches, Phys. Status Solidi B. 224 (1) (2001) 253–256.

15. **Iwamoto N., Tsunawaki Y., Fuji M., Hatfori T.,** Raman spectra of K_2O-SiO_2 and $K_2O-SiO_2-TiO_2$ glasses, J. Non. Cryst. Solids. 18 (2) (1975) 303–306.

16. **Swamy V., Kuznetsov A., Dubrovinsky L. S., et al.,** Finite-size and pressure effects on the Raman spectrum of nanocrystalline anatase TiO_2, Phys. Rev. B. 71 (18) (2005) 184302.

17. **Ohsaka T., Izumi F., Fujiki Y.,** Raman spectrum of anatase, TiO_2, J. Raman Spectrosc. 7 (6) (1978) 321–324.

18. **Kirillova S. A., Almjashev V. I., Gusarov V. V.,** Phase relationships in the SiO_2-TiO_2 system, Russ. J. Inorg. Chem. 56 (9) (2011) 1464–1471.

19. **Best M. F., Condrate R. A.,** A Raman study of TiO_2-SiO_2 glasses prepared by sol-gel processes, J. Mater. Sci. Lett. 4 (8) (1985) 994–998.

20. **Sankur H., Gunning W.,** Crystallization and diffusion in composite TiO_2-SiO_2 thin films, J. Appl. Phys. 66 (10) (1989) 4747–4751.

21. **Kaneko T.,** Dilation of glass by field-assisted ion exchange, J. Mater. Sci. Lett. 5 (10) (1986) 1011–1012.

22. **Tomozawa M.,** Water in glass, J. Non. Cryst. Solids. 73 (1–3) (1985) 197–204.

23. **Tomozawa M., Takata M., Acocella J., et al.,** Thermal properties of $Na_2O{\cdot}3SiO_2$ glasses with high water content, J. Non. Cryst. Solids. 56 (1–3) (1983) 343–348.

24. **Deubener J., Müller R., Behrens H., Heider J.,** Water and the glass transition temperature of silicate melts, J. Non. Cryst. Solids. 330 (1–3) (2003) 268–273.

25. **Kreidl N. J., Maklad M. S.,** Effect of water content on phase separation in soda-silica glasses, J. Am. Ceram. Soc. 52 (9) (1969) 508–509.

26. **Suzuki M., Maruyama S., Umesaki N., Tanaka T.,** Hydroxyl-group identification using O K-Edge XAFS in porous glass fabricated by hydrothermal reaction and low-temperature foaming, Molecules. 24 (19) (2019) 3488.

СПИСОК ЛИТЕРАТУРЫ

1. **Myers R. A., Mukherjee N., Brueck S. R. J.** Large second-order nonlinearity in poled fused silica // Optics Letters. 1991. Vol. 16. No. 22. Pp. 1732–1734.

2. **Qiu M., Pi F., Orriols G., Bibiche M.** Signal damping of second-harmonic generation in poled soda-lime silicate glass // Journal of the Optical Society of America B. 1998. Vol. 15. No. 4. Pp. 1362–1365.

3. **Garcia F. C., Carvalho I. C. S., Hering E., Margulis W., Lesche W.** Inducing a large second-order optical nonlinearity in soft glasses by poling, Applied Physics Letters. 1998. Vol. 72. No. 25. Pp. 3252–3254.

4. **De Vekey R. C., Majumdar A. J.** Effect of electric field on phase separation of glass // Nature. 1970. Vol. 225. No. 5228. Pp. 172–173.

5. **Kashchiev D.** Nucleation in external electric field // Journal of Crystal Growth. 1972. Vols. 13–14. Third International Conference on Crystal Growth. May. Pp. 128–130.

6. **Liu W., Liang K. M., Zheng Y. K., Gu S. R., Chen H.** The effect of an electric field on the phase separation of glasses // Journal of Physics D: Applied Physics. 1997. Vol. 30. No. 24. Pp. 3366–3370.

7. **An H., Fleming S.** Electric field enhanced nanocrystal formation in thermally poled optical fibers // Electronics Letters. 2005. Vol. 41. No. 10. Pp. 584–586.

8. **Lipovskii A. A., Tagantsev D. K., Tatarintsev B. V., Vetrov A. A.** The origin of electrooptical sensitivity of glassy materials: Crystal motifs in glasses // Journal of Non-Crystalline Solids. 2003. Vol. 318. No. 3. Pp. 268–283.

9. **Narazaki A., Tanaka K., Hirao K.** Poling-induced crystallization of tetragonal $BaTiO_3$ and enhancement of optical second-harmonic intensity in BaO-TiO_2-TeO_2 glass system // Applied Physics Letters. 1999. Vol. 75. No. 21. Pp. 3399–3401.

10. **An H., Fleming S.** Second-order optical nonlinearity and accompanying near-surface structural modifications in thermally poled soda-lime silicate glasses // Journal of the Optical Society of America B. 2006. Vol. 23. No. 11. Pp. 2303–2309.

11. **Redkov A. V., Melehin V. G., Raskhodchikov D. V., Reshetov I. V., Tagantsev D. K., Zhurikhina V. V., Lipovskii A. A.** Modifications of poled silicate glasses under heat treatment // Journal of Non-Crystalline Solids. 2019. Vol. 503–504. 15 January. Pp. 279–283.

12. **Dergachev A., Kaasik V., Lipovskii A., Melehin V., Redkov A., Reshetov I., Tagantsev D.** Control of soda-lime glass surface crystallization with thermal poling // Journal of Non-Crystalline Solids. 2020. Vol. 533. 1 April. P. 119899.

13. **Lipovskii A. A., Melehin V. G., Redkov A. V., Reshetov I. V., Tagantsev D. K.** Crystallization of K_2O-TiO_2-SiO_2 glass below glass transition by poling // Journal of Non-Crystalline Solids. 2021. Vol. 571. 1 November. P. 121081.

14. **Malyarevich A. M.**, **Savitsky V. G., Denisov I. A., Prokoshin P. V., Yumashev K. V., Raaben E., Zhilin A.A., Lipovskii A. A.** PbS(Se) quantum dot doped glass applications as laser passive *Q*-switches // Physica Status Solidi B. 2001. Vol. 224. No. 1. Pp. 253–256.

15. **Iwamoto N., Tsunawaki Y., Fuji M., Hatfori T.** Raman spectra of K_2O-SiO_2 and K_2O-SiO_2-TiO_2 glasses // Journal of Non-Crystalline Solids. 1975. Vol. 18. No. 2. Pp. 303–306.

16. **Swamy V., Kuznetsov A., Dubrovinsky L. S., Caruso R. A., Shchukin G. D., Muddle B. C.** Finite-size and pressure effects on the Raman spectrum of nanocrystalline anatase TiO_2 // Physical Review B. 2005. Vol. 71. No. 18. P. 184302.

17. **Ohsaka T., Izumi F., Fujiki Y.** Raman spectrum of anatase TiO_2 // Journal of Raman Spectroscopy. 1978. Vol. 7. No. 6. Pp. 321–324.

18. **Кириллова С. А., Альмяшев В. И., Гусаров В. В.** Фазовые соотношения в системе SiO_2 – TiO_2 // Журнал неорганической химии. 2011. Т. 56. № 9. С. 1547–1553.

19. **Best M. F., Condrate R. A.** A Raman study of TiO_2-SiO_2 glasses prepared by sol-gel processes // Journal of Materials Science Letters. 1985. Vol. 4. No. 8. Pp. 994–998.

20. **Sankur H., Gunning W.** Crystallization and diffusion in composite TiO_2 -SiO_2 thin films // Journal of Applied Physics. 1989. Vol. 66. No. 10. Pp. 4747–4751.

21. **Kaneko T.** Dilation of glass by field-assisted ion exchange // Journal of Materials Science Letters. 1986. Vol. 5. No. 10. Pp. 1011–1012.

22. **Tomozawa M.** Water in glass // Journal of Non-Crystalline Solids. 1985. Vol. 73. No. 1–3. Pp. 197–204.

23. **Tomozawa M., Takata M., Acocella J., Watson E. B., Takamori T.** Thermal properties of $Na_2O{\cdot}3SiO_2$ glasses with high water content // Journal of Non-Crystalline Solids. 1983. Vol. 56. No. 1–3. Pp. 343–348.

24. **Deubener J.**, **Müller R., Behrens H., Heider J.** Water and the glass transition temperature of silicate melts // Journal of Non-Crystalline Solids. 2003. Vol. 330. No. 1–3. Pp. 268–273.

25. **Kreidl N. J., Maklad M. S.** Effect of water content on phase separation in soda-silica glasses // Journal of the American Ceramic Society. 1969. Vol. 52. No. 9. Pp. 508–509.

26. **Suzuki M., Maruyama S., Umesaki N., Tanaka T.** Hydroxyl-group identification using O K-Edge XAFS in porous glass fabricated by hydrothermal reaction and low-temperature foaming // Molecules. 2019. Vol. 24. No. 19. P. 3488.

THE AUTHORS

RESHETOV Ilya V.
Alferov University,
Peter the Great St. Petersburg Polytechnic University
8/3 Khlopina St., St. Petersburg, 194021, Russia
reshetov_iv@spbstu.ru
ORCID: 0000-0002-8661-3654

REDKOV Alexey V.
Alferov University,
Institute of Problems of Mechanical Engineering, RAS
61 Bolshoi Pr. V. I., St. Petersburg, 199178, Russia
red-alex@mail.ru
ORCID: 0000-0002-2748-6966

MELEHIN Vladimir G.
Ioffe Physical Technical Institute of the Russian Academy of Sciences
26 Polytekhnicheskaya St., St. Petersburg, 194021, Russia
melekhin1952@gmail.com
ORCID: 0000-0003-3741-3936

ZHURIKHINA Valentina V.
Peter the Great St. Petersburg Polytechnic University,
Alferov University
29 Politechnicheskaya St., St. Petersburg, 195251, Russia
jourikhina@mail.ru
ORCID: 0000-0003-0685-9409

LIPOVSKII Andrey A.
Alferov University,
Peter the Great St. Petersburg Polytechnic University
8/3 Khlopina St., St. Petersburg, 194021, Russia
lipovskii@mail.ru
ORCID: 0000-0001-9472-9190

СВЕДЕНИЯ ОБ АВТОРАХ

РЕШЕТОВ Илья Валентинович – *инженер Лаборатории оптики гетерогенных структур и оптических материалов Санкт-Петербургского академического университета имени Ж. И. Алферова Российской академии наук; инженер научно-образовательного центра «Физика и технология гетерогенных материалов и наногетероструктур» Санкт-Петербургского политехнического университета Петра Великого.*
194021, Россия, г. Санкт-Петербург, ул. Хлопина, 8, к. 3
reshetov_iv@spbstu.ru
ORCID: 0000-0002-8661-3654

РЕДЬКОВ Алексей Викторович – *кандидат физико-математических наук, старший научный сотрудник Института проблем машиноведения РАН, Санкт-Петербург, Россия; младший научный сотрудник Лаборатории оптики гетерогенных структур и оптических материалов Санкт-Петербургского академического университета имени Ж. И. Алферова Российской академии наук.*
199178, Россия, г. Санкт-Петербург, Большой проспект В. О., 61.
red-alex@mail.ru
ORCID: 0000-0002-2748-6966

МЕЛЕХИН Владимир Герасимович – *доктор физико- математических наук, профессор Физико-технического института имени А. Ф. Иоффе РАН.*
194021, Россия, г. Санкт-Петербург, Политехническая ул., 26
melekhin1952@gmail.com
ORCID: 0000-0003-3741-3936

ЖУРИХИНА Валентина Владимировна – *доктор физико-математических наук, профессор Высшей школы фундаментальных физических исследований Физико-механического института Санкт-Петербургского политехнического университета Петра Великого; профессор кафедры физики и технологии наногетероструктур Санкт-Петербургского академического университета имени Ж. И. Алферова Российской академии наук.*
195251, Россия, г. Санкт-Петербург, Политехническая ул., 29
jourikhina@mail.ru
ORCID: 0000-0003-0685-9409

ЛИПОВСКИЙ Андрей Александрович – *доктор физико-математических наук, профессор, заведующий кафедрой физики и технологии наногетероструктур Санкт-Петербургского академического университета имени Ж. И. Алферова Российской академии наук; профессор Высшей инженерно-физической школы Санкт-Петербургского политехнического университета Петра Великого.*
194021, Россия, г. Санкт-Петербург, ул. Хлопина, 8, к. 3
lipovskii@mail.ru
ORCID: 0000-0001-9472-9190

Received 26.02.2022. Approved after reviewing 09.03.2022. Accepted 09.03.2022.
Статья поступила в редакцию 26.02.2022. Одобрена после рецензирования 09.03.2022. Принята 09.03.2022.

Original article
DOI: https://doi.org/10.18721/JPM.15104

AN INVERSE PROBLEM FOR GENERALIZED RADON TRANSFORMATION

D. S. Anikonov ✉, *E. Yu. Balakina, D. S. Konovalova*
Sobolev Institute of Mathematics, Novosibirsk, Russia

✉ anik@math.nsc.ru

Abstract: The paper studies the problem of inverting the integral transformation of Radon, whose formula, under traditional restrictions, gives the integrand values at any point. For the case when such a function is discontinuous and depends not only on the points of 3D space, but also on the parameters characterizing the plane of integration, these integrals have been named the generalized Radon transform (GRT). For the GRT inversion problem, the matching between quantities of known variables and variables of the integrand did not allow us to fully find the desired function. In this paper, only a part of such a function was selected, namely, the discontinuity surface of the integrand for the GRT. An algorithm for solving the problem was put forward, and it was supported by a concrete example.

Keywords: generalized Radon transformation, integral geometry, differential equations, discontinuous functions

Citation: Anikonov D. S., Balakina E. Yu., Konovalova D. S., An inverse problem for generalized Radon transformation, St. Petersburg Polytechnical State University Journal. Physics and Mathematics. 15 (1) (2022) 41–51. DOI: https://doi.org/10.18721/JPM.15104

Научная статья
УДК 517.958
DOI: https://doi.org/10.18721/JPM.15104

ОБРАТНАЯ ЗАДАЧА ДЛЯ ОБОБЩЕННОГО ПРЕОБРАЗОВАНИЯ РАДОНА

Д. С. Аниконов ✉, *Е. Ю. Балакина, Д. С. Коновалова*

Институт математики им. С. Л. Соболева СО РАН, г. Новосибирск, Россия

✉ anik@math.nsc.ru

Аннотация. В работе исследуется проблема обращения интегрального преобразования Радона, формула которого при традиционных ограничениях дает значения подынтегральной функции в любой точке. Для случая, когда подобная функция является разрывной и зависит не только от точек трехмерного пространства, но и от параметров, характеризующих плоскость интегрирования, эти интегралы названы обобщенным преобразованием Радона (ОПР). Для задачи обращения ОПР сопоставление количества переменных известных величин и подынтегрального выражения не позволяет полностью найти искомую функцию. В этой статье выбрана лишь часть такой функции, а именно поверхность разрывов подынтегральной функции для ОПР. Предложен алгоритм решения поставленной задачи, который подкреплен конкретным примером.

Ключевые слова: обобщенное преобразование Радона, интегральная геометрия, дифференциальное уравнение, разрывная функция

Для цитирования: Аниконов Д. С., Балакина Е. Ю., Коновалова Д. С. Обратная задача для обобщенного преобразования Радона // Научно-технические ведомости СПбГПУ. Физико-математические науки. 2022. Т. 15. № 1. С. 41–51. DOI: https://doi.org/10.18721/JPM.15104

Introduction

This paper addresses a problem from the theory of integral geometry on obtaining information about the integrand function from a certain set of integrals over this function. Such a general statement includes many particular cases. The most well-known are the problems on inverting the ray transform and the Radon transform. Aside from purely academic interest, the findings of studies on such problems have major practical implications. The best-known applied example is the mathematical formulation of X-ray tomography theory. In this regard, it is notable that many probing problems are specifically reduced to the problems of integral geometry.

While we do not claim to provide an exhaustive overview of the topic, we draw attention to studies of such renowned scholars in this field as Johann Radon [1], Richard Courant [2], Fritz John [3], and Israel Gelfand [4]. Furthermore, the circle of mathematicians surrounding Lavrentyev contributed significantly to resolving these issues in connection with inverse problems of mathematical physics [5].

Research in this direction is ongoing, even though comparatively fewer studies have been published in recent years. Notable examples include [6–14]. The bulk of the results on this topic attempt to determine the entire integrand; this means that rather stringent constraints have to be introduced, limiting potential wider applications. In addition, the integrand may depend on a large number of variables in some important applied problems, making it impossible to find this entire expression from the available information. This is the case, for example, in X-ray tomography, if the effect of particle scattering in the material scanned is fully taken into account. For this reason, the problem statement has to be modified, e.g., only the discontinuity surfaces of the integrand are regarded as the desired object. Notably, the information about such surfaces provides a satisfactory representation of the medium examined in imaging problems. In particular, these data serve as the main characteristics in X-ray tomography. It bears mentioning that this approach to the problems of X-ray tomography was taken earlier, for example, in [15–17], where integration was carried out along one-dimensional manifolds, while the desired object in our study is the discontinuity surface for the case of integration along two-dimensional manifolds. To the best of our knowledge, no other authors have discussed similar problems.

Definitions and problem statement

We adopted the following notation: E^3 is the three-dimensional Euclidean space with the coordinate system $Ox_1x_2x_3$, corresponding to the orthonormal basis e_1, e_2, e_3; Ω is a unit sphere in E^3,

$$\Omega = \left\{\omega : \omega \in \mathbb{R}^3, |\omega| = 1\right\},$$

$$\omega = \omega(\theta, \gamma) = (\sin\theta\cos\gamma, \sin\theta\sin\gamma, \cos\theta),$$

θ, γ are the spherical angles; $L(x,\omega)$ is the ray emanating from point $x \in E^3$ in the direction ω, $L(x,\omega) = \{y: y = x + t\omega, t \geq 0\}$; *const* is a positive number; Δ_x is the Laplace operator with respect to the variable x

For any open set $T \subset E^3$, $C^k(T)$ is a set of bounded functions defined in T, continuous together with all its partial derivatives up to and including the kth order; ∂T is the boundary of the set T.

We consider a bounded domain G in space E^3, containing the pairwise disjoint domains G_i ($i = 1, 2,..., p$), such that the equality $\overline{G}_0 = \overline{G}$ is satisfied for their union G_0. We assume that each set ∂G_i, ($i = 1, 2,..., p$) is a continuous two-dimensional surface. Evidently, $\partial G_0 = \partial G_1 \cup ... \cup \partial G_p$. Let us assume that the system of sets $\{G_i\}$, ($i = 1, 2,..., p$) is generally convex in the following sense: for any point $x \in E^3$ and for all $\omega \in \Omega$, the ray $L(x,\omega)$ crosses the boundary ∂G_0 of set G_0 in no more than a finite number of points. For convenience of notation, let us assume that the system of sets G_i, ($i = 1, 2,..., p$) is supplemented by an unbounded domain $G_{p+1} = E^3 \backslash \overline{G}$. Let us call the point $z \in \partial G_0$ contact if it is boundary for two and only two sets G_j and G_l, so that $1 \leq j$, $l \leq p + 1$. Moreover, it is assumed that the set of contact points is dense in ∂G_0.

Consider a family of functions $F(x,y)$ and $f(y)$, $x, y \in E^3$, satisfying the inequalities:

$$|F(x,u) - F(x,v)| \leq const\,|u - v|, \; x,u,v \in E^3;$$

$$|f(u) - f(v)| \leq const\,|u - v|, \; u,v \in G_i.$$

In this case, the function $F(x,y)$ belongs to the class C^2 ($E^3 \times E^3$), and $f(y)$ equals zero outside the domain G. Apparently, such functions $f(y)$ have finite boundary values at points $y = z$, $z \in \partial G_i$, which we denote below as $[f(z)]_i$, i.e., $f(y) \to [f(z)]_i$, $y \in G_i$, $y \to z$. The magnitude of the discontinuity (jump) of the function $f(y)$ at the contact point $y = z$ is the difference

$$\left[f(z)\right]_{j,l} = \left[f(z)\right]_j - \left[f(z)\right]_l,\ z \in \partial G_j, z \in \partial G_l, 1 \le l < j \le p+1.$$

Definition. *The function* $I(x,\omega)$ *given by the equality*

$$I(x,\omega)(f) = \int\limits_{(y-x,\omega)=0} F(x,y) f(y) d_y\sigma,\ x \in E^3, \omega \in \Omega, \tag{1}$$

is called the generalized Radon transform of the function $f(y)$.

We should clarify that the first-kind surface integral in Eq. (1) is taken over a plane normal to the vector ω and passing through the point x.

If $F(x,y) = 1$, the set of values of the function $I(x,\omega)$ and the set of values of the classical Radon transform coincide. Broadly speaking, there are several different definitions of generalized Radon transforms. Our case is peculiar in that discontinuous integrands are used, depending not only on integration variables but also on additional variables.

We have been unable to uncover any equivalents for this definition in the literature. Let us prove that it is correct. Consider an orthogonal transformation of A to E^3 that has the property

$$A\omega = \omega^*,\ \omega = (\sin\theta\cos\gamma, \sin\theta\sin\gamma, \cos\theta),\ \omega^* = e_3, \omega^* = (0,0,1).$$

This transformation can be obtained by sequentially performing two rotations: the first is the rotation around the axis Ox_3 by the angle γ, the second is around the axis Ox_2 by the angle θ.

It is easy to verify that the matrix Λ of the transformation A and the matrix Λ^{-1} of the transformation A^{-1} take the following form:

$$\Lambda = \begin{pmatrix} cos\theta\cos\gamma & \cos\theta\sin\gamma & -\sin\theta \\ -\sin\gamma & \cos\gamma & 0 \\ \sin\theta\cos\gamma & \sin\theta\sin\gamma & \cos\theta \end{pmatrix},$$

$$\Lambda^{-1} = \begin{pmatrix} \cos\theta\cos\gamma & -\sin\gamma & \sin\theta\cos\gamma \\ \cos\theta\sin\gamma & \cos\gamma & \sin\theta\sin\gamma \\ -\sin\theta & 0 & \cos\theta \end{pmatrix}.$$

Let us describe the set of vectors w from the sphere Ω, orthogonal to the vector ω. To do this, we apply the transformation A^{-1} with the property $\omega = A^{-1}\omega^*$ to horizontal vectors $(\cos\alpha, \sin\alpha, 0)$. As a result, we obtain:

$$w(\theta,\gamma,\alpha) = (\cos\theta\cos\gamma\cos\alpha - \sin\gamma\sin\alpha, \cos\theta\sin\gamma\cos\alpha + \cos\gamma\sin\alpha, -\sin\theta\cos\alpha). \tag{2}$$

We introduce the polar coordinate system (r,α), centered at point x, in the plane passing through the point x and normal to the vector ω. Then, moving on to integration in polar coordinates, equality (1) is rewritten in the following form:

$$I(x,\omega)(f) = \int\limits_0^{2\pi}\int\limits_0^{\infty} rF\left(x, x + rw(\theta,\gamma,\alpha)\right) f\left(x + rw(\theta,\gamma,\alpha)\right) dr d\alpha. \tag{3}$$

We consider the function

$$g(x,r,\theta,\gamma,\alpha) = rF\left(x, x + rw(\theta,\gamma,\alpha)\right) f\left(x + rw(\theta,\gamma,\alpha)\right),$$

which, for any fixed values of x, θ, γ, has no more than a finite number of discontinuities with respect to the variable r for any given α, which is provided by the generalized convexity condition. Thus, the integrand in equality (3) is continuous almost everywhere in the integration domain, which ensures the existence of the integral. The constraints on the integral follow from the constraints on the domain G and the functions F, f. Following the above steps in the reverse order, that is, from equality (3) to equality (1), we confirm that the definition of the generalized Radon transform is correct.

Now let us prove the continuity of function $I(x,\omega)(f)$. We fix an arbitrary point (x,ω), so that $\{x_k,\omega_k\}$, $\omega_k = \omega(\theta_k,\gamma_k)$ is a sequence of points converging to (x,ω).

We consider the functions

$$\chi_k(r,\alpha) = rF\left(x_k, x_k + rw(\theta_k,\gamma_k,\alpha)\right) f\left(x_k + rw(\theta_k,\gamma_k,\alpha)\right),$$
$$\chi(r,\alpha) = rF\left(x, x + rw(\theta,\gamma,\alpha)\right) f\left(x + rw(\theta,\gamma,\alpha)\right).$$

Imposing the condition of generalized convexity again, we establish that $\chi_k(r,\alpha)$ tends to the function $\chi(r,\alpha)$ for almost all r, α. Therefore, according to the Lebesgue theorem, we allow a pass to the limit under the integral sign, i.e.,

$$I(x_k,\omega_k)(f) = \int_0^{2\pi}\int_0^{\infty} \chi_k(r,\alpha)\,dr\,d\alpha \to \int_0^{2\pi}\int_0^{\infty} \chi(r,\alpha)\,dr\,d\alpha = I(x,\omega)(f),$$

which in fact implies continuity of the function $I(x,\omega)(f)$.

Let us formulate the following problem of integral geometry.

Problem of the unknown boundary. *The set ∂G_0 can be found from Eq. (1), if only the values of the following function are known:*

$$I(x,\omega)(f),\ x \in \mathrm{E}^3,\ \omega \in \Omega.$$

Evidently, while a family of integrals is given in this problem, it is required to find a set of potential discontinuity points of an unknown integrand. This statement of the problem elaborates on our previous papers; the difference lies in the dimension of the integration set and in the fact that the domain G is not assumed to be known in this case. We should note that the range of problems dealing with the search for unknown boundaries is fairly extensive, covering diverse areas of mathematics. The earliest statement is perhaps the well-known Stefan problem.

Construction of the algorithm for solving the problem

Consider the following function:

$$J(x,\omega,p)(f) = \int_{(y,\omega)=p} F(x,y) f(y)\,d_y\sigma,\ x \in \mathrm{E}^3,\ \omega \in \Omega,\ -\infty < p < +\infty. \tag{4}$$

The integral here is taken over a plane orthogonal to vector ω and deviating from the origin by p. If $F(x,y) = 1$, then $J(x,\omega,p)(f)$ is independent of x and coincides with the traditional Radon transform, which we denote as $R(\omega,p)(f)$. It is easy to see that the functions $I(x,\omega)(f)$ and $J(x,\omega,p)(f)$ are related by the equality

$$J(x,\omega,x\cdot\omega)(f) = I(x,\omega)(f),$$

i.e., they coincide if we assume that $p = x\cdot\boldsymbol{\omega}$.

It follows then that the functions $J(x,\omega,p)(f)$, $R(\omega,p)(f)$ are continuous because the function $I(x,\omega)(f)$ is continuous. Notice also that any transformation $R(\omega,p)(h)$ is also continuous if the function $h(y)$ satisfies the same conditions as the function $f(y)$, i.e.,

$$|h(u) - h(v)| \le const\,|u - v|,\ u,v \in G_i, i = 1,\ldots,p,\ h(y) = 0,\ y \in G_{p+1}.$$

Let us prove one useful property for the Radon transform of the function $h(y)$. Here we use a small excerpt of the proof for some assumption from monograph [3], which we summarize to the case of a discontinuous integrand $h(y)$.

Consider the integral

$$H(x) = \int_G \int_\Omega h(y) \left|(y - x, \omega)\right| d\omega dy.$$

We need the following known, easily verifiable equations:

$$\begin{gathered} \Delta_x \left|y - x\right| = 2\left|y - x\right|^{-1}, \int_\Omega \left|\xi \cdot \omega\right| d\omega = 2\pi \left|\xi\right|, \xi \in \mathrm{E}^3, \\ \Delta_x \int_G \frac{h(y)}{\left|y - x\right|} dy = -4\pi h(x). \end{gathered} \tag{5}$$

Using the first two formulas in (5) to transform the integral $H(x)$, we obtain:

$$\Delta_x H(x) = 4\pi \int_G \frac{h(y)}{\left|y - x\right|} dy. \tag{6}$$

The same relation can be expressed in terms of the Radon transforms by changing the order of integration and using the Fubini theorem:

$$H(x) = \int_\Omega \int_G h(y) \left|(y - x) \cdot \omega\right| dy d\omega = \int_\Omega \int_{-\infty}^{+\infty} \left|p\right| \int_{(y-x)\cdot\omega = p} h(y) d_y \sigma dp d\omega = \int_\Omega \int_{-\infty}^{+\infty} \left|p\right| R(\omega, p + x \cdot \omega)(h) dp d\omega,$$

Consider the expression

$$\Delta_x H(x) = \int_\Omega \Delta_x \int_{-\infty}^{+\infty} \left|p\right| R(\omega, p + x \cdot \omega)(h) dp d\omega. \tag{7}$$

We transform the inner integral in Eq. (7), using the property $R(\omega,h)(h) = R(-\omega,-h)(h)$:

$$\begin{gathered} \Delta_x \int_{-\infty}^{+\infty} \left|p\right| R(\omega, p + x \cdot \omega)(h) dp = \\ = \Delta_x \left[\int_{x\cdot\omega}^{+\infty} (p - x \cdot \omega) R(\omega, p + x \cdot \omega)(h) dp - \int_{-\infty}^{x\cdot\omega} (p - x \cdot \omega) R(\omega, p + x \cdot \omega)(h) dp \right] = \\ = 2R(\omega, x \cdot \omega)(h). \end{gathered} \tag{8}$$

It follows then that

$$\Delta_x H(x) = 2 \int_\Omega R(\omega, x \cdot \omega)(h) d\omega.$$

Comparing the obtained equality with equality (6), we derive the formula

$$\int_\Omega R(\omega, x \cdot \omega)(h) d\omega = 2\pi \int_G \frac{h(y)}{\left|y - x\right|} dy. \tag{9}$$

Notice that integration in equality (9) is carried out over the variables y, ω, while the variable x remains unchanged. This allows to assume that x here is a parameter expanding the range of application for Eq. (9). Namely, given a fixed value of x, we can regard the product $F(x,y)f(h)$ as some function $h(y)$ and assume that

$$R\left(\omega, x\cdot\omega\right)\left(h\right) = I\left(x,\omega\right)\left(f\right).$$

Then it follows from equality (9) that

$$\int_{\Omega} I\left(x,\omega\right)\left(f\right)d\omega = 2\pi\int_{G}\frac{F(x,y)f(y)}{\left|y-x\right|}dy. \tag{10}$$

Applying the Laplace operator to equality (10), we obtain:

$$\begin{gathered}\Delta_x\int_{\Omega} I\left(x,\omega\right)\left(f\right)d\omega = \\ = 2\pi\Delta_x\int_{G}\frac{F\left(x,x\right)f(y)}{\left|y-x\right|}dy + 2\pi\Delta_x\int_{G}\frac{(F(x,y)-F\left(x,x\right))f(y)}{\left|y-x\right|}dy.\end{gathered} \tag{11}$$

To transform the first term in the right-hand side of equality (11), we select the integral, where only the denominator $|y - x|^{-1}$ is differentiated, and, using for it the last equality in relations (5), we obtain the representation:

$$2\pi\Delta_x\int_{G}\frac{F\left(x,x\right)f(y)}{\left|y-x\right|}dy = -8\pi^2F\left(x,x\right)f\left(x\right)+\Phi_1\left(x\right).$$

Here, the function $\Phi_1(x)$ is a linear combination of the integrals over the variable y of functions

$$\beta\left(x,y\right)f\left(y\right)\left|y-x\right|^{-\alpha},\ \alpha=1,2,\ \beta\left(x,y\right)\in C^0\left(\mathrm{E}^3\times\mathrm{E}^3\right),$$

i.e., potential-like integrals with a weak singularity.

The general properties of such integrals imply continuity and boundedness of $\Phi_1(x)$. Clearly, by virtue of inequality

$$\left|F(x,u)-F\left(x,v\right)\right|\le const\left|u-v\right|,\ x,u,v\in\mathrm{E}^3,$$

the second term in the right-hand side of Eq. (11), denoted by $\Phi_2(x)$, is also a combination of potential-like integrals with a weak singularity and a continuous bounded function.

These considerations lead to the following formula:

$$\Delta_x\int_{\Omega} I\left(x,\omega\right)\left(f\right)d\omega = -8\pi^2F\left(x,x\right)f\left(x\right)+\Phi\left(x\right), \tag{12}$$

where $\Phi(x) = \Phi_1(x) + \Phi_2(x)$.

Equality (12) serves as a basis for constructing an algorithm for solving the problem, comprising the following steps.

Step 1. Integrate the known function $I(x,\omega)$ over $\omega \in \Omega$.

Step 2. Apply the Laplace operator Δ_x to the resulting expression.

Step 3. Analyze the function $\Delta_x\int_{\Omega} I\left(x,\omega\right)\left(f\right)d\omega$ and indicate its discontinuity points that coincide with the discontinuity points of the function $f(x)$.

Comment on the algorithm presented. The left-hand side of Eq. (12) is known from the problem statement, and the right-hand side has first-kind discontinuities only at contact points $z \in \partial G_0$, provided that $F(x,x) \neq 0$, $x \in E^3$, $[f(z)]_{j,l} \neq 0$, which we assume to be satisfied. Thus, we find a set of all contact points in ∂G_0 and, by virtue of its density in ∂G_0, determine this entire set.

Note that Eq. (12) for the case $F(x,y) = 1$, $f(y) \in C^1(E^3)$ coincides with the known formula for inversion of the classical Radon transform [3]. The result we obtained therefore in a sense builds on the result above. Comparing the algorithm that we obtained with other algorithms, we can see that the integrands are assumed to be smooth in all known formulas for the inverse Radon transform so that it is possible to differentiate them. If we attempt to apply such algorithms to discontinuous functions (e.g., meaning differentiation in a generalized sense), new terms such as the δ-function appear, with unforeseen complications for further analysis.

Particular case

Let us consider the case when the given object is a ball with a unit radius (1.0) centered at the origin, containing an inhomogeneity, namely a ball 0.5 in radius also centered at the origin. Therefore,

$$G = \{x \in E^3 : |x| < 1\},\ G = \overline{G_1} \cup G_2,$$
$$G_1 = \{x \in E^3 : |x| < 0.5\},\ G_2 = \{x \in E^3 : 0.5 < |x| < 1\}.$$

For the sake of simplicity, let us assume that $F(x,y) = 1$, and the function f is piecewise constant:

$$f(x) = \begin{cases} f_1, |x| < 0.5, \\ f_2, 0.5 < |x| < 1. \end{cases}$$

It is evident that all the requirements of this problem are satisfied, including the condition of generalized convexity for the discontinuity surface.

Then the integral over the plane, i.e., $I(x,\omega)$, takes the following form:

$$\int\limits_{(y-x,\omega)=0} f(y) d_y\sigma = \begin{cases} \pi f_1(0.25 - (\omega \cdot x)^2) + 0.75\pi f_2, |\omega \cdot x| < 0.5, \\ \pi f_2(1 - (\omega \cdot x)^2), 0.5 < |\omega \cdot x| < 1. \end{cases}$$

Next, we integrate it over a unit sphere. For this purpose, we adopt a spherical coordinate system and divide the integration into two parts, so that the planes intersect the domains G_1 and G_2 in one part, and only the set G_2 in the other. As a result, we obtain the equality

$$\int\limits_{\Omega} I(x,\omega) d\omega = \begin{cases} 4\pi^2 (0.25 f_1 + 0.75 f_2 - \dfrac{f_1 |x|^2}{3}), |x| < 0.5, \\ 4\pi^2 \left(f_2 - \dfrac{f_2 |x|^2}{3} + \dfrac{2(f_1 - f_2)}{3|x|} \right), 0.5 < |x| < 1. \end{cases}$$

We calculate the Laplacian of this integral:

$$\Delta_x \int\limits_{\Omega} I(x,\omega) d\omega = \begin{cases} -8\pi^2 f_1, |x| < 0.5, \\ -8\pi^2 f_2, 0.5 < |x| < 1. \end{cases} \tag{13}$$

Evidently, the latter expression is a discontinuous function if $f_1 \neq f_2$, and the desired surface is a sphere with a radius of 0.5 centered at the origin.

The outcome is consistent with the conclusions of the general theory, which indirectly supports our assumptions.

Conclusion

The study we have carried out is theoretical in nature, confirming that an unknown boundary can in fact be found, which can be a useful tool for developing the theory on scanning various media by physical signals. We intend to discuss the numerical implementations of the algorithm in our future research. Since it is important to adopt the weakest constraints possible for wider practical applications, we allowed for a case of a discontinuous integrand in the generalized Radon transform, depending on multiple variables. Unfortunately, we are still forced to confine our analysis to the condition of generalized convexity for discontinuity surfaces. The results obtained can serve for further relaxing the constraints and increasing the efficiency of the developed algorithm.

REFERENCES

1. **Helgason S.,** The Radon transform, 2nd edition, (Progress in mathematics. Vol. 5), Springer Science, Cambridge, USA, 1927.

2. **Courant R.,** Partial differential equations, Interscience, France, 1962.

3. **John F.,** Plane waves and spherical means applied to partial differential equations, Springer, New York, 1981.

4. **Gelfand I. M., Grayev M. I., Vilenkin N. Ya.,** Integral geometry and representation theory (Generalized Functions, Vol. 5), Translated by Saletan E. J., Elsevier Inc. All, 1966.

5. **Lavrent'ev M. M., Savel'ev L. Ya.,** Operator theory and ill-posed problems: Posed problems (Inverse and ill-posed problems), Brill Academic Publishers, Leyden, Netherlands, 2006.

6. **Koganov A. V.**, The task of integral geometry with measure induction, Computer Research and Modeling. 3 (1) (2011) 31–37 (in Russian).

7. **Kalnin T. G., Ivonin D. A., Abrosimov K. N., et al.,** Analysis of tomographic images of the soil pore space structure by integral geometry methods, Eurasian Soil Sci. 54 (9) (2021) 1400–1409.

8. **Lyakhov L. N., Lapshina M. G., Roshchupkin S. A.,** Support theorem for the Radon – Kipriyanov K_γ - transform, Itogi Nauki i Tekhn. Ser. Sovrem. Mat. Pril. Temat. Obz. 171 (2019) 118–124 (in Russian).

9. **Temirgaliyev N., Abikenova Sh. K., Azhgaliyev Sh. U., Taugynbayeva G. E.,** The Radon transform in the scheme C(N)D-inverstigations and the quasi-Monte Carlo theory, Russian Math. (Iz. VUZ). 64 (3) (2020) 87–92.

10. **Bayev A. V.,** Radon transform for solving an inverse scattering problem in a planar layered acoustic medium, Comput. Math. Math. Phys. 58 (4) (2018) 537–547.

11. **Simonov E. N., Prokhorov A. V., Akintseva A. V.,** Mathematical modelling of reconstruction of volumetric images in X-ray computed tomography using holographic methods, Vestnik YuUrGU. Ser. Mat. Model. Progr. 12 (3) (2019) 102–114 (in Russian).

12. **Derevtsov E. Yu., Volkov Yu. S., Schuster T.,** Differential equations and uniqueness theorems for the generalized attenuated ray transforms of tensor fields, In book: Numerical computations: Theory and algorithms, Part II. Sergeyev Ya. D., Kvasov D. E. (Eds.); Lecture Notes in Computer Science. 11974 (2020) 97–111.

13. **Svetov I. E.,** The method of approximate inverse for the Radon transform operator acting on vector and symmetric 2-tensor fields in R^3, Siberian Electronic Mathematical Reports. 17 (2020) 1073–1087 (in Russian).

14. **Polyakova A. P.,** Singular value decomposition of a normal Radon transform operator acting on 3D symmetric 2-tensor fields, Siberian Electronic Mathematical Reports. 18 (2) (2021) 1572–1595.

15. **Anikonov D. S., Prokhorov I. V., Kovtanyuk A. E.,** Investigation of scattering and absorbing media by methods of X-ray tomography, J. Inv. Ill-Posed Probl. 1 (4) (1993) 259–281.

16. **Vainberg E. I., Kazak I. A., Faingoiz M. L.**, X-ray computerized back projection tomography with filtration by double differentiation. Procedure and information features, Soviet J. Nondest. Test. 21 (2) (1985) 106–113.

17. **Derevtsov E. Y., Maltseva S. V., Svetov I. E.,** Determination of discontinuities of a function in a domain with refraction from its attenuated ray transform, J. Appl. Ind. Math. 12 (4) (2018) 619–641.

СПИСОК ЛИТЕРАТУРЫ

1. **Хелгасон С.** Преобразование Радона. Пер. с англ. М.: Мир, 1983. 152 с.

2. **Курант Р.** Уравнения с частными производными. Пер. с англ. М.: Мир, 1964. 832 с.

3. **Йон Ф.** Плоские волны и сферические средние в применении к дифференциальным уравнениям с частными производными. М.: Изд-во иностранной литературы, 1958. 160 с.

4. **Гельфанд И. М., Граев М. И., Виленкин Н. Я.** Интегральная геометрия и связанные с ней вопросы теории представлений. М.: Физматгиз, 1962. 656 с.

5. **Лаврентьев М. М., Савельев Л. Я.** Теория операторов и некорректные задачи. 2-е изд., перераб. и доп. Новосибирск: Изд-во Института математики, 2010. 912 с.

6. **Коганов А. В.** Задача интегральной геометрии с мероиндукцией // Компьютерные исследования и моделирование. 2011. Т. 3. № 1. С. 31–37.

7. **Kalnin T. G., Ivonin D. A., Abrosimov K. N., Grachev E. A., Sorokina N. V.** Analysis of tomographic images of the soil pore space structure by integral geometry methods // Eurasian Soil Science. 2021. Vol. 54. No. 9. Pp. 1400–1409.

8. **Ляхов Л. Н., Лапшина М. Г., Рощупкин С. А.** Теорема о носителе для K_γ-преобразования Радона – Киприянова // *Материалы Воронежской зимней математической школы «Современные методы теории функций и смежные проблемы». 28 января – 2 февраля 2019 г. Ч. 2.* Итоги науки и техники. Сер. Соврем. мат. и ее прил. Темат. обз. 2019. Т. 171. С. 118–124.

9. **Темиргалиев Н., Абикенова Ш. К., Ажгалиев Ш. У., Таугынбаева Г. Е.** Преобразование Радона в схеме К(В)П-исследований и теории квази- Монте-Карло // Известия вузов. Математика. 2020. № 3. С. 98–104.

10. **Баев А. В.** Использование преобразования Радона для решения обратной задачи рассеяния в плоской слоистой акустической среде // Журнал вычислительной математики и математической физики. 2018. Т. 58. № 4. С. 550–560.

11. **Симонов Е. Н., Прохоров А. В., Акинцева А. В.** Математическое моделирование реконструкции объемных изображений в рентгеновской компьютерной томографии с применением голографических методов // Вестник Южно-Уральского гос. ун-та. Сер. Математическое моя делирование и программирование. 2019. Т. 12. № 3. С. 102–114.

12. **Derevtsov E. Yu., Volkov Yu. S., Schuster T.** Differential equations and uniqueness theorems for the generalized attenuated ray transforms of tensor fields // Numerical computations: Theory and algorithms. Part II. Sergeyev Ya. D., Kvasov D. E. (Eds.). Lecture Notes in Computer Science, 2020. Vol. 11974. Pp. 97–111.

13. **Светов И. Е.** Метод приближенного обращения для операторов преобразования Радона функций и нормального преобразования Радона векторных и симметричных 2-тензорных полей в R^3 // Сибирские электронные математические известия. 2020. Т. 17. С. 1073–1087.

14. **Polyakova A. P.** Singular value decomposition of a normal Radon transform operator acting on 3D symmetric 2-tensor fields // Siberian Electronic Mathematical Reports. 2021. Vol. 18. No. 2. Pp. 1572–1595.

15. **Anikonov D. S., Prokhorov I. V., Kovtanyuk A. E.** Investigation of scattering and absorbing media by methods of X-ray tomography // Journal of Inverse and Ill-Posed Problems. 1993. Vol. 1. No. 4. Pp. 259–281.

16. **Вайнберг Э. И., Казак И. А., Файнгойз М. Л.** Рентгеновская вычислительная томография по методу обратного проецирования с фильтрацией двойным дифференцированием // Дефектоскопия. 1985. № 2. С. 31–39.

17. **Деревцов Е. Ю., Мальцева С. В., Светов И. Е.** Определение разрывов функции, заданной в области с рефракцией, по ее экспоненциальному лучевому преобразованию // Сибирский журнал индустриальной математики. 2018. Т. 21. № 4. С. 51–74.

THE AUTHORS

ANIKONOV Dmitry S.
Sobolev Institute of Mathematics
4 Acad. Koptyug Ave., Novosibirsk, 630090, Russia
anik@math.nsc.ru
ORCID: 0000-0003-4056-0988

BALAKINA Ekaterina Yu.
Sobolev Institute of Mathematics
4 Acad. Koptyug Ave., Novosibirsk, 630090, Russia
balakina@math.nsc.ru
ORCID: 0000-0002-5696-4525

KONOVALOVA Dina S.
Sobolev Institute of Mathematics
4 Acad. Koptyug Ave., Novosibirsk, 630090, Russia
dsk@math.nsc.ru
ORCID: 0000-0003-1200-4116

СВЕДЕНИЯ ОБ АВТОРАХ

АНИКОНОВ Дмитрий Сергеевич – *доктор физико-математических наук, заведующий лабораторией условно-корректных задач Института математики имени С. Л. Соболева СО РАН.*
630090, Россия, г. Новосибирск, ул. Коптюга, 4
anik@math.nsc.ru
ORCID: 0000-0003-4056-0988

БАЛАКИНА Екатерина Юрьевна – *кандидат физико-математических наук, научный сотрудник лаборатории условно-корректных задач Института математики имени С. Л. Соболева СО РАН.*
630090, Россия, г. Новосибирск, ул. Коптюга, 4
balakina@math.nsc.ru
ORCID: 0000-0002-5696-4525

КОНОВАЛОВА Дина Сергеевна – *кандидат физико-математических наук, старший научный сотрудник лаборатории условно-корректных задач Института математики имени С. Л. Соболева СО РАН.*
630090, Россия, г. Новосибирск, ул. Коптюга, 4
dsk@math.nsc.ru
ORCID: 0000-0003-1200-4116

Received 04.03.2022. Approved after reviewing 16.03.2022. Accepted 16.03.2022.
Статья поступила в редакцию 04.03.2022. Одобрена после рецензирования 16.03.2022. Принята 16.03.2022.

Original article
DOI: https://doi.org/10.18721/JPM.15105

ABNORMAL PARTICLE HEATING IN THE PLASMA DUST STRUCTURES

S. I. Mol'kov ✉, *A. S. Shtykov*

Petrozavodsk State University, Petrozavodsk, Russia

✉ tandem@onego.ru

Abstract: In order to explain the nature of abnormal particle heating in the plasma dust structures (PDS) based on helium-group gases, kinetic characteristics of PDS have been studied experimentally and theoretically. To inject the dust component, a container with particles of dispersed materials of different nature was used. The visualization and monitoring of PDS behavior as well as measuring of plasma parameters were carried out via specially designed hardware and software complex. The rates and temperatures of dust particles depending on the discharge conditions were determined experimentally. An analysis of the obtained results made it possible to reveal the process peculiarities and to put forward the explanation of mechanism of heating and dissipation of particle energy in the ordered and chaotic PDSs.

Keywords: plasma dust structure, abnormal particle heating, free-molecular condition, RMS-bias

Citation: Mol'kov S. I., Shtykov A. S., Abnormal particle heating in the plasma dust structures, St. Petersburg Polytechnical State University Journal. Physics and Mathematics. 15 (1) (2022) 52–61. DOI: https://doi.org/10.18721/JPM.15105

Научная статья
УДК 533.9.01
DOI: https://doi.org/10.18721/JPM.15105

АНОМАЛЬНЫЙ РАЗОГРЕВ ЧАСТИЦ В ПЛАЗМЕННО-ПЫЛЕВЫХ СТРУКТУРАХ

С. И. Мольков ✉, *А. С. Штыков*

Петрозаводский государственный университет, г. Петрозаводск, Россия

✉ tandem@onego.ru

Аннотация. С целью объяснения природы аномального разогрева пылевых частиц в плазменно-пылевых структурах (ППС) на основе инертных газов, в работе исследуются экспериментально и теоретически кинетические характеристики ППС. Для инжектирования пылевого компонента применялся контейнер с частицами полидисперсных материалов разной природы (оксид алюминия и цинк). Визуализация и мониторинг поведения ППС, а также измерение параметров плазмы осуществлялись с помощью специально созданного программно-аппаратного комплекса. Экспериментально определены скорости и температуры различных пылевых частиц в зависимости от условий разряда. Анализ полученных результатов позволил выявить особенности процессов и предложить объяснение механизма разогрева и диссипации энергии частиц в упорядоченной и хаотической ППС.

Ключевые слова: плазменно-пылевая структура, аномальный разогрев, свободномолекулярный режим, среднеквадратичное смещение

Для цитирования: Мольков С. И., Штыков А. С. Аномальный разогрев частиц в плазменно-пылевых структурах // Научно-технические ведомости СПбГПУ. Физико-математические науки. 2022. Т. 15. № 1. С. 52–61. DOI: https://doi.org/10.18721/ JPM.15105

Introduction

Dusty plasma is an example of an open non-equilibrium system where a self-assembly process occurs, with dissipative structures emerging [1]. Massive dust particles in weakly ionized plasma effectively dissipate their kinetic energy due to collisions with neutral atoms at a rate ν_{da}, so they are assumed to be in equilibrium with the atomic component and their temperature T_d is equal to the atom temperature T_a (T_a = 300 K = 0.026 eV). The mean particle velocity v_d reaches about 0.5 mm/s at a mass $m \approx 0.1$ μg in real experiments. At the same time, the kinetic energy of the dust component particle is about 10 aJ (10^{-17}J), which corresponds to a temperature of the order of 10^3 T_a. The mechanisms behind abnormal heating of the dust component have been linked to stochastic fluctuations in the particle charge [2, 3]. Estimates of T_d values obtained by the formulas given in monograph [4] do not correspond to our experimental data (see the results below), so the true nature of dust particle heating in plasma-dust structures (PDS) is yet to be established definitively.

The goal of this study consisted in describing the behavior of plasma-dust structures, proposing an explanation for the nature of abnormal heating of dust particles in such structures.

Experimental

A plasma crystal setup, described in our earlier study [5], was used for the experiment. A glass discharge tube with a radius of 1.5 cm where the glow discharge plasma was induced and the PDS was generated was filled with the working gas (helium, neon or argon) under a pressure of 0.15 to 3.0 Torr and at a discharge current of 0.1–3.0 mA. A container with particles of different polydisperse materials was used to inject the dust component:

aluminum oxide Al_2O_3 with mean radius $a \approx 23$ μm and mass $m \approx 0.20$ μg;

polydisperse zinc Zn with mean radius $a \approx 28$ μm and $m \approx 0.65$ μg;

same material (Zn), but with $a \approx 8$ μm and $m \approx 0.015$ μg.

The dust structure was visualized with a DTL-316 pulsed semiconductor laser (working wavelength λ = 532 nm) and a set of lenses producing a laser sheet; the PDS can be observed in the light scattered by this sheet.

The hardware and software system for video images included a Hispec 1 high-speed video camera and the Hispec Control software; the system provided real-time recording for 1 min at different speeds (from 25 to 1500 fps). The experimental setup was assembled so that the electrical characteristics of plasma and the pressure of the plasma-forming gas could be monitored simultaneously. The plasma parameters (electron temperature, charge carrier density) were measured by an automated system for recording the probe characteristics.

Fig. 1 shows the trajectories of zinc particles for discharge in neon under a pressure p = 1 Torr, at a discharge current I = 1.5 mA and at different camera speeds.

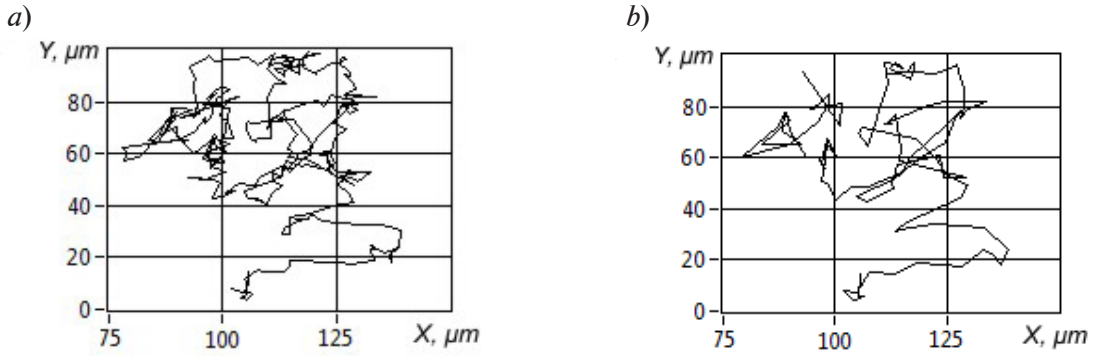

Fig. 1. Trajectories of zinc dust particles in neon, obtained at two camera speeds, fps: 1500 (*a*) and 250 (*b*); pressure p = 1 Torr, discharge current I = 1.5 mA

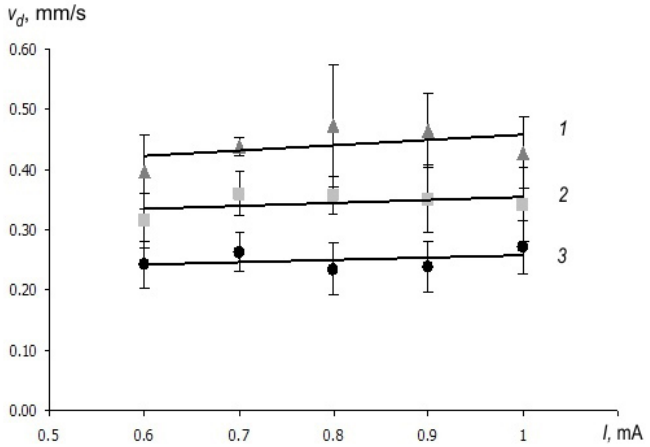

Fig. 2. Experimental dependences of mean velocity on the discharge current for Al_2O_3 particles in neon at various neon pressures p, Torr: 0.3 (*1*), 0.6 (*2*) and 0.9 (*3*)

Particle velocity is determined by the ratio of the distance between two positions of the particle to the time interval equal to the inverse frame rate n of video recording. The error in determining the velocity first decreases with increasing frame rate n, and then starts to increase as the distance traveled by the particle between the frames becomes comparable to its size. The optimal range of the high-speed camera's frame rates was determined experimentally and amounted to 250–500 fps [5]; this was based on the results of particle velocity measurements for PDS in the 'liquid' phase including particles levitating in argon, neon or helium plasma. The confidence interval for the mean velocity v_d, determined through a series of measurements, amounted to 90%.

Fig. 2 shows the typical dependences of the mean velocity on the discharge current for aluminum oxide particles in neon at different pressures.

Analysis of the experimental data obtained for the mean particle velocity v_d and the velocity-related temperature $T_d = m_d v_d^2/3k$ (k is the Boltzmann constant) shows that they weakly depend on current and are governed by pressure. In addition to the particle velocity measurements, experiments were conducted to find the distances r_d between the particles depending on the discharge conditions. The following approximate formulas hold true in the given range of discharge conditions:

$$v_d \approx v_0\sqrt{\frac{p_0}{p}},\ T_d \approx T_0\frac{p_0}{p} = \frac{m_d v_0^2}{3k}\frac{p_0}{p},\ r_d \approx r_0\left(1+\mu I\right)\sqrt{\frac{p}{p_0}}, \quad (1)$$

where v_0, mm/s, is the velocity at $p = p_0 = 0.3$ Torr; T_0, K, is the corresponding temperature; I, mA, is the current.

The quantities v_0, r_0 and the constant μ depend on the type of gas and the characteristics of the particles. For example, they take the following values for PDS in $Ne–Al_2O_3$:

$$v_0 = 0.44 \text{ mm/s},\ T_0 = 9.4\cdot10^5 \text{ K},\ r_0 = 130 \text{ μm},\ \mu = 0.38.$$

The pressure determines the effective electron temperature T_e, and the discharge current determines the electron density n_0. The lighter the plasma-forming gas, the smaller the value of r_d. For example, the following dependence is observed for $p = 0.6$ Torr:

Gas	r_d, μm
Ar	330
Ne	200
He	140

This may be due to the difference in electron temperatures T_e at the same pressures and currents. In particular, the following relationship is observed at $I = 1$ mA, $pR = 0.9$ Torr·cm (R, cm, is the tube radius):

Gas	T_e, eV
Ar	1.4
Ne	2.8
He	3.7

Indeed, according to Eq. (10) (see below), the charge ratio $|Z_d|$ for particles of the same size for different Ar : Ne : He gases is defined as 1.0 : 2.0 : 2.6, which correlates well with the ratio for the inverse distances $(r_d)^{-1}$ between the particles: 1.0 : 1.7 : 2.3.

The distribution of velocity projections along the horizontal axis (Ox) and along the vertical axis (Oy), determined both for an individual dust particle and for their ensemble, corresponds to a normal distribution, which is consistent with the results obtained in [6].

Determination of dust particle velocity and temperature

The distribution function (DF) along the components of dust particle velocity is approximated by a Maxwellian DF [7]:

$$f(\nu_i) = \sqrt{\frac{\beta}{\pi}} \exp\left\{-\beta \nu_i^2\right\}, \tag{2}$$

where $\beta = m_d/2kT_{di}$; T_{di} are the temperatures of dust particles in the vertical ($i = y$) and horizontal ($i = x$) planes; m_d is the mass of dust particles.

Then we obtain the following expression for T_{di} (K):

$$T_{di} = \frac{m_d}{(2\ln 2)k}\left(\frac{\Delta\nu_i}{2}\right)^2,$$

$$\text{or } T_{di}[\text{K}] = 1.3\cdot 10^{16} m_d \Delta v_i^2, \tag{3}$$

where Δv_i is the DF width at half-maximum; m_d is measured in kg, and Δv_i in mm/s.

We analyze the experimental data, for example, for the discharge in argon with Al_2O_3 dust particles with a mass $m_d = 0.2$ μg, for $p = 0.6$ Torr, $I = 0.6$ mA, obtaining that $\Delta v_x = 0.35$ mm/s, $\Delta v_y = 0.53$ mm/s. Calculation by Eq. (2) gives the temperature values along the axes x and y:

$$T_{dx} \approx 3.2\cdot 10^5 \text{ K} \approx 27 \text{ eV}; T_{dy} \approx 7.3\cdot 10^5 \text{ K} \approx 63 \text{ eV}.$$

Thus, the DF of dust particles is anisotropic.

The chaotic velocity of the dust component v_d is related to the temperature of the dust particles as

$$m_d v_d^2/2 = 3T_d/2,$$

where $T_d = (2T_{dx} + T_{dy})/3$.

Then the temperature T_d (K) of the dust particles follows the expression

$$T_d = 2.4\cdot 10^{16} m_d v_d^2, \tag{4}$$

where m_d is expressed in kg, and v_d in mm/s.

Equation of the energy balance and temperature of the dust particles

To establish the mechanism by which dust particles are heated to temperatures at about a few tens of electron volts and are subsequently cooled, we should consider the equation for particle motion:

$$m_d \frac{d\mathbf{u}}{dt} = eZ_d \mathbf{E} - m_d \nu_{da} \mathbf{u} + \mathbf{f}_r, \tag{5}$$

where eZ_d is the charge of the dust particle; **u** is the instantaneous velocity of the particle; ν_{da} is the rate of momentum transfer for collisions between the particle and the atoms; **E** is the local strength of the electric field; $\mathbf{f}_r$ is a random Langevin force due to collisions with atoms, ions and electrons.

The momentum transfer rate ν_{da} given the Knudsen number $\mathrm{Kn} = \lambda_a/a >> 1$ (λ_a is the mean free path of the atom, a is the particle radius) for free molecular flow is expressed as follows [4]:

$$\nu_{da} = \frac{8\sqrt{2\pi}\gamma}{3}\frac{a^2 n_a T_a}{m_d \nu_{T_a}}, \tag{6}$$

or

$$\nu_{da} = 1.16\cdot 10^{-11} a^2 (p/m_d)(m_a/T_a)^{1/2},$$

where a, m, is the dust particle radius; p, Torr, is the pressure, m_d, kg, is the dust particle mass, m_a, u, is the atomic mass in the plasma-forming gas; $v_{T_a} = \sqrt{T_a/m_a}$ is the thermal velocity of atoms; γ is the accommodation coefficient characterizing the collisions between the atoms and the dust particle, $1 < \gamma < 1.39$ ($\gamma = 1.2$ in the calculation formula).

Multiplying Eq. (5) by **u** and averaging it over an ensemble of dust particles within a unit volume, we obtain:

$$n_d \frac{d}{dt}\frac{m_d\langle u^2\rangle}{2} = \langle \mathbf{j}_d\mathbf{E}\rangle - 2\nu_{da} n_d \frac{m_d\langle u^2\rangle}{2} + n_d\langle \mathbf{u}\mathbf{f}_r\rangle, \tag{7}$$

where the last term after averaging is substituted by zero (because there is no correlation between $\mathbf{f}_r$ and **u**); $\mathbf{j}_d$ is the current density of dust particles; **E** is the local strength of the electric field near the particle; n_d is the density of dust particles; $\langle \mathbf{j}_d\mathbf{E}\rangle = W_d$ is the power spectral density generated by the discharge and spent on heating dust particles with the averaging condition imposed not only over the ensemble, but also over time, since the quantities $\mathbf{j}_d$ and **E** fluctuate around the average values.

Bearing in mind that $\langle u^2\rangle = \nu_d^2$, as well as the relationship between the temperature and velocity of dust particles, we obtain an equation for the dust particle temperature:

$$\frac{dT_d}{dt} + 2\nu_{da} T_d = \frac{2W_d}{3n_d k}. \tag{8}$$

Solving this equation with the initial condition $T_d = T_a$, we obtain a time dependence (t is the time) for the dust particle temperature:

$$T_d = T_a \exp\{-2\nu_{da} t\} + \frac{W_d}{3n_d\nu_{da}k}\left(1 - \exp\{-2\nu_{da} t\}\right). \tag{9}$$

The dust component is heated in a characteristic time $\tau \approx (2\nu_{da})^{-1}$ to the temperature determined by the multiplier $W_d/3n_d\nu_{da}k$. In view of expression (1), the dependence of W_d on pressure takes the form $W_d \sim 1/p^{3/2}$, which approximately corresponds to the experimental data (see Table). The quantity W_d can be estimated from the values of experimentally measured temperatures. In our case, it depends on the pressure and current, amounting to about $W_d \sim 10^{-11}$ W/cm^3, which is significantly less than the power density dissipated in the discharge (10^{-5} W/cm^3). The source of dust particle heating $W_d = \langle \mathbf{j}_d\mathbf{E}\rangle$ is related to their temperature T_d by the ratio $W_d/3n_d\nu_{da}kT_d$. Energy dissipation of dust particles occurs upon braking due to collision with gas atoms.

Table shows the experimental and calculated data we obtained for the Ne–Al_2O_3 PDS under various pressures at the discharge current $I = 0.6$ mA. The given characteristics of the PDS are necessary to substantiate the conclusions formulated. The particle charge, measured in elementary charges, is determined by the balance of ion and electron fluxes in plasma, taking into account the emission processes on the surface [8]:

$$|Z_d| = \frac{4\pi\varepsilon_0 a}{e^2} T_e \eta_W(\tau_e) = 694 a T_e \eta_W(\tau_e), \quad (10)$$

where τ_e is the normalized electron temperature ($\tau_e = T_e/T_a$); η_W is the dimensionless potential of the particle depending on τ_e; the quantity a is expressed in μm, T_e in eV. As the temperature T_e increases, the potential η_W decreases, so that $\eta_W T_e \approx$ const [9].

The value of Z_d, calculated taking into account the uncertainty in the properties of the particle surface (degree of roughness, types of emission), yields $|Z_d| = (3 \pm 0.6)10^4$ (in elementary charge units).

We describe the PDS using the nonideality parameter of the system, equal to the ratio of the electrostatic interaction energy between particles to their kinetic energy, i.e., $\Gamma = (eZ_d)^2/r_d T_d$. If $p = 0.3$ Torr, we obtain a value of $\Gamma \approx 100$; melting of the lower PDS section is observed visually in this case. The critical parameter of nonideality Γ_c, corresponding to the phase equilibrium at $r_d/\lambda_D \approx 1$, equals $\Gamma_c = 106$ [1] (λ_D is the Debye shielding radius). If $\Gamma < \Gamma_c$, the plasma-dust system is a liquid; as the pressure increases, the melting stops, and the magnitude of Γ exceeds Γ_c (see the corresponding row in Table), while the PDS is formed as a crystal (in our case, this is a phase with a body-centered cubic lattice (*bcc*)).

Table

Experimental and calculated characteristics of the Ne–Al_2O_3 plasma-dust structure

Parameter	Value for pressure p, Torr			Calculation formula (or experiment)
	0.3	0.6	0.9	
T_e, eV	3.4	2.8	2.5	Experiment/calculation (see [10])
v_d, mm/s	0.44	0.35	0.25	Experiment
T_d, 10^3 K	940	590	300	$T_d = 3m_d v_d^2/k$
	270	193	155	Calculation (see [4])
r_d, μm	160	225	280	Experiment
n_d, 10^5cm^{-3}	2.44	0.88	0.46	$n_d = 10^{12}/r_d^3$
Γ	≈ 100	≈ 120	≈ 180	$\Gamma = (eZ_d)^2/r_d T_d$ (for estimate)
W_d, 10^{-11} W·cm^{-3}	2.28	1.03	0.41	$W_d = 3n_d \nu_{da} k T_d$
r_c, μm	22.0	17.5	12.5	$r_c = \sqrt{3kT_d/\alpha}$
E_d, W/cm	3.67	2.92	2.09	$E_d = \alpha r_c/e\|Z_d\|$
j_d, 10^{-11} A·cm^{-2}	0.62	0.35	0.196	$j_d = W_d/E_d$
r_c/r_d	0.14	0.08	0.045	Lindemann criterion

Notations: T_e, T_d are the effective electron temperature and dust particle (DP) temperature, respectively; v_d, r_d are the mean DP velocity and the distance between the particles; n_d is the DP density; r_c is the mean-squared displacement of DP from the equilibrium position in a conditional crystal lattice; Γ is the nonideality parameter of the system; W_d is the power density released in the discharge and spent on heating dust particles; E_d is the mean strength of the electric field; j_d is DP current density; m_d, eZ_d are the DP mass and charge; ν_{da} is the rate of DP collisions with neutral atoms; α is the elasticity coefficient; k is the Boltzmann constant.

Note. The discharge current is $I = 0.6$ mA for all data.

Table lists, among other parameters, the values of T_d, which we found by calculation using the formulas given in [4]; they are considerably different from our results (given in the row above). Thus, the power of the DP heating source associated with the fluctuation of particle charge induced by the discrete charging current [4], is clearly insufficient for the observed heating of particles.

Consider the quantity $W_d = \langle \mathbf{j}_d \mathbf{E} \rangle$. The current density of dust particles j_d is induced by elementary currents $eZ_d \nu_d / r_d$ near the sites of the crystal lattice. Averaging within a unit volume, we obtain an estimate of the maximum characteristic density of dust particle current: $j_d^{\max} \sim eZ_d n_d \nu_d$. The minimum field strength corresponding to W_d is equal to $E^{\min}_d \sim W_d / j_d^{\max}$.

A more accurate value of the field strength near the lattice site can be estimated using the electrostatic oscillation frequency ω_E. For particles of different materials and sizes in the neon discharge for $\omega_E \sim 1/\sqrt{m_d}$, ~10–80 s^{-1}, and then the coefficient of elasticity is equal to $\alpha = \omega_E^2 m_d \sim (8 \pm 2) 10^{-8}$ kg/s^2. The elastic force acting on the particle allows to estimate the field strength by the formula $E_r = \alpha r / e|Z_d|$, where r is the radial coordinate.

The potential φ at the distance r from the particle is determined by the expression:

$$\varphi = -\int E_r dr = \alpha r^2 / 2e|Z_d|.$$

Assuming the thermodynamic equilibrium of the dust component and using the theorem on the uniform distribution of kinetic energy over degrees of freedom, we obtain:

$$e|Z_d|\langle \varphi \rangle = \alpha \langle r^2 \rangle / 2 = 3kT_d / 2,$$

$$r_c = \sqrt{\langle r^2 \rangle} = \sqrt{3kT_d / \alpha}. \qquad (11)$$

For example, if $T_d = 9.4 \cdot 10^5$ K, we obtain $r_c = 22$ μm, which corresponds to the observed deviations of particles from the equilibrium position (see Fig. 1). The physical meaning of the quantity r_c becomes clear from expression (11): this is the mean-squared displacement of a particle from the equilibrium position in a conditional crystal lattice. Table gives the values of r_c and the corresponding averaged values of $E_d = \alpha r_c / e|Z_d|$ and $j_d = W_d / E_d$, providing the required value W_d. According to the Lindemann criterion for a melting crystal [4], $r_c / r_d \geq 0.15$, which is close to our results: $r_c / r_d = 0.14$.

Thus, the heating source of dust particles is only partially related to their charge fluctuation induced by discrete charging current [2]. This dust particle in lattice site loses the equilibrium position due to the random collisions with gas atoms and because of the force action of the nearest dust particles in constant Brownian motion. The potential energy upon displacement from the lattice site increases by an average of $\alpha r_c^2 / 2$, which is converted into kinetic energy of directed motion $3kT_d / 2$.

Conclusion

We have considered the kinetic characteristics of plasma-dust structures (PDS) both experimentally, using high-speed video recording, and theoretically. We determined the velocities and temperatures of dust particles depending on the discharge conditions. Good agreement between theoretical and experimental results was obtained. We have proposed a scenario for the mechanism behind heating and dissipation of particle energy in ordered and chaotic plasma-dust structures.

REFERENCES

1. **Fortov V. E., Khrapak A. G., Khrapak S. A., et al.,** Dusty plasmas, Physics-Uspekhi. 47 (5) (2004) 447–492.

2. **Morfill G. E., Thomas H.,** Plasma crystal, J. Vacuum Sci. & Technol. A. 14 (2) (1996) 490–495.

3. **Vaulina O. S., Nefedov A. P., Petrov O. F., Khrapak S. A.,** Role of stochastic fluctuations in the charge on macroscopic particles in dusty plasmas, JETP. 88 (6) (1999) 1130–1136.

4. **Vaulina O. S., Petrov O. F., Fortov V. E., et al.,** Pylevaya plazma: eksperiment i teoriya [Dusty plasmas: Experiment and theory], Fizmatlit, Moscow, 2009 (in Russian).

5. **Shtykov A. S.,** The measuring of the kinetic characteristics values of dusty plasma using the high-speed video camera, Proceedings of Petrozavodsk State University. Natural & Engineering Sciences. (6 (151)) (2015) 121–123 (in Russian).

6. **Zharikov N. E., Piskunov A. A., Podryadchikov S. F., et al.,** Dusty structure and microparticle properties modification in complex plasma, Proceedings of Petrozavodsk State University. Natural & Engineering Sciences. (6 (111)) (2010) 99–108 (in Russian).

7. **Biberman, L. M., Vorob'ev V. S., Yakubov I. T.,** Kinetika neravnovesnoy nizkotemperaturnoy plazmy [Kinetics of nonequilibrium low temperature plasma], Nauka, Moscow, 1982 (in Russian).

8. **Mol'kov S. I., Savin V. N.,** Mechanisms of dust grain charging in plasma with allowance for electron emission processes, Plasma Physics Reports. 43 (2) (2017) 202–212.

9. **Savin V. N., Mol'kov S. I.,** The effect of electron emission processes on micro- and nanoparticle charges in the dusty plasma: the accounting for engineering, St. Petersburg State Polytechnical University Journal. Physics and Mathematics. (3(248)) (2016) 78–87 (in Russian).

10. **Prokhorova E. I., Platonov A. A., Molkov S. I., et al.,** The effect of material and roughness of the probe surface on probe characteristics, Plasma Physics Reports. 46 (5) (2020) 521–526.

СПИСОК ЛИТЕРАТУРЫ

1. **Фортов В. Е., Храпак А. Г., Храпак С. А., Молотков В. И., Петров О. Ф.** Пылевая плазма // Успехи физических наук. 2004. Т. 174. № 5. С. 494–544.

2. **Morfill G. E., Thomas H.** Plasma crystal // Journal of Vacuum Science & Technology. A. 1996. Vol. 14. No. 2. Pp. 490–495.

3. **Ваулина О. С., Нефедов А. П., Петров О. Ф., Храпак С. А.** Роль стохастических флуктуаций заряда макрочастиц в пылевой плазме // Журнал экспериментальной и теоретической физики. 1999. Т. 115. № 6. С. 2067–2079.

4. **Ваулина О. С., Петров О. Ф., Фортов В. Е., Храпак А. Г., Храпак С. А.** Пылевая плазма: эксперимент и теория. М.: Физматлит, 2009, 315 с.

5. **Штыков А. С.** Измерение значений кинетических характеристик плазменно-пылевых систем с помощью высокоскоростной видеосъемки // Ученые записки Петрозаводского государственного университета. Серия: Естественные и технические науки. 2015. № 6 (151). С. 121–123.

6. **Жариков Н. Е., Пискунов А. А., Подрядчиков С. Ф., Семенов А. В., Хахаев А. Д., Щербина А. И.** Модификация свойств плазменно-пылевых структур и микрочастиц в комплексной плазме // Ученые записки Петрозаводского государственного университета. Серия: Естественные и технические науки. 2010. № 6 (111). С. 99–108.

7. **Биберман Л. М., Воробьев В. С., Якубов И. Т.** Кинетика неравновесной низкотемпературной плазмы. М.: Наука, 1982, 376 с.

8. **Мольков С. И., Савин В. Н.** Механизмы зарядки пылевых части в плазме с учетом эмиссионных процессов // Физика плазмы. 2017. Т. 43. № 2. С. 193–202.

9. **Савин В. Н., Мольков С. И.** Учет влияния эмиссионных процессов на заряд микро- и наночастиц в пылевой плазме для технологических приложений // Научно-технические ведомости СПбГПУ. Физико-математические науки. 2016. № 3(248) С. 78–87.

10. **Прохорова Е. И., Платонов А. А., Мольков С. И., Игнахин В. С., Назаров А. И.** Влияние материала и степени шероховатости поверхности зонда на зондовые характеристики // Физика плазмы. 2020. Т. 46. № 5. С. 435–440.

THE AUTHORS

MOL'KOV Sergey I.
Petrozavodsk State University
33, Lenin Ave., Petrozavodsk, 185910, Russia
tandem@onego.ru, molkov@petysu.ru
ORCID: 0000-0002-2792-0320

SHTYKOV Aleksey S.
Petrozavodsk State University
33, Lenin Ave., Petrozavodsk, 185910, Russia
shtykoff@petrsu.ru
ORCID: 0000-0003-4693-8881

СВЕДЕНИЯ ОБ АВТОРАХ

МОЛЬКОВ Сергей Иванович – *доктор физико-математических наук, профессор кафедры электроники и электроэнергетики Петрозаводского государственного университета.*
185910, Россия, г. Петрозаводск, пр. Ленина, 33.
tandem@onego.ru, molkov@petysu.ru
ORCID: 0000-0002-2792-0320

ШТЫКОВ Алексей Сергеевич – *старший преподаватель кафедры информационно-измерительных систем и физической электроники Петрозаводского государственного университета.*
185910, Россия, г. Петрозаводск, пр. Ленина, 33.
shtykoff@petrsu.ru
ORCID: 0000-0003-4693-8881

Received 13.12.2021. Approved after reviewing 07.02.2022. Accepted 08.02.2022.
Статья поступила в редакцию 13.12.2021. Одобрена после рецензирования 07.02.2022. Принята 08.02.2022.

Original article
DOI: https://doi.org/10.18721/JPM.15106

SURFACES OF COHESIVE BONDS' FRACTURE IN THE MULTILAYER SYSTEMS: A COMPARATIVE ANALYSIS

N. V. Ilyasowa [1] ✉, *O. V. Kondrakova* [1], *A. I. Kudyukin* [2], *E. N. Moos* [2]

[1] Ryazan State Medical University, Ryazan, Russia;

[2] Ryazan State University named for S. A. Yesenin, Ryazan, Russia

✉ ilyasowa-natalya@mail.ru

Abstract: Studies of the fracturing surfaces on foreign material as a model object that binds a component to bone tissue have been carried out. Metal and ceramic brackets were used during operation. Brackets were fixed using the same materials under the identical conditions, according to the standard direct fixing procedure. Areas of the bone surfaces were investigated (when brackets removed) with the aid of scanning atomic force microscopy (AFM). The studied roughness was digitized owing to the 'analysis' microscope option. As a result, the average value of the fracture surface roughness was found (when removed) to be 241 nm for the metal bracket systems and 156 nm for the ceramic ones. Ultimately, the difference was more than one and a half. This is useful in practical medicine when choosing a bracket system.

Keywords: bracket system, bone tissue, discontinuity surface, atomic force microscopy, surface profiling

Citation: Ilyasowa N. V., Kondrakova O. V., Kudyukin A. I., Moos E. N., Surfaces of cohesive bonds' fracture in the multilayer systems: A comparative analysis, St. Petersburg Polytechnical State University Journal. Physics and Mathematics. 15 (1) (2022) 62–69. DOI: https://doi.org/10.18721/JPM.15106

Научная статья
УДК 620.22
DOI: https://doi.org/10.18721/JPM.15106

СРАВНИТЕЛЬНЫЙ АНАЛИЗ ПОВЕРХНОСТЕЙ РАЗРЫВА КОГЕЗИОННЫХ СВЯЗЕЙ В МНОГОСЛОЙНЫХ СИСТЕМАХ

Н. В. Илясова [1] ✉, *О. В. Кондракова* [1], *А. И. Кудюкин* [2], *Е. Н. Моос* [2]

[1] Рязанский государственный медицинский университет имени академика И. П. Павлова, г. Рязань, Россия;

[2] Рязанский государственный университет имени С. А. Есенина, г. Рязань, Россия

✉ ilyasowa-natalya@mail.ru

Аннотация. Проведены исследования поверхности разрыва на модельном объекте – инородном материале, который связывает компонент с костной тканью. В процессе работы использованы металлические и керамические брекеты. Фиксирование брекетов проведено в идентичных условиях с использованием одинаковых материалов по стандартному прямому методу фиксации. Участки поверхности костной ткани исследовали при снятии брекета, с помощью метода атомно-силовой микроскопии (АСМ). Благодаря применению опции «анализ», имеющейся у сканирующего зондового микроскопа, шероховатость исследуемых поверхностей была переведена в цифровую характеристику. Установлено, что среднее значение шероховатости поверхности разрыва (при снятии) для металлической брекет-системы составило 241 нм, а для керамической – 156 нм, что указывает на более чем полуторократное различие. Полученный результат может быть полезен в практической медицине при выборе брекет-системы.

Ключевые слова: брекет, костная ткань, поверхность разрыва, атомно-силовая микроскопия, поверхностное профилирование, растровое изображение

Для цитирования: Илясова Н. В., Кондракова О. В., Кудюкин А. И., Моос Е. Н. Сравнительный анализ поверхностей разрыва когезионных связей в многослойных системах // Научно-технические ведомости СПбГПУ. Физико-математические науки. 2022. Т. 15. № 1. С. 62–69. DOI: https://doi.org/10.18721/ JPM.15106

Introduction

Physical materials science has been central to the advances made in the medical industry. There is a known problem with compatibility between living tissues and foreign materials, for example, in the case of bone and joint replacement [1–7] or mounting of bracket systems. This aspect is important for multilayer structures comprising bone tissue, binder, and metal or ceramics. A wide range of orthodontic appliances are available; in particular, both removable and fixed appliances are used for bite correction and teeth alignment [8–11]. Edgewise brackets are a type of fixed appliance popular in the orthodontics market. Removing these brackets carries a risk that tooth enamel can be damaged and subsequently crack. Studying the bond strengths and adhesive remnants underneath orthodontic brackets is of interest for orthodontic practitioners; the remnants can have damaging effects if the patient consumes any chemicals [12].

However, we have been unable to uncover any studies on the topology of the fracture surface, which should serve as an evaluative criterion. This aspect of the problem makes it possible to predict the effectiveness of certain technological approaches.

The goal of this study consists in exploring the characteristics of the fracture surfaces in metal and ceramic brackets.

Experimental samples and procedures

The behavior of the surface fractures was analyzed for two bracket systems manufactured by 3M Unitek (USA): metal Victory Series™ and ceramic Clarity™. We prepared a small sample of human tooth specimens, unaffected by caries and extracted for orthodontic (retained, dystopic) or periodontal reasons.

The specimens were prepared as follows. The surfaces of all teeth were rinsed under running water, cleaned of plaque with circular brushes and polishing paste (Detartrine, Septodont). The specimens prepared were stored in normal saline (0.9% sodium chloride solution) prior to the study. Brackets were attached in accordance with the standard protocol. The dental specimens were etched with 37% orthophosphoric acid gel (TRAVEX-37, Omega) for 30 s. The treated area was then sprayed with large amounts of water to remove the gel, and dried until the enamel reached a semi-dry chalky state.

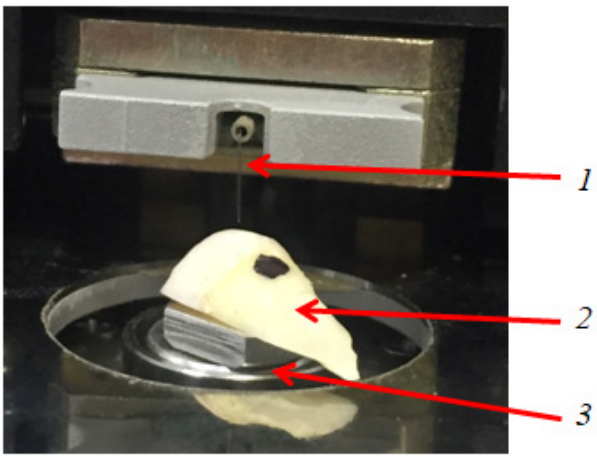

Fig. 1. Tooth specimen (*2*) mounted on stage (*3*) of the scanner and cantilever (*1*) of the scanning probe microscope

The TRANSBOND XT (3M Unitek) primer was applied to the enamel and the bracket base. The primer was cured with a LED lamp emitting at 400–500 nm (UV range) for 40 s. A TRANSBOND XT (3M Unitek) light-curing adhesive was then applied to the bracket base, excess material was removed, and the bracket was attached to the surface of the tooth. Next, first the mesial and then the distal surface of the bracket was light-cured (for 10 s in both cases). Both brackets (metal and ceramic) were simultaneously attached to one tooth. The system was removed after 7 days using specialized atraumatic forceps. Atomic force microscopy (AFM) was then used to analyze sections of the surface in each tooth. Fig. 1 shows tooth specimen *2* mounted on stage *3*. As cantilever *1* moves along the fracture surface considered, its profile is recorded, with a raster image generated.

The scanning probe microscope has a function for analysis, allowing to extract the numerical values for the measured roughness of the given surface.

Results and discussion

The results of the above measurement procedure are shown in Fig. 2–4. After scanning the fracture surfaces in the binding system of the multilayer structure (dental enamel – adhesive system – bracket), we carried out comparative analysis of the scans along two orthogonal directions. All figures below show the scan lines of the cantilever along which roughness was measured.

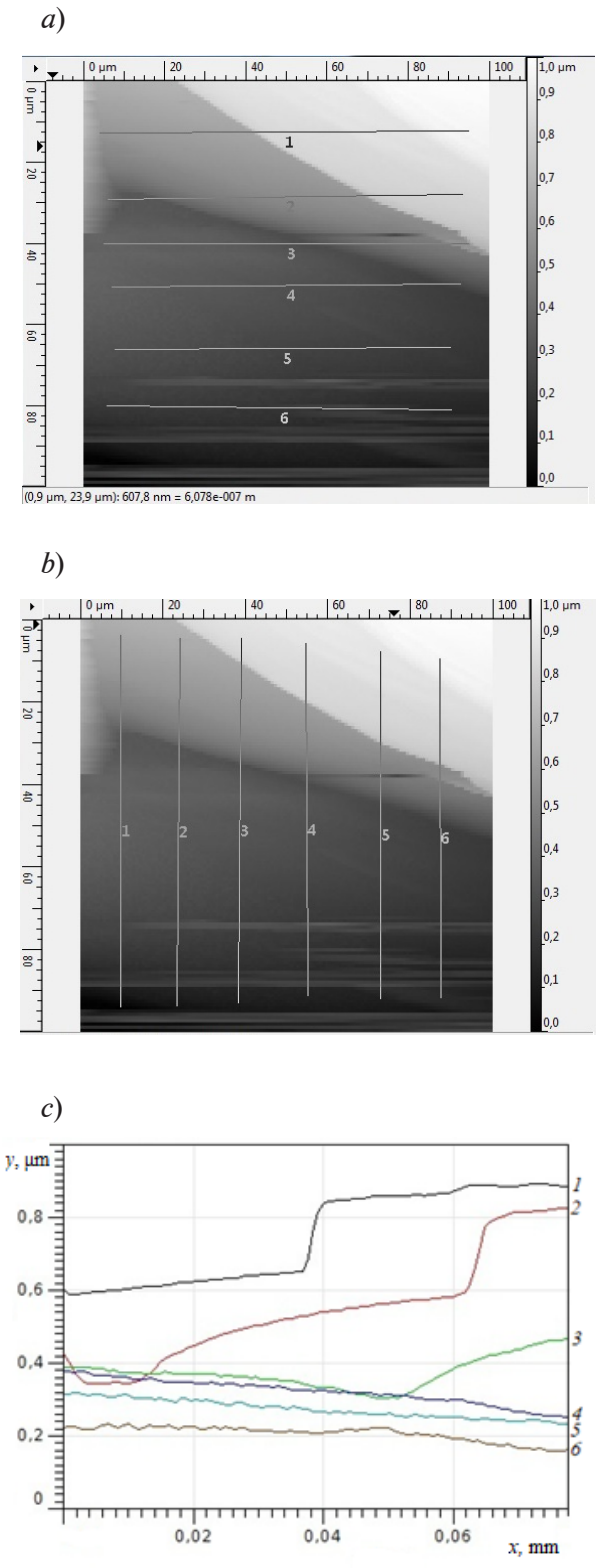

Fig. 2. Dependences of relief height on the scanning coordinate along two orthogonal directions (*a*, *b*) and the scanned surface curves after the ceramic bracket was removed (*c*)

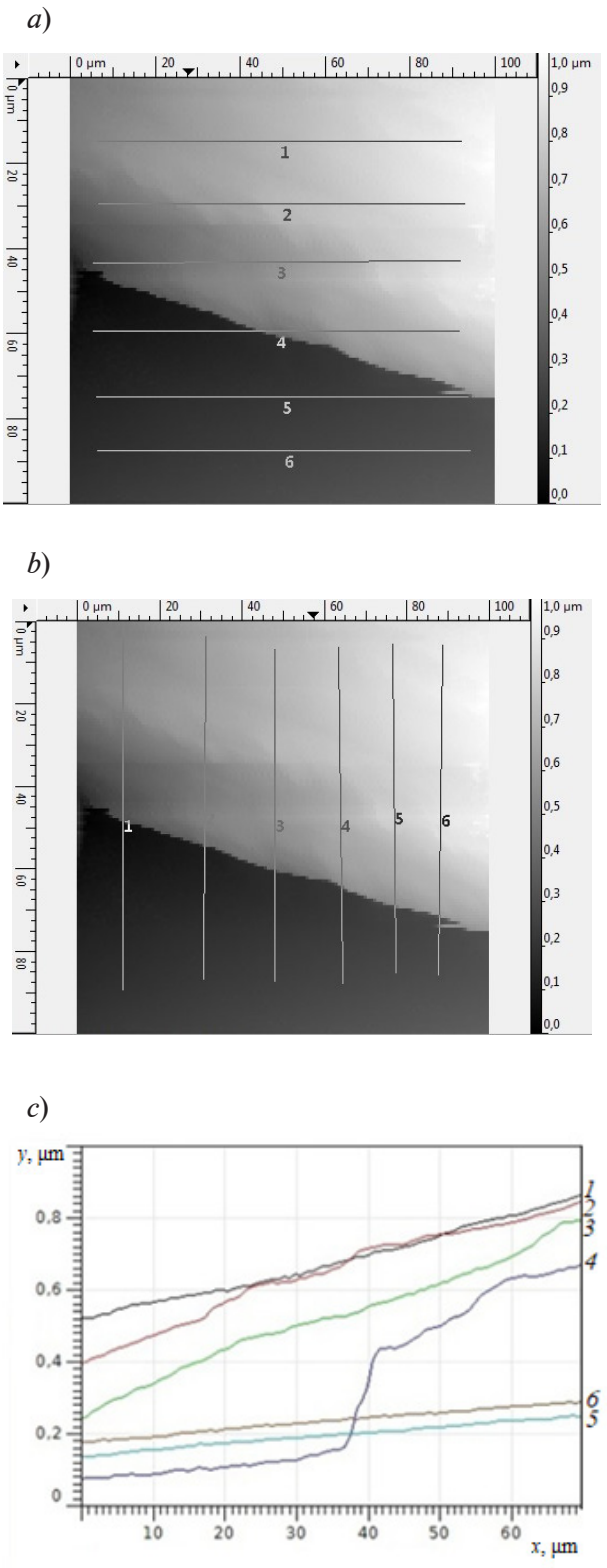

Fig. 2. Dependences of relief height on the scanning coordinate along two orthogonal directions (*a*, *b*) and the scanned surface curves after the metal bracket was removed (*c*)

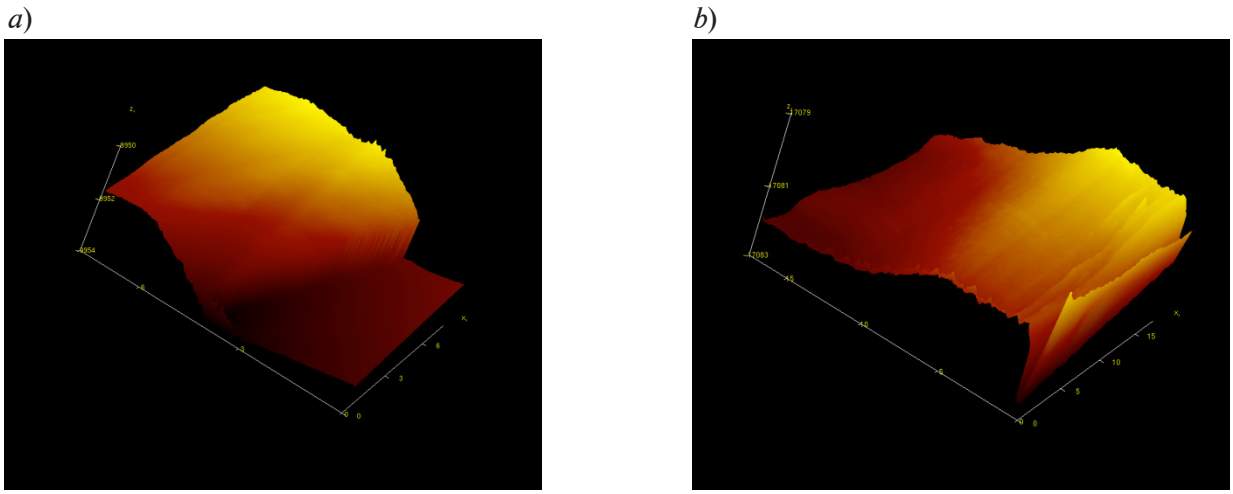

Fig. 4. 3D raster images of surfaces obtained after removal of metal (*a*) and ceramic (*b*) brackets

Table

Measurement results for average roughness of the fracture surface for removal of two types of brackets

Sample number	Average surface roughness, nm	
	Metal bracket	Ceramic bracket
1	253.6	212.0
2	232.8	155.8
3	255.7	140.0
4	391.6	74.79
5	180.5	138.2
6	228.9	190.9
7	180.4	143.4

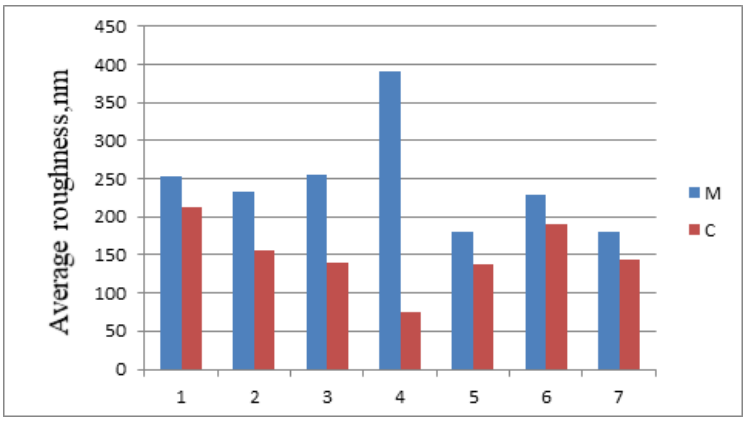

Fig. 5. Diagram for average roughnesses of dental surfaces after removal of metal (M) and ceramic (C) bracket systems. Specimen numbers are plotted on the horizontal axis (see Table)

Scanning was carried out for lines *1*–*6* shown in Figs. 2, *a*, *b* and 3, *a, b*. Height differences of about 200 nm were detected along one profile. In particular, we discovered by scanning along the selected direction of profile *1* that a jump in height y in the range of 0.63–0.84 (Fig. 2, *c*) occurs at the coordinate $x = 0.036$. As seen in Fig. 3, *c*, scanning along profile *4*, we observed a jump in height y in the range of 0.16–0.43 at the coordinate $x = 0.037$.

Furthermore, Fig. 4, *a*,*b* shows the surface reliefs (in Cartesian coordinates) obtained after removing metal (4,*a*) and ceramic (4,*b*) brackets.

Table shows the average roughnesses of the fracture surface for metal and ceramic brackets. Fig. 5 shows a diagram for the average roughness of the tooth surface, revealing significant variations in this characteristic. We observed irregularities (peaks and valleys) from 575.8 to −836.0 nm.

Comparative analysis of the results given in Table indicates that the average roughnesses of fracture surfaces in tooth enamel lie in the range from 180.4 to 212.0 nm for ceramic brackets and from 143.4 to 253.6 nm for metal ones. The integral result for the average roughness of the fracture surface amounts to an even greater difference: in the range from 74.79–212.0 nm for ceramic and 143.4–391.6 nm for metal. Given the same material and attachment method, removing the metal bracket system yields a roughness whose values exceed those for the ceramic system by more than 1.5 times. Expressed numerically, the degree to which the roughness is developed reflects the strength of the adhesion process in three-layer composites.

Conclusion

The difference in the structures and materials used, the sequence of steps and methods for attaching the brackets at both the preparatory and main stages of the procedure has allowed to formulate the proposals for improving the technologies adopted in dental practice. The findings outlined in this paper can be useful in practical medicine for choosing the bracket system.

REFERENCES

1. **Sinani I. L., Shchurik A. G., Osorgin Yu. K., Bushuev V. M.,** Carbon-carbon composites for orthopaedics and traumatology, Russian Journal of Biomechanics. 16 (2(56)) (2012) 66–73. (in Russian).

2. **Gavryushenko N. S., Batrakov S. Yu., Balametov S. G.,** Comparative characteristic of mechanical strength properties of the carbon nanostructural implant and native bone, Vestnik of the Smolensk State Medical Academy. 19 (1) (2020) 108–115 (in Russian).

3. **Fedoseev A. V., Litvinov A. A., Chekushin A. A., et al.,** Quality of life in patients after total cement or cementless hip arthroplasty, I. P. Pavlov Russian Medical Biological Herald. 22 (4) (2014) 121–125 (in Russian).

4. **Shevtsov V., Mushkin A., Sergeyev K., et al.,** Uglerod: novyye grani yego ispolzovaniya v meditsine [Carbon: New facets of its use in medicine], Meditsinskaya gazeta [Medical Newspaper]. 2014. No. 86, November 19, 2014 (in Russian).

5. **Nazarov E. A., Ryabova M. N.,** Application domestic implants in total hip arthroplasty, I. P. Pavlov Russian Medical Biological Herald. 15 (2) (2007) 13–20 (in Russian).

6. **Kuzmanin S. A., Nazarov E. A., Vesnov I. G.,** Composite material based on calcium phosphate and germanium (experimental study), I. P. Pavlov Russian Medical Biological Herald. 24 (2) (2016) 92–100 (in Russian).

7. **Ryabova M. N., Nazarov E. A., Zubov A. A., Podyablonskaya I. A.,** Total hip replacement in bilateral ankyloses, Nauka molodykh (Eruditio Juvenium). (2) (2017) 271–276.

8. **Chetan P., Tandon P., Singh G., et al.,** Dynamics of a smile in different age groups, Angle Orthod. 83 (1) (2013) 90–96.

9. **Sarver D. M.,** Interactions of hard tissues, soft tissues, and growth over time, and their impact on orthodontic diagnosis and treatment planning, Am. J. Orthod. Dentofacial Orthop. 148 (3) (2015) 380–386.

10. **Pitts T. R.,** Bracket positioning for smile arc protection, J. Clin. Orthod. 51 (3) (2017) 142–156.

11. **Proffit W., Fields H., Larson B., Sarver D.,** Contemporary orthodontics, 6th ed., Elsevier, Philadelphia, 2018.

12. **Pulgaonkar R., Chitra P.,** Stereomicroscopic analysis of microleakage, evaluation of shear bond strengths and adhesive remnants beneath orthodontic brackets under cyclic exposure to commonly consumed commercial «soft» drinks, Indian J. Dent. Res. 32 (1) (2021) 98–103.

СПИСОК ЛИТЕРАТУРЫ

1. **Синани И. Л., Щурик А. Г., Осоргин Ю. К., Бушуев В. М.** Углерод-углеродные материалы для ортопедии и травматологии // Российский журнал биомеханики. 2012. Т. 16. № 2. С. 74–82.

2. **Гаврюшенко Н. С., Батраков С. Ю., Баламетов С. Г.** Сравнительная характеристика механикопрочностных свойств углеродного наноструктурного имплантата и нативной кости // Вестник Смоленской государственной медицинской академии. 2020. Т. 19. № 1. С. 108–115.

3. **Федосеев А. В., Литвинов А. А., Чекушин А. А., Филоненко П. С., Аль Мансур А. Ю., Юрчикова Е. Е.** Качество жизни пациентов после тотального цементного и бесцементного эндопротезирования тазобедренного сустава // Российский медико-биологический вестник имени академика И. П. Павлова. 2014. Т. 22. № 4. С. 121–125.

4. **Шевцов В., Мушкин А., Сергеев К., Скрябин В., Шатохин В., Эргашев О.** Углерод: новые грани его использования в медицине // Медицинская газета. № 86 от 19 ноября 2014. С. 7–10.

5. **Назаров Е. А., Рябова М. Н.** Применение отечественных имплантатов в эндопротезировании тазобедренного сустава // Российский медико-биологический вестник имени академика И. П. Павлова. 2007. Т. 15. № 2. С. 13–20.

6. **Кузьманин С. А., Назаров Е. А., Веснов И. Г.** Экспериментальное исследование сил сцепления композиционного материала из фосфата кальция и германия с костью // Российский медико-биологический вестник имени академика И. П. Павлова. 2016. Т. 24. № 2. С. 92–100.

7. **Рябова М. Н., Назаров Е. А., Зубов А. А., Подъяблонская И. А.** Тотальное эндопротезирование тазобедренного сустава при двухстороннем анкилозе // Наука молодых (Eruditio Juvenium). 2017. № 2. С. 265–270.

8. **Chetan P., Tandon P., Singh G. K., Nagar A., Prasad V., Chugh V. K.** Dynamics of a smile in different age groups // The Angle Orthodontist. 2013. Vol. 83. No. 1. Pp. 90–96.

9. **Sarver D. M.** Interactions of hard tissues, soft tissues, and growth over time, and their impact on orthodontic diagnosis and treatment planning. // American Journal of Orthodontics & Dentofacial Orthopedics. 2015. Vol. 148. No. 3. Pp. 380–386.

10. **Pitts T. R.** Bracket positioning for smile arc protection // Journal of Clinical Orthodontics. 2017. Vol. 51. No. 3. Pp. 142–156.

11. **Proffit W., Fields H., Larson B., Sarver D.** Contemporary orthodontics. 6th ed. Philadelphia, USA: Elsevier, 2018. 160 p.

12. **Pulgaonkar R., Chitra P.** Stereomicroscopic analysis of microleakage, evaluation of shear bond strengths and adhesive remnants beneath orthodontic brackets under cyclic exposure to commonly consumed commercial “soft” drinks // Indian Journal of Dental Research. 2021. Vol. 32. No. 1. Pp. 98–103.

THE AUTHORS

ILYASOWA Natalya V.
Ryazan State Medical University
9, Vysokovol’tnaya St., Ryazan, 390026, Russia
ilyasowa-natalya@mail.ru
ORCID: 0000-0001-8248-4309

KONDRAKOVA Olga V.
Ryazan State Medical University
9, Vysokovol’tnaya St., Ryazan, 390026, Russia
kov0177@mail.ru
ORCID: 0000-0002-4889-5566

KUDYUKIN Aleksandr I.
Ryazan State University named for S. A. Yesenin
40, Svobody St., Ryazan, 390000, Russia
a.kudykin@rsu.edu.ru
ORCID: 0000-0002-1213-4837

MOOS Evgeniy N.
Ryazan State University named for S. A. Yesenin
40, Svobody St., Ryazan, 390000, Russia
e_moos@mail.ru
ORCID: 0000-0003-3831-7882

СВЕДЕНИЯ ОБ АВТОРАХ

ИЛЯСОВА Наталья Викторовна – *ординатор кафедры ортопедической стоматологии и ортодонтии Рязанского государственного медицинского университета имени академика И. П. Павлова.*
390026, г. Рязань, Высоковольтная ул., 9
ilyasowa-natalya@mail.ru
ORCID: 0000-0001-8248-4309

КОНДРАКОВА Ольга Владимировна – *кандидат медицинских наук, доцент кафедры ортопедической стоматологии и ортодонтии, врач-ортодонт Рязанского государственного медицинского университета имени академика И. П. Павлова.*
390026, г. Рязань, Высоковольтная ул., 9
kov0177@mail.ru
ORCID: 0000-0002-4889-5566

КУДЮКИН Александр Игоревич – *аспирант кафедры общей и теоретической физики и методики преподавания физики Рязанского государственного университета имени С. А. Есенина.*
390000, Россия, г. Рязань, ул. Свободы, 46
a.kudykin@rsu.edu.ru
ORCID: 0000-0002-1213-4837

МООС Евгений Николаевич – *доктор технических. наук, профессор кафедры общей и теоретической физики и методики преподавания физики Рязанского государственного университета имени С. А. Есенина.*
390000, Россия, г. Рязань, ул. Свободы, 46
e_moos@mail.ru
ORCID: 0000-0003-3831-7882

Received 14.11.2021. Approved after reviewing 15.12.2021. Accepted 15.12.2021.
Статья поступила в редакцию 14.11.2021. Одобрена после рецензирования 15.12.2021. Принята 15.12.2021.

Original article
DOI: https://doi.org/10.18721/JPM.15107

SINGLE MOLECULES CHARACTERIZATION OF TRANSCRIPTION OF BACTERIAL RNA-POLYMERASE PARAMETERS USING ACOUSTIC FORCE SPECTROSCOPY

A. N. Arseniev, M. A. Panfilov, G. E. Pobegalov, A. S. Potyseva, P. A. Pavlinova, M. V. Yakunina, M. A. Khodorkovskii ✉

Peter the Great St. Petersburg Polytechnic University, St. Petersburg, Russia

✉ khodorkovskii@gmail.com

Abstract: This work presents the results of single-molecule studies of the effect of magnesium ions on the dynamic characteristics of transcription elongation of bacterial RNA polymerase. It has been shown that the instant and average transcription velocities decrease with a decrease in magnesium concentration. The observed dependence occurred due to an increase in the number of short pauses; an explanation of the mechanism of their formation was put forward. To perform these studies, the method of acoustic force spectroscopy (AFS) was used. This technique served as a basis for the development of a single-molecule procedure for characterizing the transcription parameters. A detailed description of the method and algorithm for processing the measurement results was given.

Keywords: transcription, RNA polymerase, acoustic force spectroscopy, single-molecule methods

Funding: The research was supported by the Ministry of Education of Russian Federation as a part of a state task (agreement No. 075-15-2021-996, Sept. 23, 2021).

Citation: Arseniev A. N., Panfilov M. A., Pobegalov G. E., Potyseva A. S., Pavlinova P. A., Yakunina M. V., Khodorkovskii M. A., Single molecules characterization of transcription of bacterial RNA-polymerase parameters using acoustic force spectroscopy, St. Petersburg Polytechnical State University Journal. Physics and Mathematics. 15 (1) (2022) 70–80. DOI: https://doi.org/10.18721/JPM.15107

Научная статья
УДК 577.29, 57,052, 57,042.2
DOI: https://doi.org/10.18721/JPM.15107

ХАРАКТЕРИЗАЦИЯ НА УРОВНЕ ОДИНОЧНЫХ МОЛЕКУЛ ПАРАМЕТРОВ ТРАНСКРИПЦИИ БАКТЕРИАЛЬНОЙ РНК-ПОЛИМЕРАЗЫ МЕТОДОМ АКУСТИЧЕСКОЙ СИЛОВОЙ СПЕКТРОСКОПИИ

А. Н. Арсениев, М. А. Панфилов, Г. Е. Побегалов, А. С. Потысьева, П. А. Павлинова, М. В. Якунина, М. А. Ходорковский ✉

Санкт-Петербургский политехнический университет Петра Великого, Санкт-Петербург, Россия

✉ khodorkovskii@gmail.com

Аннотация. В настоящей работе приведены результаты одномолекулярных исследований влияния ионов магния на динамические характеристики элонгации транскрипции бактериальной РНК-полимеразы. Показано, что с уменьшением концентрации магния снижаются мгновенная и средняя скорости транскрипции. Наблюдаемая зависимость происходит за счет увеличения количества коротких пауз; предложено объяснение механизма их образования. Для проведения исследований использован метод акустической силовой спектроскопии (АСС), который составил основу для разработки одномолекулярной методики характеризации параметров транскрипции. Приведено подробное описание методики и алгоритма обработки результатов измерений.

Ключевые слова: транскрипция, РНК-полимераза, акустическая силовая спектроскопия, одномолекулярные методы

Финансирование: Исследование выполнено при финансовой поддержке Российской Федерации в лице Министерства науки и высшего образования Российской Федерации (соглашение № 996-2021-15-075 от 23.09.2021).

Для цитирования: Арсениев А. Н., Панфилов М. А., Побегалов Г. Е., Потысьева А. С., Павлинова П. А., Якунина М. В., Ходорковский М. А. Характеризация на уровне одиночных молекул параметров транскрипции бактериальной РНК-полимеразы методом акустической силовой спектроскопии // Научно-технические ведомости СПбГПУ. Физико-математические науки. 2022. Т. 15. № 1. С. 70–80. DOI: https://doi.org/10.18721/ JPM.15107

Introduction

The transcription process resulting in gene expression by DNA-dependent RNA polymerase (RNAP) has been considered in a huge number of studies, most of them performed using classical biochemical methods. These methods only offer limited possibilities for obtaining detailed characteristics of the given process. Furthermore, crucial data is provided in structure studies focused on bacterial RNAP–DNA complexes using cryoelectron microscopy, nuclear magnetic resonance spectroscopy and X-ray crystallography. While these methods yield essential data on some of the longest-lived states of these complexes, less details can be uncovered about the intermediate, short-lived states governing the dynamics of the process.

As a matter of fact, unambiguous data on these dynamics can only be obtained by single-molecule techniques allowing to monitor the mechanistic changes of individual molecules in real time, without averaging over an ensemble of particles. The most commonly used single-molecule techniques are optical or magnetic tweezers and single-molecule Förster resonance energy transfer (smFRET).

The number of studies incorporating these methods to gain detailed insights into the dynamics of transcriptional elongation has increased dramatically in the last 10–15 years [1–4]. The results indicated that various conformational states of RNAP (whose lifetimes differ by several orders of magnitude) evolve throughout the complex structural transformations during the single transcription steps – a nucleotide addition cycle, each corresponding in length to progression of RNA-polymerase by one base pair.

Here we employ acoustic force spectroscopy technique for single-molecule research of transcription elongation; the advantage of this approach is that data on the dynamics of several RNAP molecules can be extracted simultaneously. Since this method is relatively new, we focused on its capabilities and the particulars of the technique developed based on the method.

Here we perform new data characterizing the dynamic pattern of bacterial RNAP transcription under specific conditions.

Acoustic force spectroscopy for transcription analysis

The method of acoustic force spectroscopy (AFS) was first presented in late 2014 [3]. The studies were run on a specially made Lumicks setup including a customized microfluidic chip, an inverted microscope, and a camera. The microfluidic chip used in the experiments is a chamber bounded by two glass plates with fluid in between. Applying a voltage to a piezo element attached to this chip generates a plane acoustic wave acting on polymer microspheres; their displacements were tracked with an inverted microscope and camera. DNA molecules are tethered between the surface of the cover glass and the microspheres (Fig. 1). A force of an acoustic nature acts on the microspheres.

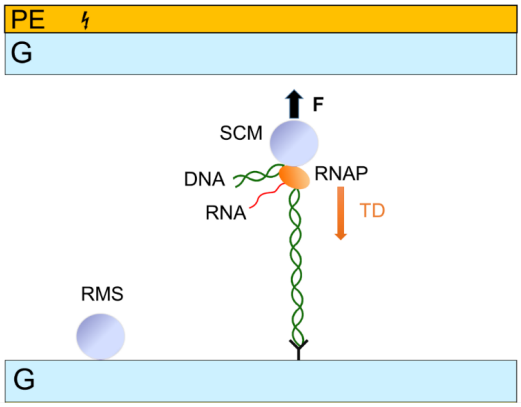

Fig. 1. The configuration of the AFS experiment:
piezo element PE; glass G; streptavidin-coated microsphere SCM and reference microsphere RMS; DNA, RNA; biotin-modified RNAP; transcription direction TD; applied force **F**

The acoustic wave propagating inside the chip generates the force acting on the microspheres:

$$F = -V\nabla\left[\frac{1-k^*}{4}k_m p^2 - \frac{\rho^* - 1}{2\rho^* + 1}\rho_m v^2\right], \quad (1)$$

where V, m^3, is the volume of the microsphere; p, Pa, is acoustic pressure; v, m/s, is the speed of sound; $\rho^* = \rho_p/\rho_m$ is the density ratio between the microsphere and the medium; $k^* = k_p/k_m$ is the ratio of elasticity coefficients between the microsphere and the medium.

The magnitude of the force F (see Fig. 1) depends on the size of the microsphere, the frequency of the acoustic wave and its amplitude, which in turn depends on the voltage applied to the piezo element [3].

The forces applied in the method generally range from units to tens and even hundreds of piconewtons, which underlies its potential for studies of biological objects [5].

While the AFS method itself has a simple design, the experiments performed needed a lengthy and complicated protocol.

A DNA molecule should be obtained at the preparation stage before the experiment; this molecule is subsequently tethered to one of the surfaces of the microfluidic chip. To achieve this, the DNA and the surface are modified, respectively, with digoxigenin and anti-Dig antibodies, compounds forming a chemical bond during interaction. It can be seen from Fig. 1 that RNA polymerase must be chemically bound to the microsphere in order to conduct the experiment. For these purposes RNAP modified by biotin is used. Thus, biotinylated RNAP is strongly binding to the streptavidin covered microspheres [6].

The transcription cycle performed by RNA polymerase (regardless of cell type) includes three stages: initiation, elongation, and termination. During initiation, RNAP binds to the promoter sequence, with the bound double-stranded DNA melting as a result and open RNAP–DNA complexes forming. The elongation stage when RNA molecules are actively synthesized follows next. RNAP moves along the DNA in leaps, this enzyme can stop either temporarily (i.e., pause) or permanently (i.e., arrest) during elongation. Moreover, RNA synthesis can be terminated in response to regulatory events from protein factors and/or signals encoded in DNA and RNA [7, 8].

AFS allows to simultaneously track the dynamics for several RNAP molecules moving along the DNA, which is an advantage over other single-molecule methods where only the position of a one RNAP molecule can be detected in real time [9, 10].

Elongation profiles demonstrate the dynamic characteristics of a single RNAP, such as instantaneous (between pauses) and average rate, the presence of arrests/pauses and their duration. The profiles are the graphical interpretation for the characteristic motion of single polymerases responsible for transcriptional elongation, presented as the time dependence of the transcribed DNA length (in nanometers or nucleotides) on time (seconds).

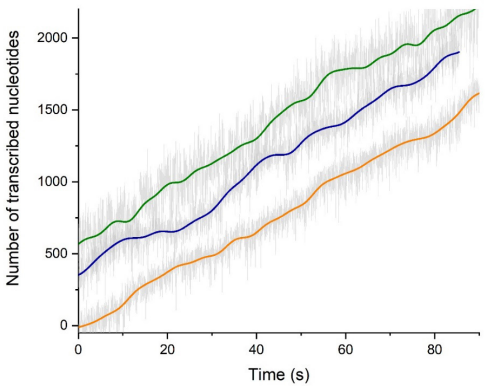

Fig. 2. Representative elongation profiles for three individual RNAPs under conditions without the influence of chemical agents

Algorithm for processing the elongation profiles

A typical shape of the elongation profiles for three single RNA polymerases in the absence of any chemical agents affecting transcription is shown in Fig. 2.

A median filter with a window of several seconds is used to process the obtained data, and a Savitzky–Golay filter is applied for repeated smoothing [11]. Transcription rate thresholds and all-time intervals where the velocities falling below the threshold value are regarded as pauses are given. These pauses are sorted into 'long' ones, lasting over 20 s, and 'short' ones, lasting from 2.5 to 20 s [12, 13]. The resolution of the setup does not allow to determine pauses shorter than 2.5 s. The threshold value is chosen to equal 0.5 σ, where σ is the standard deviation from the mean, obtained from the Gaussian distribution for instantaneous rates. The Gaussian function $f(x)$ has the form

$$f(x) = \frac{1}{\sigma\sqrt{2\pi}} e^{-\frac{1}{2}\left(\frac{x-\mu}{\sigma}\right)^2}.$$

The values extracted are averaged over the entire ensemble of pauses and are represented as (mean ± standard error of the mean (sem)). The Mann–Whitney test is used as a criterion for statistical significance. The distribution of instant velocities is generated by processing with the selected rate threshold.

In the general case, the velocity distribution contains signals corresponding to the derivatives of noise and useful signal. The noise component is determined by the parameters of the experimental setup, and its spectrum corresponds to the distribution of derivatives for those sections of the elongation profile where the polymerase progression is stopped, i.e., when it dwells in paused states. The noise derivative has a symmetrical distribution with respect to zero rate; its contribution can be considered using the negative part of the distribution, which is not superimposed by the useful signal. Since the positive values of the noise signal are equal in magnitude to its negative values, the true distribution of instant velocities can be obtained by subtracting the absolute values of the noise signal from the total transcription rate distribution. This method was previously successfully applied in [14, 15]. Fig. 3,*a* shows a histogram for one of the obtained elongation profiles with a pronounced bimodal distribution for the example described. Expansion of this distribution using Gaussian functions allows isolating the distribution near zero (red curve) corresponding to the noise component of the signal, and the true instant transcription velocity (green curve).

The parameters of the instantaneous transcription rate can be determined more precisely using the noise subtraction procedure described above.

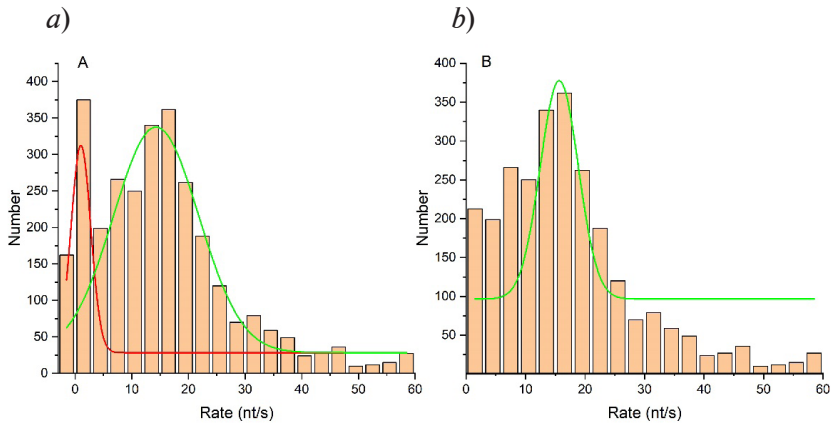

Fig. 3. Histograms of instant transcription rate distributions before (*a*) and after (*b*) subtracting the absolute values of the noise component from the signal and approximation by the Gaussian function (green curves correspond to the instantaneous rate, red to the noise component)

Fig. 3,*b* shows the approximation of the transcription rate distribution by the Gaussian function after subtracting the noise signal. As evident from the approximation results, the value of instantaneous transcription rate extracted by this procedure is higher and likely closer to the true values of instant transcription rate in polymerase.

After these measures are performed for each elongation profile obtained, the data for all profiles corresponding to the specific experimental conditions are averaged and represented as (mean value ± sem).

The value of the average transcription velocity for each RNA polymerase is equal to the ratio of the path traveled by the polymerase (the elongation profile length) to the total travel time. The obtained values are averaged over the entire ensemble of velocities for each of the experimental conditions and are represented as (mean value ± sem). The Mann–Whitney test is used as a criterion for statistical significance.

Effect of magnesium ions on transcription parameters

To assess the effect of magnesium ions on the transcription process, we compared the parameters of elongation profiles measured at $MgCl_2$ concentrations equal to 1 and 10 mM. Representative elongation profiles for single RNAPs at various magnesium concentrations are shown in Fig. 4.

The values of instant and average transcription velocities at a magnesium chloride concentration of 10 mM, obtained after averaging over 28 elongation profiles (Fig. 5), turned out to be 20.5 ± 0.9 and 17 ± 0.7 nucleotides per second (nt/s; mean value ± sem).

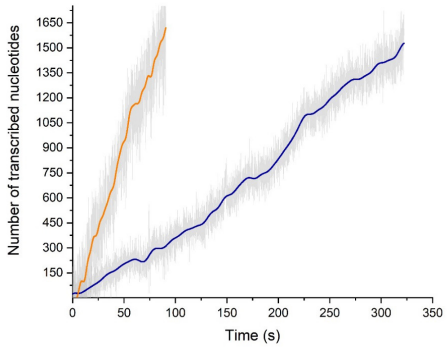

Fig. 4. Representative elongation profiles of instantaneous RNAPs for $MgCl_2$ concentrations equal to 1 mM (blue curve) and 10 mM (red curve)

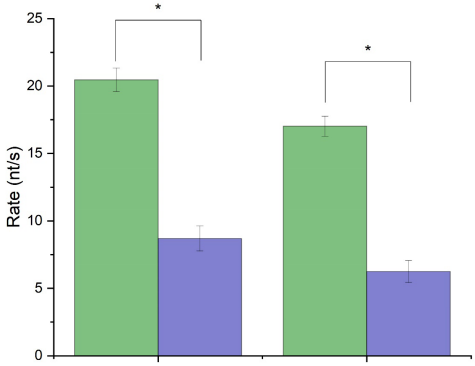

Fig. 5. Diagram for values of instantaneous (left) and average (right) transcription rates for $MgCl_2$ concentrations of 10 mM (green bars) and 1 mM (blue bars). The concentration of nucleoside triphosphates (NTP) is 1 mM

The numerical values of these quantities practically coincide with the data obtained previously [6, 16, 17]. Such close values of the average and instant velocities and a small number of short pauses at a high concentration of magnesium ions indicate that RNA-polymerase is only motionless for a small period compared to the time spent on transcribing a DNA sequence, chosen equal to 500 nm ± 10% in these experiments. Large pauses (longer than 20 s) are not observed under these conditions, while a small number of short pauses (between 2.5 and 20 s) were found using the processing protocol above. Fig. 6 shows the results extracted by processing the entire data array, determining the average number of short pauses per one elongation profile.

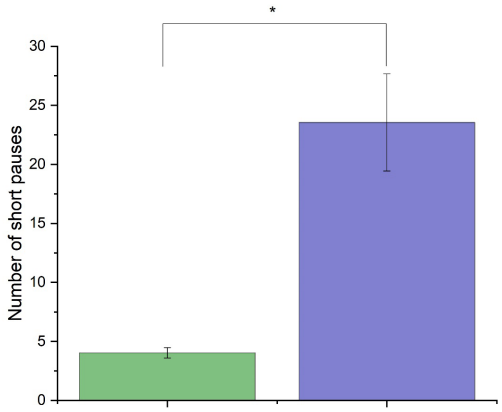

Fig. 6. Diagram of the average number of short transcription pauses per elongation profile for $MgCl_2$ concentrations of 10 mM (green bar) and 1 mM (blue bar).
The concentration of NTP is 1 mM

As seen from Fig. 4, the fundamental difference between the shape of elongation profile at low (1 mM of $MgCl_2$) and high (10 mM of $MgCl_2$) magnesium concentration is that it takes much longer for polymerase to travel the same length of DNA. No pauses longer than 20 s are observed in this case, the same as with a high magnesium concentration. The values of instantaneous and average rates, as well as the number of short pauses per one elongation profile, calculated by the same protocols as for a high concentration of magnesium ions, turned out to be 8.7 ± 0.9 and 6.3 ± 0.8 nt/s, respectively, as well as 23.6 ± 4 pauses (see Fig. 6).

First, we should note that the results obtained for the slowing down rate of transcriptional elongation with a decrease in the concentration of magnesium ions qualitatively agree with the data of biochemical experiments. However, the data provided by ensemble methods could not provide dynamic characteristics of potential processes affecting the value of the average transcription velocity.

As follows from our findings, the decrease in the average transcription velocity with decreasing concentration of magnesium ions is largely due to an increase in the number of short pauses. A possible mechanism behind these pauses is associated with the mismatched base composition within the active site of RNAP, necessary for the first stage of transcriptional elongation. This composition must contain a nucleotide complementary to the corresponding nucleotide of the template DNA strand and a magnesium ion. These components enter the active site of the polymerase through a secondary channel as a result of diffusion. Access of mismatched nucleotides to the active site of RNAP or the absence of magnesium ions within the site induce short pauses when RNAP can delete the mismatch from the active site.

Assuming that a pause happens by this mechanism, it should be expected that the number of cases with the absence of magnesium ions in the active site is greater at a low than at a high $MgCl_2$ concentration in the transcription buffer, and, accordingly, more short pauses are also observed at a low concentration, as confirmed by our study.

Notably, the resolution of the AFS setup does not allow detecting pauses shorter than 2.5 s, whose number is likely also significantly larger at low magnesium concentrations. In view of this, it can be assumed that the value of the instant elongation velocity (i.e., the rate between pauses) at a low concentration of magnesium ions is greater than the value obtained in this study by calculating this rate between pauses longer than 2.5 s.

Conclusion

We have developed a technique for measuring the RNA-polymerase transcriptional elongation profiles at the level of individual molecules by acoustic force spectroscopy (AFS), constructing an algorithm for analyzing the data extracted. This technique was used to study such transcription parameters as instant and average elongation velocities and the density of paused states of bacterial RNA polymerase. Moreover, it was demonstrated the quantity dependence of these paused states on the concentration of magnesium ions. The parameter values obtained made it possible to draw conclusions about the possible mechanism behind the short pauses generated at the stage of transcriptional elongation by bacterial RNAP.

REFERENCES

1. **Dulin D., Lipfert J., Moolman M. C., Dekker N. H.,** Studying genomic processes at the single-molecule level: introducing the tools and applications, Nat. Rev. Genet.. 2013. Vol. 14 (1) (2013) 9–22.

2. **Kamsma D., Creyghton R., Sitters G., et al.,** Tuning the music: Acoustic force spectroscopy (AFS) 2.0, Methods. 105 (1 August) (2016) 26–33.

3. **Sitters G., Kamsma D., Thalhammer G., et al.,** Acoustic force spectroscopy, Nat. Methods. 12 (1) (2015) 47–50.

4. **Mohapatra S., Lin Ch.-T., Feng X. A., et al.,** Single-molecule analysis and engineering of DNA motors, Chem. Rev. 120 (1) (2020) 36–78.

5. **Yin H., Wang M. D., Svoboda K., et al.,** Transcription against an applied force, Sci. 270 (5242) (1995) 1653–1657.

6. **Metelev M., Arseniev A., Bushin L. B., et al.,** Acinetodin and klebsidin, RNA polymerase targeting lasso peptides produced by human isolates of *Acinetobacter gyllenbergii* and *Klebsiella pneumonia*, ACS Chem. Biol. 12 (3) (2017) 814–824.

7. **Nudler E.,** RNA polymerase backtracking in gene regulation and genome instability, Cell. 149 (7) (2012) 1438–1445.

8. **Saba J., Chua X. Y., Mishanina T. V., et al.,** The elemental mechanism of transcriptional pausing, eLife. (Jan. 8) (2019) e40981.

9. **Zhao Y., Chen D., Yue H., et al.,** Lab-on-a-chip technologies for single-molecule studies, Lab Chip. 13 (12) (2013) 2183.

10. **Neuman K.C., Nagy A.,** Single-molecule force spectroscopy: Optical tweezers, magnetic tweezers and atomic force microscopy, Nat. Methods. 5 (6) (2008) 491–505.

11. **Savitzky A., Golay M. J. E.,** Smoothing and differentiation, // Anal. Chem. 36 (8) (1964) 1627–1639.

12. **Neuman K. C., Abbondanzieri E. A., Landick R., et al.,** Ubiquitous transcriptional pausing is independent of RNA polymerase backtracking, Cell. 115 (4) (2003) 437–447.

13. **Shaevitz J. W., Abbondanzieri E. A., Landick R., Block S. M.,** Backtracking by single RNA polymerase molecules observed at near-base-pair resolution, Nature. 426 (6967) (2003) 684–687.

14. **Hodges C., Bintu L., Lubkowska L., et al.,** Nucleosomal fluctuations govern the transcription dynamics of RNA polymerase II, Sci. 325 (5940) (2009) 626–628.

15. **Bintu L., Ishibashi T., Dangkulwanich M., et al.,** Nucleosomal elements that control the topography of the barrier to transcription, Cell. 151 (4) (2012) 738–749.

16. **Mejia Y. X., Nudler E., Bustamante C.,** Trigger loop folding determines transcription rate of *Escherichia coli*'s RNA polymerase, Proc. Natl. Acad. Sci. 112 (3) (2015) 743–748.

17. **Adelman K., Yuzenkova J., La Porta A., et al.,** Molecular mechanism of transcription inhibition by peptide antibiotic microcin J25, Mol. Cell. 14 (6) (2004) 753–762.

СПИСОК ЛИТЕРАТУРЫ

1. **Dulin D., Lipfert J., Moolman M. C., Dekker N. H.** Studying genomic processes at the single-molecule level: introducing the tools and applications // Nature Reviews Genetics. 2013. Vol. 14. No. 1. Pp. 9–22.

2. **Kamsma D., Creyghton R., Sitters G., Wuite G. J., Peterman E. J.** Tuning the music: Acoustic force spectroscopy (AFS) 2.0 // Methods. 2016. Vol. 105. 1 August. Pp. 26–33.

3. **Sitters G., Kamsma D., Thalhammer G., Ritsch-Marte M., Peterman E. J. G., Wuite G. J. L.** Acoustic force spectroscopy // Nature Methods. 2015. Vol. 12. No. 1. Pp. 47–50.

4. **Mohapatra S., Lin Ch.-T., Feng X. A., Basu A., Ha T.** Single-molecule analysis and engineering of DNA motors // Chemical Reviews. 2020. Vol. 120. No. 1. Pp. 36–78.

5. **Yin H., Wang M. D., Svoboda K., Landick R., Block S. M., Gelles J.** Transcription against an applied force // Science. 1995. Vol. 270. No. 5242. Pp. 1653–1657.

6. **Metelev M., Arseniev A., Bushin L. B., Kuznedelov K., Artamonova T. O., Kondratenko R., Khodorkovskii M., Seyedsayamdost M. R., Severinov K.** Acinetodin and klebsidin, RNA polymerase targeting lasso peptides produced by human isolates of *Acinetobacter gyllenbergii* and *Klebsiella pneumoniae* // ACS Chemical Biology. 2017. Vol. 12. No. 3. Pp. 814–824.

7. **Nudler E.** RNA polymerase backtracking in gene regulation and genome instability // Cell. 2012. Vol. 149. No. 7. Pp. 1438–1445.

8. **Saba J., Chua X. Y., Mishanina T. V., Nayak D., Windgassen T. A., Mooney R. A., Landick R.** The elemental mechanism of transcriptional pausing // eLife. 2019. January 8. P. e40981.

9. **Zhao Y., Chen D., Yue H., French J. B., Rufo J., Benkovic S. J., Huang T. J.** Lab-on-a-chip technologies for single-molecule studies // Lab on a Chip. 2013. Vol. 13. No. 12. P. 2183.

10. **Neuman K.C., Nagy A.** Single-molecule force spectroscopy: Optical tweezers, magnetic tweezers and atomic force microscopy // Nature Methods. 2008. Vol. 5. No. 6. Pp. 491–505.

11. **Savitzky A., Golay M. J. E.** Smoothing and differentiation // Analytical Chemistry. 1964. Vol. 36. No. 8. Pp. 1627–1639.

12. **Neuman K. C., Abbondanzieri E. A., Landick R., Gelles J., Block S. M.** Ubiquitous transcriptional pausing is independent of RNA polymerase backtracking // Cell. 2003. Vol. 115. No. 4. Pp. 437–447.

13. **Shaevitz J. W., Abbondanzieri E. A., Landick R., Block S. M.** Backtracking by single RNA polymerase molecules observed at near-base-pair resolution // Nature. 2003. Vol. 426. No. 6967. Pp. 684–687.

14. **Hodges C., Bintu L., Lubkowska L., Kashlev M., Bustamante C.** Nucleosomal fluctuations govern the transcription dynamics of RNA polymerase II // Science. 2009. Vol. 325. No. 5940. Pp. 626–628.

15. **Bintu L., Ishibashi T., Dangkulwanich M., Wu Yu-Yi, Lubkowska L., Kashlev M., Bustamante C.** Nucleosomal elements that control the topography of the barrier to transcription // Cell. 2012. Vol. 151. No. 4. Pp. 738–749.

16. **Mejia Y. X., Nudler E., Bustamante C.** Trigger loop folding determines transcription rate of *Escherichia coli*'s RNA polymerase // Proceedings of the National Academy of Sciences. 2015. Vol. 112. No. 3. Pp. 743–748.

17. **Adelman K., Yuzenkova J., La Porta A., Zenkin N., Lee J., Lis J. T., Borukhov S., Wang M. D., Severinov K.** Molecular mechanism of transcription inhibition by peptide antibiotic microcin J25 // Molecular Cell. 2004. Vol. 14. No. 6. Pp. 753–762.

THE AUTHORS

ARSENIEV Anatolii N.
Peter the Great St. Petersburg Polytechnic University
29 Politechnicheskaya St., St. Petersburg, 195251, Russia
arsenievanatoly@gmail.com
ORCID: 0000-0003-0901-4188

PANFILOV Mikhail A.
Peter the Great St. Petersburg Polytechnic University
29 Politechnicheskaya St., St. Petersburg, 195251, Russia
miha-panf@yandex.ru
ORCID: 0000-0003-2875-7315

POBEGALOV Georgii E.
Peter the Great St. Petersburg Polytechnic University
29 Politechnicheskaya St., St. Petersburg, 195251, Russia
lwdrums@gmail.com
ORCID: 0000-0003-0836-0732

POTYSEVA Alina S.
Peter the Great St. Petersburg Polytechnic University
29 Politechnicheskaya St., St. Petersburg, 195251, Russia
alina.potyseva@yandex.ru
ORCID: 0000-0003-0121-1494

PAVLINOVA Polina A.
Peter the Great St. Petersburg Polytechnic University
29 Politechnicheskaya St., St. Petersburg, 195251, Russia
polina.pavlina1004@gmail.com
ORCID: 0000-0003-4269-5632

YAKUNINA Maria V.
Peter the Great St. Petersburg Polytechnic University
29 Politechnicheskaya St., St. Petersburg, 195251, Russia
yakuninam@gmail.com
ORCID: 0000-0003-2083-3643

KHODORKOVSKII Mikhail A.
Peter the Great St. Petersburg Polytechnic University
29 Politechnicheskaya St., St. Petersburg, 195251, Russia
khodorkovskii@gmail.com
ORCID: 0000-0003-0562-0156

СВЕДЕНИЯ ОБ АВТОРАХ

АРСЕНИЕВ Анатолий Николаевич – *научный сотрудник научно-исследовательского комплекса «Нанобиотехнологии» Санкт-Петербургского политехнического университета Петра Великого.*
195251, Россия, г. Санкт-Петербург, Политехническая ул., 29
arsenievanatoly@gmail.com
ORCID: 0000-0003-0901-4188

ПАНФИЛОВ Михаил Андреевич – *лаборант-исследователь лаборатории молекулярной микробиологии Санкт-Петербургского политехнического университета Петра Великого.*
195251, Россия, г. Санкт-Петербург, Политехническая ул., 29
miha-panf@yandex.ru
ORCID: 0000-0003-2875-7315

ПОБЕГАЛОВ Георгий Евгеньевич – *кандидат физико-математических наук, научный сотрудник научно-исследовательского комплекса «Нанобиотехнологии» Санкт-Петербургского политехнического университета Петра Великого.*
195251, Россия, г. Санкт-Петербург, Политехническая ул., 29
lwdrums@gmail.com
ORCID: 0000-0003-0836-0732

ПОТЫСЬЕВА Алина Сергеевна – *студентка Санкт-Петербургского политехнического университета Петра Великого.*
195251, Россия, г. Санкт-Петербург, Политехническая ул., 29
alina.potyseva@yandex.ru
ORCID: 0000-0003-0121-1494

ПАВЛИНОВА Полина Андреевна – *лаборант-исследователь лаборатории молекулярной микробиологии Санкт-Петербургского политехнического университета Петра Великого.*
195251, Россия, г. Санкт-Петербург, Политехническая ул., 29
polina.pavlina1004@gmail.com
ORCID: 0000-0003-4269-5632

ЯКУНИНА Мария Вячеславовна – *кандидат биологических наук, научный сотрудник лаборатории молекулярной микробиологии Санкт-Петербургского политехнического университета Петра Великого.*
195251, Россия, г. Санкт-Петербург, Политехническая ул., 29
yakuninam@gmail.com
ORCID: 0000-0003-2083-3643

ХОДОРКОВСКИЙ Михаил Алексеевич – *кандидат физико-математических наук, директор научно-исследовательского комплекса «Нанобиотехнологии» Санкт-Петербургского политехнического университета Петра Великого.*
195251, Россия, г. Санкт-Петербург, Политехническая ул., 29
khodorkovskii@gmail.com
ORCID: 0000-0003-0562-0156

Received 07.12.2021. Approved after reviewing 15.12.2021. Accepted 15.12.2021.
Статья поступила в редакцию 07.12.2021. Одобрена после рецензирования 15.12.2021. Принята 15.12.2021.

Original article
DOI: https://doi.org/10.18721/JPM.15108

AGGREGATES OF MULTILAYERED PARTICLES: THE SPECTRAL CHARACTERISTICS OF LIGHT SCATTERING AND SIZE DISTRIBUTION FUNCTIONS

V. G. Kontsevaya [1] ✉, *A. P. Golovitskii* [2], *K. G. Kulikov* [2]

[1] Pskov State University, Pskov, Russia;

[2] Peter the Great St. Petersburg Polytechnic University, St. Petersburg, Russia

✉ nkoncevoi@mail.ru

Abstract: In the paper, a new mathematical model for calculating the spectral characteristics of biological particles imitating blood corpuscles, as well as their aggregates has been put forward. The model takes into account the aggregate structure and multiple light scattering effect on them. The methods and algorithms based on the T-matrix technique for calculating the laser radiation scattering on a biological cluster were considered. A particle size distribution function was determined on a basis of *in vitro* simulation experiment on light scattering by particle aggregates. A discussion of the obtained results was presented.

Keywords: T-matrix method, erythrocytes, Tikhonov regularization method

Citation: Kontsevaya V. G., Golovitskii A. P., Kulikov K. G., Aggregates of multilayered particles: the spectral characteristics of light scattering and size distribution functions, St. Petersburg Polytechnical State University Journal. Physics and Mathematics. 15 (1) (2022) 81–97. DOI: https://doi.org/10.18721/JPM.15108

Научная статья
УДК 517.95+577.3+535.8+519.6
DOI: https://doi.org/10.18721/JPM.15108

ОПРЕДЕЛЕНИЕ СПЕКТРАЛЬНЫХ ХАРАКТЕРИСТИК СВЕТОРАССЕЯНИЯ И ФУНКЦИИ РАСПРЕДЕЛЕНИЯ ПО РАЗМЕРАМ ДЛЯ АГРЕГАТОВ ИЗ МНОГОСЛОЙНЫХ ЧАСТИЦ

В. Г. Концевая [1] ✉, *А. П. Головицкий* [2], *К. Г. Куликов* [2]

[1] Псковский государственный университет, г. Псков, Россия;

[2] Санкт-Петербургский политехнический университет Петра Великого, Санкт-Петербург, Россия

✉ nkoncevoi@mail.ru

Аннотация. В статье представлена новая математическая модель для расчета спектральных характеристик биологических частиц, имитирующих форменные элементы крови, а также их агрегатов с учетом структуры и эффектов многократного светорассеяния. Рассмотрены методы и алгоритмы, базирующиеся на методе Т-матриц расчета рассеяния лазерного излучения на группе биологических частиц. Определена функция распределения частиц по размерам на основе данных модельного эксперимента по рассеянию света агрегатами биологических частиц в случае *in vitro*. Представлено обсуждение полученных результатов.

Ключевые слова: Т-матрица, эритроцит, метод регуляризации Тихонова, многократное светорассеяние, форменный элемент крови

Для цитирования: Концевая В. Г., Головицкий А.П., Куликов К. Г. Определение спектральных характеристик светорассеяния и функции распределения по размерам для агрегатов из многослойных частиц // Научно-технические ведомости СПбГПУ. Физико-математические науки. 2022. Т. 1 № .15. С. 81–97. DOI: https://doi.org/10.18721/JPM.15108

Introduction

The blood test is an essential tool in modern medical diagnostics, serving as a sensitive method for monitoring the variation in health parameters. Furthermore, such characteristics of blood cells as size, deformability and shape immediately affect the processes of gas exchange in the tissues.

Measuring the optical characteristics of blood cells is crucial for developing new methods to diagnose biological structures used in diverse biomedical applications [1, 2], for example, for diagnosing blood conditions. Constructing suitable mathematical models describing the propagation of light in biological tissues can contribute substantially to tackling this challenge.

Early diagnostics of platelet dysfunction (deviations in platelet size and shape, changes in their aggregation properties) and related clotting disorders is important for identifying the risks of diseases closely linked to such conditions. This primarily applies to coronary heart disease.

The absorption and scattering efficiency of laser radiation largely depends on activated platelets prone to aggregation and thrombogenicity.

The process of erythrocyte aggregation, caused by natural damage in this case, can trigger hypercoagulability by releasing erythrocytic coagulation factors into the blood.

Each specific disease accompanied by pathological aggregation of blood cells requires comprehensive study to carefully select the most effective laboratory technique for monitoring and analyzing this process. The main factors influencing such pathological processes and the mechanisms behind them are impairments in the structure and function of erythrocytes, especially their ability to aggregate.

The optical characteristics of blood are very sensitive to the aggregation parameters of such cell types as erythrocytes and platelets; in particular, such processes affect the absorption and scattering efficiency of laser radiation by blood.

Exploring the quantitative relationships between biological properties and optical characteristics of biological particle aggregates is of immediate interest for advancing new approaches in optical biopsy, optical tomography, analysis of photodynamic and photothermal destruction of tissues and cells forming them. In particular, potential aggregation between the simulated particles should be taken into account. This study reports on numerical simulation of multiple light scattering by particle aggregates imitating the given biological structures, carried out for the first time to quantitatively study the assembly of biological particles into aggregates.

Our goal was to describe in detail the newly developed mathematical model for interaction of laser radiation with aggregates of biological structures with varying degree of complexity and organization in different cell types, testing the model proposed in specific scenarios.

Solution of the light scattering problem for the case of particle aggregate

The phenomena of light scattering by particle aggregates (clusters, ensembles, etc.) even having simple shapes can be rather difficult to interpret since these phenomena are governed by the interactions of fields from all particles comprising the aggregate. It should be borne in mind that each particle modifies the field not only in the vicinity of the others (multiple scattering), but also due to far-field interference.

In general, multiple scattering should be accounted for by rigorous numerical methods. Some of these methods explicitly take into account the interactions between particles [3] (like the superposition T-matrix approach [4–6] and the discrete dipole approximation (DDA) [7]), while others regard the aggregate as a cluster, i.e., a single particle of complex shape (like the finite-difference time-domain method [8]).

Multiple scattering can be computed iteratively [9, 10], for example, by the successive order-of-scattering technique, which is considered a special case of the superposition method.

Let us focus on the problem of multiple light scattering by an ensemble of particles imitating blood cells that contain nuclei, plasma membranes and cytoplasm inherent to the given biological structure, characterized by various geometric and optical parameters close to the simulated object.

The decomposition coefficients corresponding to the fields of incident light and light scattered by the aggregate can be related by calculating the T-matrix for laser scattering by an aggregate composed of multilayered particles within the strict theory of multiple light scattering. Since multiple interactions within the aggregate components are taken into account, it can be concluded that the scattered fields are connected.

T-matrices are calculated in a local coordinate system associated with the center of the corresponding particle for each of the aggregate particles, since they are independent of incident radiation. We follow the standard representation of the electromagnetic field incident on the *j*th particle as the sum of the initial incident field of the light wave and the field scattered by an ensemble of other particles located in a medium with a refractive index *n*, writing the expression [11]:

$$E_{inc}(j) = E_0(j) + \sum_{l \neq j} E_{scat}(l, j), \tag{1}$$

where $E_{scat}(l,j)$ is the sum of the fields scattered by the *j*th particle (we use *l*, *j* to denote the indices to emphasize the transition from the *l*th to the *j*th coordinate system.

We apply the T-matrix to calculate the field scattered by the *j*th particle; it is included in this equation as $E_{scat}(l,j)$. A local coordinate system associated with the *j*th particle was selected to calculate the T-matrix.

Relying on the translational properties of vector spherical wave functions, we can further transform the decompositions with respect to these functions from coordinate systems associated with the *j*th particles to the coordinate system of the *l*th particle. As a result, we obtain a system of linear algebraic equations (SLAE) for finding the coefficients of the light field scattered by an ensemble of multilayered particles a^j_{mn}, b^j_{mn}:

$$\begin{gathered}\begin{pmatrix} a^j \\ b^j \end{pmatrix} = T^j_{12}\left[\begin{pmatrix} p^{i,j} \\ q^{i,j} \end{pmatrix} + \sum_{l \neq j}\begin{pmatrix} A(l,j) & B(l,j) \\ B(l,j) & A(l,j) \end{pmatrix}\begin{pmatrix} a^j \\ b^j \end{pmatrix}\right], \\ T^j_{12} = T^j_1 + T^j_2,\ T^j_1 = \begin{pmatrix} a^j_{n_{1p}} & 0 \\ 0 & b^j_{n1q} \end{pmatrix},\ T^j_2 = \begin{pmatrix} 0 & a^j_{n_{1q}} \\ b^j_{n1p} & 0 \end{pmatrix};\end{gathered} \tag{2}$$

the expressions for the coefficients $a^j_{n_p}$, $b^j_{n_q}$, $a^j_{n_q}$, $b^j_{n_q}$ given here are provided in [11, 12], while the quantities $A(l,j)$ and $B(l,j)$ are defined in [13, 14].

Problems on light scattering by dielectric objects imitating biological structures, in particular blood cells, often entail solving the so-called ill-conditioned SLAE.

SLAE of the form (2) was solved via a stable algorithm of biconjugate gradients [15]. This method is based on the conjugate gradient squared method and does not allow for unstable behavior of the residual and accumulation of round-off errors.

Convergence to the required solution was substantially improved by using the algorithm for solving preconditioned SLAE as an LU-decomposition [16].

Analyzing the graph in Fig. 1, showing the dependences of relative residual norm on the iteration number for the method of preconditioned biconjugate gradients, we can conclude that the method used clearly has satisfactory convergence.

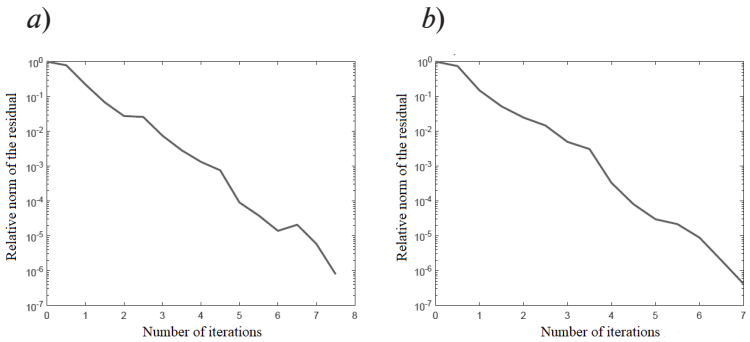

Fig. 1. Values of relative residual norm as a function of iteration number, obtained by the method of preconditioned biconjugate gradients.
Case of 4 particles in a layer, spaced 2 μm (*a*) and 1 μm (*b*) apart. Their parameters are given in Table

Table

Computational parameter sets for the problem of particle aggregates

Particle parameter	Parameter value for particle				
	I	II	III	IV	V
Distance between particles is 2 μm (Figs. 1,a and 2) and 1 μm (Fig. 1,b)					
Diameter, μm	6.5	6.5	7.0	7.6	–
Diameter, μm particle nucleus particle cytoplasm	 4.0 5.0	 4.0 6.0	 4.0 6.5	 4.0 6.5	
Refractive index of nucleus	1.37				
Refractive index of cytoplasm	1.00				
Refractive index of plasma membrane	1.33				
Distance between particles is 2 μm (Fig. 3) and 1 μm (Fig. 4)					
Diameter, μm	6.5	6.5	7.0	7.6	8.0
Diameter, μm particle nucleus particle cytoplasm	 4.0 5.0	 4.0 6.0	 4.0 6.5	 4.0 6.5	 3.0 4.0
Refractive index of nucleus	1.37				
Refractive index of cytoplasm	1.00				
Refractive index of plasma membrane	1.33				
Distance between particles is 2 μm (Fig. 5)					
Diameter, μm	6.6	6.6	7.1	7.7	8.1
Diameter, μm particle nucleus particle cytoplasm	 4.0 5.0	 4.0 6.0	 4.0 6.5	 4.0 6.5	 3.0 4.0
Refractive index of nucleus	1.37				
Refractive index of cytoplasm	1.34				
Refractive index of plasma membrane	1.33				
Distance between particles is 2 μm (Fig. 7)					
Diameter, μm	6.5	6.5	7.0	6.6	6.0
Refractive index of nucleus	1.37	1.33	1.33	1.37	1.37
Distance between particles is 1 μm (Fig. 9)					
Diameter, μm	6.5	6.5	7.0	8.6	12.0
Refractive index of nucleus	1.37	1.33	1.33	1.37	1.37

We developed a software package for computing T-matrices, taking into account multiple scattering for multilayered spherical structures. The T-matrix for spherical scatterers assumes a diagonal shape [17].

The software we have developed was used for fairly detailed analysis of the spectral characteristics of laser radiation (wavelength range from 400 to 650 nm) scattered by multilayered spherical particles.

Finding the numerical values of the coefficients a^j_{mn}, b^j_{mn} from expression (2), we can calculate such physical quantities as the absorption cross section (C_{abs}), scattering cross section (C_{sca}) and extinction cross section (C_{ext}), determined by the following procedure [18]:

$$C_{scat} = \frac{W_{scat}}{I_i},\ C_{ext} = \frac{W_{ext}}{I_i},\ C_{abs} = C_{ext} - C_{scat}, \tag{3}$$

where I_i is the intensity of incident light,

$$W_{scat} = \int_A S_{scat} \cdot e_r dA,\ W_{ext} = -\int_A S_{ext} \cdot e_r dA; \tag{4}$$

here

$$S_{scat} = \frac{1}{2}\Re[E^j_{scat} \times H^{j*}_{scat}],\ S_{ext} = \frac{1}{2}\Re[E^j_{inc} \times H^{j*}_{scat} + E^j_{scat} \times H^{j*}_{inc}]; \tag{5}$$

$$W_{scat} = \frac{1}{2}\Re\int_0^{2\pi}\int_0^{\pi}[E_{scat(\theta)}H^*_{scat(\phi)} - E_{scat(\phi)}H^*_{scat(\theta)}]r^2 \sin\theta d\theta d\phi, \tag{6}$$

$$W_{ext} = \frac{1}{2}\Re\int_0^{2\pi}\int_0^{\pi}[E_{inc(\phi)}H^*_{scat(\theta)} - E_{inc(\theta)}H^*_{scat(\phi)} - E_{scat(\theta)}H^*_{inc(\phi)} + E_{scat(\phi)}H^*_{inc(\theta)}]r^2 \sin\theta d\theta d\phi, \tag{7}$$

where

$$E_{inc(\theta)} = \sum_{n=1}^{\infty}\sum_{m=-n}^{n} E_{mn}\left[-ip^0_{mn}\psi'_n\tau_{mn} + q^0_{mn}\psi_n\pi_{mn}\right]\frac{e^{im\phi}}{kr}, \tag{8}$$

$$E_{inc(\phi)} = \sum_{n=1}^{\infty}\sum_{m=-n}^{n} E_{mn}\left[iq^0_{mn}\psi_n\tau_{mn} + p^0_{mn}\psi'_n\pi_{mn}\right]\frac{e^{im\phi}}{kr}, \tag{9}$$

$$H_{inc(\theta)} = \frac{k}{\omega\mu^0}\sum_{n=1}^{\infty}\sum_{m=-n}^{n} E_{mn}\left[ip^0_{mn}\psi_n\tau_{mn} - q^0_{mn}\psi'_n\pi_{mn}\right]\frac{e^{im\phi}}{kr}, \tag{10}$$

$$H_{inc(\phi)} = \frac{k}{\omega\mu^0}\sum_{n=1}^{\infty}\sum_{m=-n}^{n} E_{mn}\left[iq^0_{mn}\psi'_n\pi_{mn} + p^0_{mn}\psi_n\tau_{mn}\right]\frac{e^{im\phi}}{kr}, \tag{11}$$

$$E_{scat(\theta)} = \sum_{n=1}^{\infty}\sum_{m=-n}^{n} E_{mn}\left[-ia^j_{mn}\xi'_n\tau_{mn} - b^j_{mn}\xi_n\pi_{mn}\right]\frac{e^{im\phi}}{kr}, \tag{12}$$

$$E_{scat(\phi)} = \sum_{n=1}^{\infty}\sum_{m=-n}^{n} E_{mn}\left[-ib^j_{mn}\xi'_n\tau_{mn} - a^j_{mn}\xi'_n\pi_{mn}\right]\frac{e^{im\phi}}{kr}, \tag{13}$$

$$H_{scat(\theta)} = \frac{k}{\omega\mu^0}\sum_{n=1}^{\infty}\sum_{m=-n}^{n} E_{mn}\left[ia^j_{mn}\xi_n\pi_{mn} + b^j_{mn}\xi'_n\tau_{mn}\right]\frac{e^{im\phi}}{kr}, \tag{14}$$

$$H_{scat(\phi)} = \frac{k}{\omega\mu^0}\sum_{n=1}^{\infty}\sum_{m=-n}^{n} E_{mn}\left[ib^j_{mn}\xi'_n\pi_{mn} - a^j_{mn}\xi_n\tau_{mn}\right]\frac{e^{im\phi}}{kr}; \tag{15}$$

the following notations are used here: $\psi_n(\rho) = \rho j_n(\rho)$, $\xi_n(\rho) = \rho h^{(1)}_n(\rho)$ are the Riccati–Bessel functions; $E_{mn} = |E_0| i^n (2n+1)\frac{(n-m)!}{(n+m)!}$; the quantities q^0_{mn}, p^0_{mn} are defined in [11].

Substituting the expressions for the quantities $E_{inc(\theta)}$, $E_{inc(\phi)}$, $H_{inc(\theta)}$, $H_{inc(\phi)}$, $E_{scat(\theta)}$, $E_{scat(\phi)}$, $H_{scat(\theta)}$, $H_{scat(\phi)}$ to Eqs. (6) and (7), we obtain:

$$C_{scat} = \frac{4\pi}{k^2}\sum_{n=1}^{\infty}\sum_{m=-n}^{n}(n+1)(2n+1)\frac{(n-m)!}{(n+m)!}\left(\left|a^j_{mn}\right|^2 + \left|b^j_{mn}\right|^2\right), \tag{16}$$

$$C_{ext} = \frac{4\pi}{k^2}\sum_{n=1}^{\infty}\sum_{m=-n}^{n}(n+1)(2n+1)\frac{(n-m)!}{(n+m)!}\Re(p^{*0}_{mn}a^j_{mn} + q^{*0}_{mn}b^j_{mn}). \tag{17}$$

Based on expressions (12) for the θ-component of the scattered radiation intensity, we obtain

$$I_{scat(\theta)} = I_i \cdot \left| E_{scat(\theta)} \right|^2 .$$

We have thus obtained the formulas for determining the dependences of the above spectral characteristics on the wavelength of incident laser radiation (see Figs. 2–5).

We should note that the computations by the superposition T-matrix method in this paper were based on the Finite Difference Time Domain (FDTD) approach. A mathematical approach described in [12] was used for the problem on scattering by a multilayered sphere.

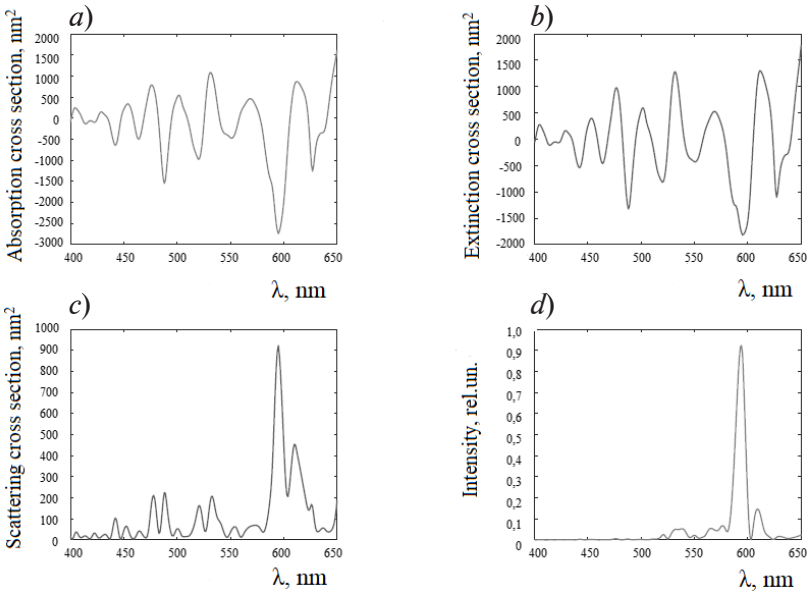

Fig. 2. Graphical representation of absorption cross sections (*a*), extinction cross section (*b*), scattering cross section (*c*) and scattered light intensity as functions of laser radiation wavelength incident at zero angle (*d*), for the given parameters of the problem
(4 particles in the layer, spaced 2 μm apart, see Table)

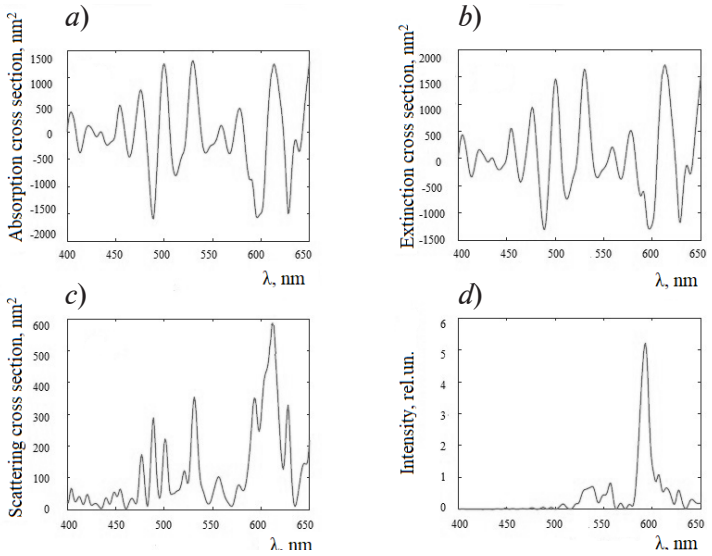

Fig. 3. Graphical representation of absorption cross sections (*a*), extinction cross section (*b*), scattering cross section (*c*) and scattered light intensity as functions of laser radiation wavelength incident at zero angle (*d*), for the given parameters of the problem
(5 particles in the layer, spaced 2 μm apart, see Table)

Determining the function for the size distribution of blood cells

The known variable (measured approximately) here is the intensity of light scattered by the aggregate of multilayered particles $I_{blood}(\lambda)$ imitating blood cells. Solving the problem should yield the size distribution of blood cells.

In this case, the quantity $I_{blood}(\lambda)$ is found through a model experiment to demonstrate the capabilities of the method (see graphs in Fig. 2,*d*–5,*d*).

Adopting the standard approach for such cases, the problem posed can be described by a linear Fredholm integral equation of the first kind, taking the following form:

$$Au \equiv \int_{\rho\min}^{\rho\max} I(\rho,\lambda)u(\rho)d\rho = f(\lambda), \tag{18}$$

where A is the integral operator; $I(\rho,\lambda)$ is the kernel of the integral equation; ρ is the equivalent radius, $\rho = ka$ (k is the magnitude of the wave vector, a is the particle radius); $u(\rho)$ is the required distribution of the cells over the sizes (equivalent radii); $f(\lambda)$ is the scattered light intensity by an ensemble of multilayered spherical particles, found by the model experiment, $f(\lambda) \equiv I_{blood}(\lambda)$.

This problem belongs to the class of so-called inverse ill-posed problems. The core of the integral equation $I(\rho,\lambda)$ is defined as the intensity of light scattered in the direction of the angle θ selected in the experiment by a multilayered spherical particle. We assume that $I(\rho,\lambda)$ is a continuous function in a rectangle

$$\Omega = ([c,d]\times[a,b]) \text{ and } f(\lambda) \in L_{2[c,d]},$$

where $a \equiv \rho_{\min}$, $b \equiv \rho_{\max}$, $c \equiv \lambda_{\min}$, $d \equiv \lambda_{\min}$.

Let $u(\rho)$ be a smooth function, when instead of f, its approximate value f_δ is known, such that $\|f - f_\delta\|_{L_{2[c,d]}} \le \delta$. Then we select the solution space as $U = W^1_{p[a,b]}$.

Let function $I_h(\rho,\lambda)$ be given instead of function $I(\rho,\lambda)$, while

$$\left\|I(\rho,\lambda) - I_h(\rho,\lambda)\right\|_{L_2(\Omega)} \le h;$$

then $\|A - A_h\|_{W^1_2 \to L_2} \le h$, where A_h is the approximation for the integral operator A with an accuracy h in the operator norm, which corresponds to the kernel $I_h(\rho,\lambda)$.

Notably, inversion of the operator A for the inverse problem (see expression (18)) is unstable for space $W^1_{p[a,b]}$. Then the Tikhonov regularization method can be used to numerically find the distribution $u(\rho)$.

Let us write the Tikhonov equation [19, 20]:

$$(A_h^* A_h + \alpha C)u^\alpha = A_h^* f,$$

where A_h is an operator from the space $W^1_{2[a,b]}$ to the subspace $L_{2[c,d]}$; A_h^* is an operator from $L_{2[c,d]}$ to $W^1_{2[a,b]}$ (conjugated to A_h); C is some operator whose matrix is defined in monograph [20].

Notably, we assume in this statement that there is no information about the smoothness of the exact solution; then we regard the operator A_h from the initial integral equation as acting from $L_{2[a,b]}$ to $L_{2[c,d]}$. In this case, the smoothing functional takes the form

$$M^\alpha[u] = \left\|A_h u^\alpha - f_\delta\right\|^2_{L_{2[c,d]}} + \alpha\left\|u\right\|^2_{L_{2[c,d]}} \to \min, \tag{19}$$

and the Tikhonov equation takes the form

$$(A_h^* A_h + \alpha E)u^\alpha = A_h^* f,$$

where E is the unit operator.

The function u^α minimizing the functional (19) depends on the value of the regularization parameter α.

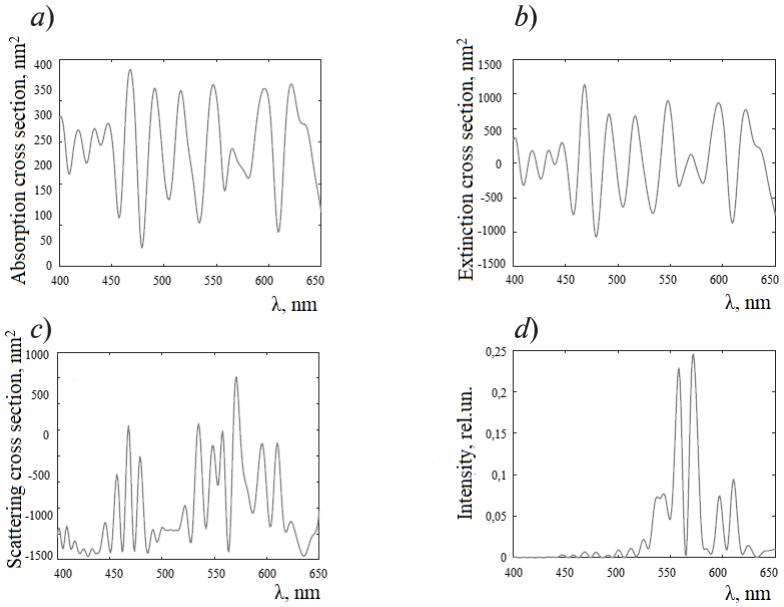

Fig. 4. Graphical representation of absorption cross sections (*a*), extinction cross section (*b*), scattering cross section (*c*) and scattered light intensity as functions of laser radiation wavelength incident at zero angle (*d*), for the given parameters of the problem
(5 particles in the layer, spaced 1 μm apart, see Table)

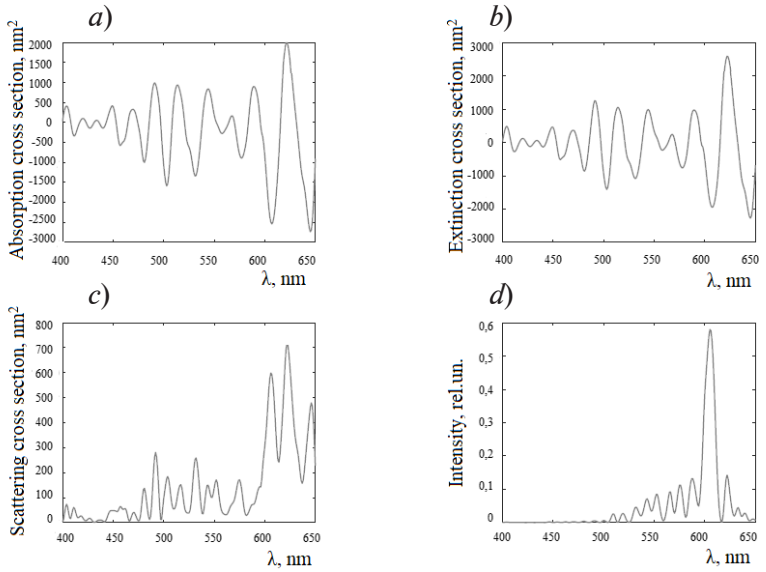

Fig. 5. Graphical representation of absorption cross sections (*a*), extinction cross section (*b*), scattering cross section (*c*) and scattered light intensity as functions of laser radiation wavelength incident at zero angle (*d*), for the given parameters of the problem
(5 particles in the layer, spaced 2 μm apart, see Table)

The regularization parameter providing optimal agreement between the experimental data and a priori information is selected for this case by the following approaches: relative residual method, quasi-optimality criterion, smoothing functional principle, *L*-curve method [19, 20]. The software package we have developed in this study was used to select the regularization parameter automatically by the predefined errors of both the integral equation kernel and the experimental data (see Figs. 6 and 8 below).

Results and discussion

The results obtained (see Fig. 2–5) confirm that the mathematical approach outlined in the study and the software package we have developed here based on it allow detecting the aggregation of simulated particles and their parameters, since varying the distance between the particles is accompanied by not only variation in the numerical values of spectral characteristics but also in the shape of the curves, as can be seen from the figures. We considered multiple light scattering by an ensemble of spherical particles with inclusions of concentric spheres with different radii.

Figs. 2,*d*–5,*d* graphically represent the scattering intensities and scattering cross sections of laser radiation as functions of radiation wavelength for different problem parameters (the parameters are summarized in Table).

It should be noted that the scattering cross section characterizes the efficiency of angle-resolved light scattering by a particle. In particular, the differences in both the scattering cross sections and its intensities for different biological substances follow from the difference in the sizes of the blood cells themselves, as well as the variability in their internal structures.

To find the erythrocyte distribution function over the equivalent radii, we solved the problem on mathematically describing the interaction of laser radiation with an aggregate consisting of a finite number of particles, taking into account their structure and the effects of multiple light scattering, as well as with the exactly given geometric and optical characteristics. Erythrocytes act as model particles. It bears mentioning that simulating the erythrocyte as a homogeneous scatterer is fairly reasonable, as it lacks cellular organelles and has a thin cell membrane (with little effect on light scattering). Some studies even generally assume the erythrocyte to be a structurally homogeneous sphere [21, 22].

To illustrate the methods described above, let us first consider the size distributions of erythrocytes used in medical practice [23]:

$$u(\rho) = A_1 \cdot e^{B_1(\rho - b_1)^2}, \tag{20}$$

$$u(\rho) = A_2 \cdot e^{B_2(\rho - b_2)^2} + A_3 \cdot e^{B_3(\rho - b_3)^2}. \tag{21}$$

The normal distribution is described by a formula of the type (20) ($A_1 = 1$, $B_1 = -3$, $b_1 = 3$); the bimodal distribution corresponds to a formula of the type (21), while the fraction of abnormally large cells amounts to 30% ($A_2 = 0.80$, $B_2 = -1.00$, $b_2 = 3.00$, $A_3 = 0.25$, $B_3 = -2.30$, $b_3 = 5.0$) [23].

We used different methods to select the regularization parameter α for the normal size distribution of erythrocytes:

by the residual, where $\|Au^\alpha - f\|/\|f\| = \delta$, the value of $\alpha = 0.00216$ (Fig. 6,*a*);

by the quasi-optimality criterion, where $\|\alpha u^\alpha / d\alpha\|$, the value of $\alpha = 1.1059 \cdot 10^{-9}$ (Fig. 6,*b*);

by the *L*-curve criterion, where $L^* = \lg\|Au^\alpha - f\|, \lg\|u^\alpha\|$, the value of $\alpha = 2.7648 \cdot 10^{-8}$ (Fig. 6,*c*);

by the smoothing functional principle, where $(\alpha\|u^\alpha\|^2 + \|Au^\alpha - f\|^2)/\|f\|^2) = C\delta^2$, the value of $\alpha = 0.00216$ (Fig. 6,*d*).

The optimal value of the regularization parameter amounted to

$$\alpha_{opt} = 0.002160 \text{ for } h = 0.11, \delta = 0.10.$$

Let us examine the graphs of the two functions in Fig. 7. The size distribution function (20) is represented by a continuous curve, and the result of the numerical solution to the inverse problem is represented by dotted curves with the noise level on the right side of Eq. (18) taken to equal 5%. Evidently, the curves practically coincide. It is thus clear that the shape of particle size distribution defined by expression (20) was restored with high accuracy from numerical solution to the problem of the form (18). Moreover, we can reasonably assume that the resulting distribution curve is close to the standard Price–Jones curve characterizing the distribution of erythrocytes in the blood of a healthy person [24].

The same as for the case of normal distribution, Fig. 8 illustrates the selection of the regularization parameter α for the case of bimodal size distribution of erythrocytes. The following results were obtained for the selection: by residual, $\alpha = 0.012805$ (Fig. 8,*a*); by quasi-optimality criterion, $\alpha = 1.311200 \cdot 10^{-9}$ (Fig. 8,*b*); by *L*-curve criterion, $\alpha = {}^{8-}10 \cdot 3.27810$ (Fig. 8,*c*); by smoothing functional principle, $\alpha = 0.00216$ (Fig. 8,*d*).

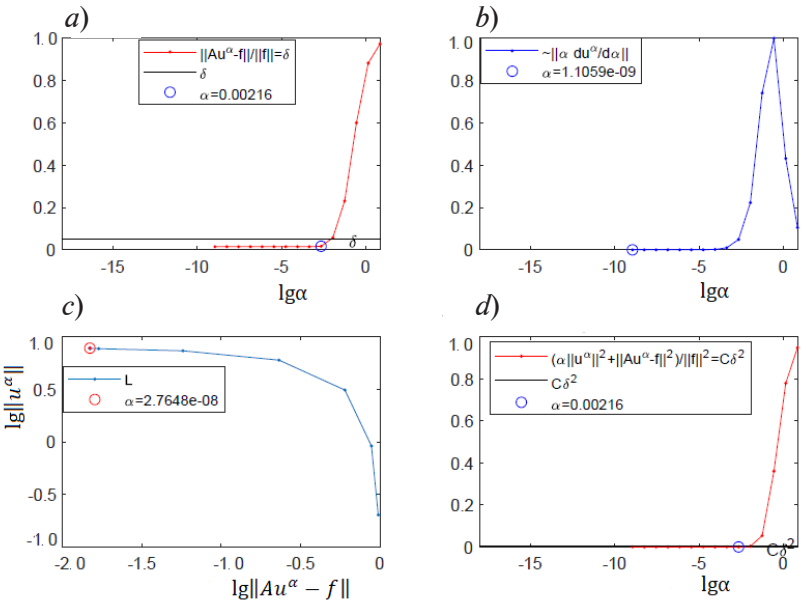

Fig. 6. Regularization parameter found by relative residual method (*a*), by quasi-optimality criterion (*b*) and *L*-curve criterion (*c*), by smoothing functional principle (*d*).
Case of normal size distribution of the particles.
The final optimal value of the required parameter is given in the text

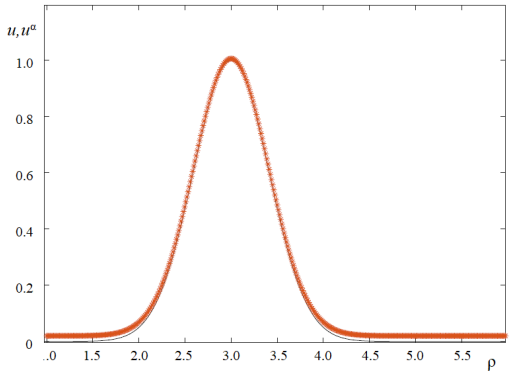

Fig. 7. Computed functions $u(\rho)$ (see Eq. (20), black solid curve) and $u^{\alpha}(\rho)$ (numerical solution of the inverse problem, colored curve) for distributions of 5 particles over the equivalent radii ρ;
particles are spaced 2 μm apart (see Table)

The optimal value of the regularization parameter amounted to

$$\alpha_{opt} = 0.012805 \text{ for } h = 0.11, \delta = 0.10.$$

Let us now consider the computational data presented in Fig. 9. A predetermined asymmetric bimodal size distribution (21) is shown by a continuous line. Such a distribution simulates the presence of fractions of normal and abnormally large erythrocytes.

The numerical solution of the problem allowed to reconstruct the intensities of both peaks on the particle size distribution with a high degree of accuracy (the peaks correspond to the fractions of typical and abnormally large cells).

The solution obtained by minimization corresponds to the model dependences predetermined for different types of distributions with an acceptable degree of accuracy. The error estimate that we obtained gives a satisfactory representation of the noise level in the right-hand side.

Thus, we have conclusively proved that a priori information about the smoothness and finiteness of the solution can be used to accurately reconstruct the distribution of erythrocytes over the equivalent radii and determine the variations in their width, which has major practical implications for modern medicine [25].

The mathematical model developed can serve for determining the size distribution function for particles imitating blood cells *in vitro*.

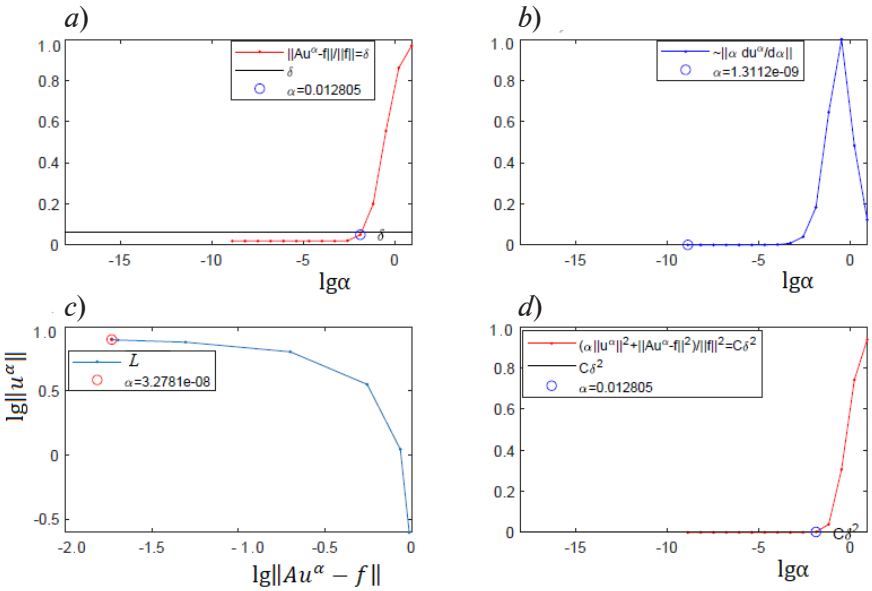

Fig. 8. Regularization parameter found by relative residual method (*a*), by quasi-optimality criterion (*b*) and *L*-curve criterion (*c*), by smoothing functional principle (*d*).
Case of bimodal size distribution of the particles.
The final optimal value of the required parameter is given in the text

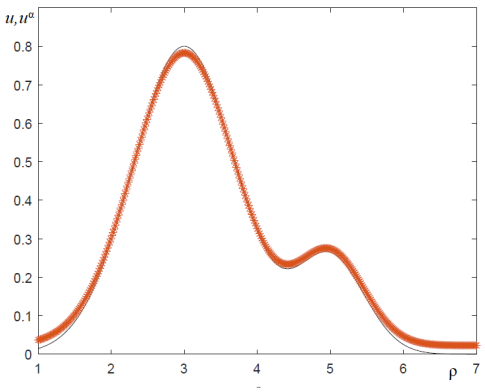

Fig. 9. Computed functions $u(\rho)$ (see Eq. (21), gray solid curve) and $u^{\alpha}(\rho)$ (numerical solution of the inverse problem, colored curve) for distributions of 5 particles along the equivalent radii ρ;
particles are spaced 1 μm apart (see Table)

Conclusion

Let us now summarize our key findings.

1. We have constructed a conceptually new model suitable for predicting the spectral characteristics in aggregates of spherical particles with a complex structure. The model can be used *in vitro* and takes a self-consistent approach to describing multiple light scattering by biological structures.

2. The model proposed can successfully yield the spectral distributions of optical parameters in a biological medium, which vary depending on different factors and induce fluctuations in the function and morphology of biological tissues (for example, aggregation of blood cells).

3. Effective software has been developed based on the given mathematical model, allowing to extract the size distributions of blood cells from the experimental data.

4. The results provided by the model show good sensitivity to fluctuations in the geometric characteristics of blood cell nucleus and plasma membrane. Such sensitivity allows to examine the physiological processes occurring in the body: for example, as the refractive index of the medium is increased by 0.34 (and, accordingly, the diameter of the simulated particles by 0.1 μm), the spectral characteristics of these particles change significantly (see the curves in Figs. 3 and 5). We should note that the changes in the size of the cell nucleus are often associated with the changes in metabolism in the human body induced by cell damage or physiological dysfunction.

The type of simulation outlined in this paper can be used to diagnose various conditions. For example, it is argued in [26] that the variations in the refractive index of the medium in the cell nucleus point to an initiating division process (mitosis), while [27] has established that the nucleus of a cancer cell exhibits internal structural changes compared to normal cells, associated with the geometric characteristics of the object considered.

The mathematical model constructed and the software based on it allow finding and analyzing the spectral characteristics for the optical parameters of the biological medium, in particular accounting for dynamics.

5. The new mathematical model provides a means for finding the particle distribution function over the equivalent radii for spherical particles with different structures, changing their geometric and optical characteristics, taking into account multiple scattering, which has major implications for medical practice.

An important result achieved in this study is that we developed a software package for computing light scattering by an aggregate whose structure includes layered spherical particles, additionally offering the options for accurately reconstructing the distribution of erythrocytes over the equivalent radii and measuring the variation in the width of such distributions. The software is valuable as an effective flexible tool for practitioners in biomedical optics; the optical characteristics and sizes of the biostructure considered can be tailored to record the dependences between them via a single automated setup.

The functions offered by the software package make it possible to collect a database for particles with different optical and geometric characteristics. This means that in the future, we will be able to comprehensively investigate the correlations between the optical characteristics and parameters of the biological substances simulated and their biological properties.

Data on the tendency towards aggregation in blood cells should open new avenues for qualitative assessment of changes in aggregation/disaggregation interactions accounting for the dynamics of the corresponding indicators.

REFERENCES

1. **Tuchin V. V.,** Optika biologicheskikh tkaney. Metody rasseyaniya sveta v meditsinskoy diagnostike [Biological tissue optics. Light scattering methods for medical diagnostics], IPR Media, Moscow, 2021 (in Russian).

2. **Tuchin V. V.,** Lazery i volokonnaya optika v biomeditsinskikh issledovaniyakh [Lasers and fiber optics in biomedical studies], IPR Media, Moscow, 2021 (in Russian).

3. **Mishchenko M. I., Mackowski D. W., Travis L. D.,** Scattering of light by bispheres with touching and separated components, Appl. Opt. 34 (21) (1995) 4589–4599.

4. **Mishchenko M. I., Travis L. D., Mackowski D. W.,** T-matrix computations of light scattering by nonspherical particles: A review, J. Quant. Spectrosc. Radiat. Transf. 55 (5) (1996) 535–575.

5. **Xu Y.,** Scattering Mueller matrix of an ensemble of variously shaped small particles, J. Opt. Soc. Am. A. 20 (11) (2003) 2093–2105.

6. **Doicu A., Wreidt T., Eremin Y.,** Light scattering by systems of particles. Null-field method with discrete sources: Theory and programs, Springer Series in Optical Sciences. Vol. 24. Springer-Verlag, Berlin, Heidelberg, 2006.

7. **Yurkin M. A., Hoekstra A. G.,** The discrete dipole approximation: An overview and recent developments, J. Quant. Spectrosc. Radiat. Transf., 106 (1–3) (2007) 558–589.

8. **Taflove A., Hagness S. C.,** Computational electrodynamics: The finite-difference time-domain method, Artech House, Boston, London, 2005.

9. **Mackowski D. W.,** Analysis of radiative scattering for multiple sphere configurations, Proc. R. Soc. Lond. Ser. Math. Phys. Sci. A: Math. Phys. Sci. 433 (1889) (1991) 599–614.

10. **Xu Y.,** Electromagnetic scattering by an aggregate of spheres, Appl. Opt. 34 (21) (1995) 4573–4588.

11. **Kulikov K. G., Radin A. M.,** Study of dispersion and absorption of an ensemble of spherical particles inside an optical cavity and new possibilities of predicting the optical characteristics of biological media by intracavity laser spectroscopy, Optics & Spectroscopy. 92 (2) (2002) 199–206.

12. **Moroz A.,** A recursive transfer-matrix solution for a dipole radiating inside and outside a stratified sphere, Ann. Phys. 315 (2) (2005) 352–418.

13. **Cruzan O. R.,** Translational addition theorems for spherical vector wave functions, Quart. Appl. Math. 20 (1) (1962) 33–40.

14. **Stein S.,** Addition theorems for spherical wave functions, Quart. Appl. Math. 19 (1) (1961) 15–24.

15. **Saad Y.,** Iterative methods for sparse linear systems. SIAM, USA, 2003.

16. **Van der Vorst H. A.,** Iterative Krylov methods for large linear systems, Cambridge University, Cambridge, 2003.

17. **Kulikov K. G., Koshlan T. V., Kontsevaya V. G.,** Programmnyy kompleks dlya rascheta opticheskikh kharakteristik na gruppe dielektricheskikh tel proizvolnoy formy. Programma dlya EVM [Software package for calculating optical characteristics on a group of dielectric arbitrary shaped bodies] No. 2022611755; 1200 p. Russian Federation; recorded in the Register of Federal Service on Intellectual Property, Patents and Trademarks 01.02.2022 (in Russian).

18. **Bohren C. F., Huffman D. R.,** Absorption and scattering of light by small particles, John Wiley & Sons, Inc., New-York, Toronto, 1998.

19.**Tikhonov A. N., Arsenin V. A.,** Metody resheniya nekorrektnykh zadach [Methods for solving ill-posed problems], Nauka, Moscow, 1979 (in Russian).

20. **Tikhonov A. N., Goncharskiy A. V., Stepanov V. V., Yagola A. G.,** Chislennyye metody resheniya nekorrektnykh zadach [Numerical methods for solving ill-posed problems], Nauka, Moscow, 1990 (in Russian).

21. **Steinke J. M., Shepherd A. P.,** Comparison of Mie theory and the light scattering of red blood cells, Appl. Opt. 27 (19) (1988) 4027–4033.

22. **Yaroslavsky A. N., Goldbach T., Schwarzmaier H.,** Influence of the scattering phase function approximation on the optical properties of blood determined from the integrating sphere measurements, J. Biomed. Opt. 4 (1) (1999) 47–53.

23. **Ustinov V. D.,** On inverse reconstruction problems of erythrocyte size distribution in laser diffractometry, Math. Models Comput. Simul. 9 (5) (2017) 561–569.

24. **Vismont F. I., Lemeshonok L. S., Poputnikov D. M.,** Patofiziologicheskiy analiz gemogramm i otsenka tipovykh narusheniy sistemy krovi [Pathophysiological analysis of haemogrammas and evaluation of typical disorders of the blood system], BGMU, Minsk, 2011 (In Russian).

25. **Dobbe J. G. G., Hardeman M. R., Streekstra G. J., et al.,** Analyzing red blood cell-deformability distributions, Blood Cells, Mol. Dis. 28 (3) (2002) 373–384.

26. **Brunsting A., Mullaney P. F.,** Differential light scattering from spherical mammalian cells, Biophys. J. 14 (6) (1974) 439–453.

27. **Zink D., Fischer A. H., Nickerson J. A.,** Nuclear structure in cancer cells, Nat. Rev. Cancer. 4 (9) (2004) 677–687.

СПИСОК ЛИТЕРАТУРЫ

1. **Тучин В. В.** Оптика биологических тканей. Методы рассеяния света в медицинской диагностике. М.: Ай Пи Ар Медиа, 2021. 802 с.

2. **Тучин В. В.** Лазеры и волоконная оптика в биомедицинских исследованиях. М.: Ай Пи Ар Медиа, 2021. 495 с.

3. **Mishchenko M. I., Mackowski D. W., Travis L. D.** Scattering of light by bispheres with touching and separated components // Applied Optics. 1995. Vol. 34. No. 21. Pp. 4589–4599.

4. **Mishchenko M. I., Travis L. D., Mackowski D. W.** T-matrix computations of light scattering by nonspherical particles: A review // Journal of Quantum Spectroscopy & Radiative Transfer. 1996. Vol. 55.No. 5. Pp. 535–575.

5. **Xu Y.** Scattering Mueller matrix of an ensemble of variously shaped small particles// Journal of the Optical Society of America. A. 2003. Vol. 20.No. 11. Pp. 2093–2105.

6. **Doicu A., Wreidt T., Eremin Y.** Light scattering by systems of particles. Null-field method with discrete sources: Theory and programs. Springer Series in Optical Sciences. Vol. 24. Berlin, Heidelberg: Springer-Verlag, 2006. 324 p.

7. **Yurkin M. A., Hoekstra A. G.** The discrete dipole approximation: An overview and recent developments // Journal of Quantum Spectroscopy & Radiative Transfer. 2007. Vol. 106. No. 1–3. Pp. 558–589.

8. **Taflove A., Hagness S. C.** Computational electrodynamics: the finite-difference time-domain method. Boston, London: Artech House, 2005. 997 p.

9. **Mackowski D. W.** Analysis of radiative scattering for multiple sphere configurations // Proceedings of the Royal Society A: Mathematical & Physical Sciences. 1991. Vol. 433. No. 1889. Pp. 599–614.

10. **Xu Y.** Electromagnetic scattering by an aggregate of spheres // Applied Optics. 1995. Vol. 34. No. 21. Pp. 4573–4588.

11. **Куликов К. Г., Радин А. М.** Исследование дисперсии и спектра поглощения совокупности сферических частиц в полости оптического резонатора и новые возможности прогноза оптических характеристик биологических сред методом внутрирезонаторной лазерной спектроскопии //Оптика и спектроскопия. 2002. Т. 92. № 2. С. 228–236.

12. **Moroz A.** A recursive transfer-matrix solution for a dipole radiating inside and outside a stratified sphere // Annals of Physics. 2005. Vol. 315. No. 2. Pp. 352–418.

13. **Cruzan O. R.** Translational addition theorems for spherical vector wave functions // Quarterly of Applied Mathematics. 1962. Vol. 20. No. 1. Pp. 33–40.

14. **Stein S.** Addition theorems for spherical wave functions // Quarterly of Applied Mathematics. 1961. Vol. 19. No. 1. Pp. 15–24.

15. **Saad Y.** Iterative methods for sparse linear systems. USA: SIAM, 2003. 535 p.

16. **Van der Vorst H. A.** Iterative Krylov methods for large linear systems. Cambridge: Cambridge University, 2003.194 p.

17. **Куликов К. Г., Кошлан Т. В., Концевая В. Г.** Программный комплекс для расчета оптических характеристик на группе диэлектрических тел произвольной формы. Программа для ЭВМ. № 2022611755. 1200 стр. Российская Федерация; зарегистрирована в реестре Федеральной службы по интеллектуальной собственности, патентам и товарным знакам 01.02.2022.

18. **Борен К., Хафмен Д.** Поглощение и рассеяние света малыми частицами. Пер. с англ. М.: Мир, 1986. 664 с.

19. **Тихонов А. Н., Арсенин В. А.** Методы решения некорректных задач. М.: Наука, 1979.285 с.

20. **Тихонов А. Н., Гончарский А. В., Степанов В. В., Ягола А. Г.** Численные методы решения некорректных задач. М.: Наука, 1990. 14 с.

21. **Steinke J. M., Shepherd A. P.** Comparison of Mie theory and the light scattering of red blood cells // Applied Optics. 1988. Vol. 27. No. 19. Pp. 4027–4033.

22. **Yaroslavsky A. N., Goldbach T., Schwarzmaier H.** Influence of the scattering phase function approximation on the optical properties of blood determined from the integrating sphere measurements// Journal of Biomedical Optics. 1999. Vol.4. No. 1. Pp. 47–53.

23. **Устинов В. Д.** Об обратных задачах восстановления распределения эритроцитов по размерам в лазерной дифрактометрии // Математическое моделирование. 2017. Т. 29. № 3. С. 51–62.

24. **Висмонт Ф. И., Лемешонок Л. С., Попутников Д. М.** Патофизиологический анализ гемограмм и оценка типовых нарушений системы крови. Минск: Изд. Белорусского государственного медицинского университета, 2011. 72 с.

25. **Dobbe J. G. G., Hardeman M. R., Streekstra G. J., Strackee J., Ince** C., **Grimbergen C. A.** Analyzing red blood cell-deformability distributions // Blood Cells, Molecules, and Diseases. 2002. Vol. 28. No. 3. Pp. 373–384.

26. **Brunsting A., Mullaney P. F.** Differential light scattering from spherical mammalian cells // Biophysical Journal. 1974. Vol. 14. No. 6. Pp. 439–453.

27. **Zink D., Fischer A. H., Nickerson J. A.** Nuclear structure in cancer cells // Nature Reviews Cancer. 2004. Vol. 4. No. 9. Pp. 677–687.

THE AUTHORS

KONTSEVAYA Vera G.
Pskov State University
2, Lenin Sq., Pskov, 180000, Russia
nkoncevoi@mail.ru
ORCID: 0000-0002-1434-5056

GOLOVITSKII Alexander P.
Peter the Great St. Petersburg Polytechnic University
29 Politechnicheskaya St., St. Petersburg, 195251, Russia
alexandergolovitski@yahoo.com
ORCID:0000-0003-4292-0959

KULIKOV Kirill G.
Peter the Great St. Petersburg Polytechnic University
29 Politechnicheskaya St., St. Petersburg, 195251, Russia
kulikov.kirill.g@gmail.com
ORCID: 0000-0002-4610-7394

СВЕДЕНИЯ ОБ АВТОРАХ

КОНЦЕВАЯ Вера Геннадьевна – *старший преподаватель кафедры математики и теории игр Псковского государственного университета.*
180000, Россия, г. Псков, пл. Ленина, д. 2.
nkoncevoi@mail.ru
ORCID: 0000-0002-1434-5056

ГОЛОВИЦКИЙ Александр Петрович – *доктор физико-математических наук, профессор Высшей инженерно-физической школы Санкт-Петербургского политехнического университета Петра Великого.*
195251, Россия, г. Санкт-Петербург, Политехническая ул., 29
alexandergolovitski@yahoo.com
ORCID:0000-0003-4292-0959

КУЛИКОВ Кирилл Геннадьевич – *доктор физико-математических наук, профессор Высшей школы биомедицинских систем и технологий Санкт-Петербургского политехнического университета Петра Великого.*

195251, Россия, г. Санкт-Петербург, Политехническая ул., 29

kulikov.kirill.g@gmail.com

ORCID: -0000-0002-4610-7394

Received 04.03.2022. Approved after reviewing 15.03.2022. Accepted 15.03.2022.

Статья поступила в редакцию 04.03.2022. Одобрена после рецензирования 15.03.2022. Принята 15.03.2022.

Original article
DOI: https://doi.org/10.18721/JPM.15109

THE MOTION OF A CHARGED PARTICLE IN THE ELECTROMAGNETIC FIELD OF A MULTITONAL AMPLITUDE-MODULATED WAVE AND IN THE CONSTANT MAGNETIC FIELD

G. F. Kopytov [1], *D.I. Kudryavtsev* [2] ✉

[1] Moscow State University of Technology and Management (The First Cossack University), Moscow, Russia;

[2] Kuban State University, Krasnodar, Russia

✉ dmitriy-kudryavtsev-2016@mail.ru

Abstract: This article presents the exact solution of the equation of motion for a charged particle in the electromagnetic field of circularly and linear polarized multitonal amplitude-modulated waves, as well in the presence of a constant uniform magnetic field. The motion of a charged particle in the both fields was analyzed and was expressed as dependences of its average kinetic energy on the electromagnetic waves' intensity, on their modulation percentage, on the modulation frequency-to carrier one ratio and on the constant magnetic field strength. The solution of the equation of the charged particle's motion in the electromagnetic field of the plane wave opens up opportunities for different applications related, in particular, to various developments of multifrequency lasers and laser modulation technology. This study was undertaken in connection with the wide practical use of high-temperature plasma.

Keywords: multitoned amplitude-modulated wave, charged particle, average kinetic energy, equation of motion

Citation: Kopytov G. F., Kudryavtsev D. I., The motion of a charged particle in the electromagnetic field of a multitonal amplitude-modulated wave and in the constant magnetic field, St. Petersburg Polytechnical State University Journal. Physics and Mathematics. 15 (1) (2022) 98–112. DOI: https://doi.org/10.18721/JPM.15109

Научная статья
УДК 539.12:537.63:537.868
DOI: https://doi.org/10.18721/JPM.15109

ДВИЖЕНИЕ ЗАРЯЖЕННОЙ ЧАСТИЦЫ В ЭЛЕКТРОМАГНИТНОМ ПОЛЕ МНОГОТОНАЛЬНОЙ АМПЛИТУДНО-МОДУЛИРОВАННОЙ ВОЛНЫ И ПОСТОЯННОМ МАГНИТНОМ ПОЛЕ

Г. Ф. Копытов [1], *Д. И. Кудрявцев* [2] ✉

[1] Московский государственный университет технологий и управления имени К. Г. Разумовского (Первый казачий университет), г. Москва, Россия;

[2] Кубанский государственный университет, г. Краснодар, Россия

✉ dmitriy-kudryavtsev-2016@mail.ru

Аннотация. Представлено решение уравнения движения заряженной частицы в электромагнитном поле циркулярно- и линейно-поляризованной многотональной амплитудно-модулированной волны, в присутствии постоянного однородного магнитного поля. Проанализировано движение заряженной частицы в этих полях и выражено в виде зависимостей ее средней кинетической энергии от интенсивности электромагнитных волн, глубины их модуляции, отношения частоты модуляции к несущей частоте, а также от напряженности постоянного магнитного поля. Решение уравнения движения заряженной частицы в поле плоской электромагнитной волны открывает возможности различных приложений, связанных, в частности, с современными разработками многочастотных лазеров и технологии лазерной модуляции. Предлагаемое исследование было проведено в связи с широким практическим применением высокотемпературной плазмы.

Ключевые слова: многотональная амплитудно-модулированная волна, заряженная частица, средняя кинетическая энергия, уравнение движения

Для цитирования: Копытов Г. Ф., Кудрявцев Д. И. Движение заряженной частицы в электромагнитном поле многотональной амплитудно-модулированной волны и постоянном магнитном поле // Научно-технические ведомости СПбГПУ. Физико-математические науки. 2022. Т. 15. № 1. С. 98–112. DOI: https://doi.org/10.18721/JPM.15109

Introduction

Large-scale studies have been carried out on acceleration of charged particles by interaction with the plasma of short laser pulses at high intensities of the order of 10^{22} W/cm^2 [1, 2]. For example, the question on the dynamics of a charged particle in the field of a monochromatic wave was raised as early as in the first half of the 20th century. A solution from the quantum standpoint was offered by Wolkow [3], the classical statement was later obtained independently by Frenkel [4], as well as by Landau and Lifshitz [5]. Thus, modifications were introduced to the problem over time. The solution for the equation of motion of an elementary particle in the field of a plane monochromatic wave was obtained in [6]. The more complicated particular cases when the laser emits a frequency or amplitude-modulated electromagnetic wave were further discussed in [7–9]. The effect from an externally applied constant magnetic field on such systems is also of considerable interest. Our studies [10–12] consider this specific issue.

The significance of our earlier and present studies is in the mathematical interpretation of this interaction, providing a description of the phenomenon using the parameters of electromagnetic radiation for the kinetic energy of the elementary particle. Particles with comparatively low energy characteristics find application in electron microscopy imaging, removal of malignant (cancer) cells and bacteria, X-ray generation. Particles with high energies above 1 MeV are interesting for studies into the structure of microobjects (clusters, atomic nuclei), the nature of fundamental forces, and other problems. Findings in this field therefore have major practical implications.

Attention should be paid to the simple frequency spectrum of the electromagnetic wave (EMW), assumed in [8, 9, 12], describing this electromagnetic wave as single-tone amplitude-modulated.

Our study differs from these works in that it considers the case when an amplitude-modulated EMW has a complex frequency spectrum, i.e., the analysis concerns a multitonal amplitude-modulated EMW most commonly found in applied problems, which also emphasizes the practical value of our results [13].

Our goal consisted in establishing the influence of a constant magnetic field on the dynamics and energy characteristics of a charged particle moving in the electromagnetic field of a multitonal amplitude-modulated wave.

Problem statement

The problem is formulated similarly to [12], accounting for the multitonal behavior of the EMW.

Amplitude modulation consists in varying such a parameter of the EMW as its amplitude over time. It is assumed that the amplitude $\mathbf{b}$ of the electromagnetic wave varies by the following harmonic law:

$$\mathbf{b}(\xi) = \mathbf{b}_{0\perp}\left(\sigma + \sum_{i=1}^{I} \delta_{\mathrm{AM}} \cos\tilde{\Phi}_i\right), \tag{1}$$

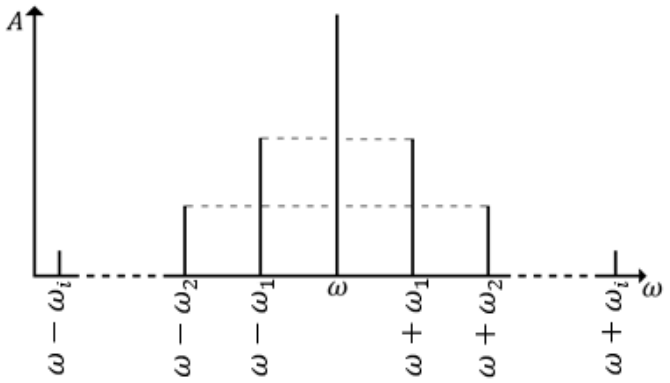

Fig. 1. Frequency spectrum of multitonal amplitude-modulated electromagnetic wave:
A, ω are its amplitude and carrier frequency, ω_i is the modulation frequency

where ξ is the spatio-temporal variable, $\xi = t - z/c$ (c is the speed of light); $\mathbf{b}_{0\perp} = \sqrt{b_{0x}^2 + b_{0y}^2}$; σ is the parameter of the EMW carrier frequency; δ_{AM} is the amplitude modulation depth; i, I are the index of the monochromatic wave and the number of waves; Φ is the full phase of the modulated EMW, $\tilde{\Phi} = \omega_i \xi + i\zeta_0$ (ω_i, s^{-1}, is the modulation frequency, ζ_0 is the initial phase of the amplitude-modulated EMW).

The quantity δ_{AM} characterizes the degree to which the amplitude of the electromagnetic wave varies provided that there is no overmodulation, $\delta_{\text{AM}} \in [0,1]$.

If the axis z is directed along the propagation path of the wave, the mathematical representation of the wave components can be written as follows:

$$\begin{gathered} E_x = H_y = b_{0_x}\left(\sigma + \sum_{\substack{i=-i \\ i\neq 0}}^{I} \delta_{\text{AM}} \cos\tilde{\Phi}_i\right)\cos\Phi, \\ E_y = -H_x = f b_{0_y}\left(\sigma + \sum_{\substack{i=-i \\ i\neq 0}}^{I} \delta_{\text{AM}} \cos\tilde{\Phi}_i\right)\sin\Phi, \\ E_z = H_z = 0, \end{gathered} \tag{2}$$

where b_{0x}, b_{0y} are the semi-axes of the polarization ellipse, coinciding with the axes x and y, where $b_{0x} \geq b_{0y} \geq 0$; ω is the carrier frequency of the EMW; f is the polarization parameter, $f = \pm 1$; the upper sign corresponds to the magnitude E_y of the right-handed polarization, the lower sign to left-handed polarization.

Now, in accordance with Eq. (2) and Fig. 1, we can determine the main difference between multi-tone and single-tone AM of a wave. The structure of such a wave is a superposition $2I + 1$ of monochromatic waves, consisting of waves with a carrier frequency ω and sideband frequencies $\omega - \omega_i$ and $\omega + \omega_i$ located symmetrically from the wave. The amplitudes of the sideband frequencies are equal and amount to $\mathbf{b}_{0\perp}/2$ of the carrier EWM amplitude. In the absence of overmodulation ($\delta_{\text{AM}} \leq 1$), the oscillation amplitude varies in the interval $\mathbf{b} = \mathbf{b}_{0\perp}/2\ (1 \pm \delta_{\text{AM}})$.

Momentum and coordinates of a charged particle moving in the electromagnetic field of a multitonal AM wave and the constant uniform magnetic field

The two major parameters of a charged particle are found through solving the equation of particle motion with mass m and charge q, taking the form

$$\frac{d\mathbf{p}}{dt} = q\left(\mathbf{E} + \frac{1}{c}\left[\mathbf{v}, \mathbf{H}_\Sigma\right]\right), \tag{3}$$

where $\mathbf{p}$ is the momentum of the particle, $\mathbf{v}$ is its velocity; $\mathbf{E}$ is the strength of the electrical component of the EM field, $\mathbf{H}_\Sigma = \mathbf{H} + \mathbf{H}_0$ ($\mathbf{H}$ is the strength of the magnetic component of the EM field, $\mathbf{H}_0$ is the strength of the constant magnetic field),

The solution to Eq. (3) takes the following form:

$$\begin{gathered} p_x = \frac{q b_{0x}}{\omega}\left(\sigma \sin\Phi + \sum_{\substack{i=-i \\ i\neq 0}}^{I} \eta_i \sin\dot{\tilde{\Phi}}_i\right) + \frac{qH_0}{c} y + \chi_x, \\ p_y = \mp \frac{q b_{0y}}{\omega}\left(\sigma \cos\Phi + \sum_{\substack{i=-i \\ i\neq 0}}^{I} \eta_i \cos\dot{\tilde{\Phi}}_i\right) - \frac{qH_0}{c} x + \chi_y, \\ p_z = \gamma g, \end{gathered} \tag{4}$$

where $\dot{\tilde{\Phi}}_i = (1+\alpha_i)\omega\xi + \varphi_0 + i\zeta_0$; φ_0 is the initial phase of the carrier wave;

$\eta_i = \dfrac{\delta_{AM}}{2(1+\alpha_i)}$; $\alpha_i = \omega/\omega_i$; χ_x, χ_y are the integration constants.

Notice that a substitution was introduced into the expression for the component p_z; we are going to use this substitution in the calculations below.

Thus, the quantity g takes the following form:

$$
\begin{aligned}
g = h - \frac{q^2\sigma^2\left(b_{0x}^2 - b_{0y}^2\right)}{4\gamma^2(\omega^2-\omega_c^2)}\cos 2\Phi - \frac{q^2\left(b_{0x}^2 - b_{0y}^2\right)}{4\gamma^2\omega^2}\sum_{\substack{i=-I\\ i\neq 0}}^{I}\frac{(\omega+\omega_i)^4}{\left[(\omega+\omega_i)^2-\omega_c^2\right]^2}\eta_i^2\cos 2\dot{\tilde{\Phi}}_i + \\
+R\frac{q\omega_c\sigma}{2\gamma c\left(\omega^2-\omega_c^2\right)}\Big[(\omega+\omega_c)\left(b_{0x}\mp b_{0y}\right)\cos(\Phi+\Phi_c) - \\
-(\omega-\omega_c)\left(b_{0x}\pm b_{0y}\right)\cos\left(\Phi-\Phi_c\right)\Big] + \\
+R\frac{q\omega_c}{2\gamma c\omega}\sum_{\substack{i=-I\\ i\neq 0}}^{I}\frac{\omega+\omega_i}{(\omega+\omega_i)^2-\omega_c^2}\eta_i\times \\
\times\Big\{\Big[(\omega+\omega_i)+\omega_c\Big]\left(b_{0x}\mp b_{0y}\right)\cos\left(\dot{\tilde{\Phi}}_i+\Phi_c\right) - \\
-\Big[(\omega+\omega_i)-\omega_c\Big]\left(b_{0x}\pm b_{0y}\right)\cos\left(\dot{\tilde{\Phi}}_i-\Phi_c\right)\Big\} + \\
+\frac{q^2\sigma}{2\gamma^2\omega\left(\omega^2-\omega_c^2\right)}\sum_{\substack{i=-I\\ i\neq 0}}^{I}\frac{\omega+\omega_i}{(\omega+\omega_i)^2-\omega_c^2}\eta_i\times \\
\times\Big\{\Big\{\Big[\omega(\omega+\omega_i)+\omega_c^2\Big]\left(b_{0x}^2+b_{0y}^2\right)\mp 2b_{0x}b_{0y}\omega_c(2\omega+\omega_i)\Big\}\cos(\Phi-\dot{\tilde{\Phi}}_i) - \\
-\Big[\omega(\omega+\omega_i)-\omega_c^2\Big]\left(b_{0x}^2-b_{0y}^2\right)\cos(\Phi+\dot{\tilde{\Phi}}_i)\Big\},
\end{aligned}
\tag{5}
$$

where h follows the expression

$$
\begin{aligned}
h = \frac{1}{2}\Big\langle\frac{m^2c^2}{\gamma^2} - 1 + \frac{q^2\sigma^2}{2\gamma^2}\frac{1}{\left(\omega^2-\omega_c^2\right)^2}\times \\
\times\Big[\left(\omega^2+\omega_c^2\right)\left(b_{0x}^2+b_{0y}^2\right)\mp 4b_{0x}b_{0y}\omega\omega_c\Big] + \\
+\frac{q^2}{2\gamma^2\omega^2}\sum_{\substack{i=-I\\ i\neq 0}}^{I}\frac{(\omega+\omega_i)^2}{\left[(\omega+\omega_i)^2-\omega_c^2\right]^2}\eta_i^2\times \\
\times\Big\{\Big[(\omega+\omega_i)^2+\omega_c^2\Big]\left(b_{0x}^2+b_{0y}^2\right)\mp 4b_{0x}b_{0y}(\omega+\omega_i)\omega_c\Big\} + \frac{R^2\omega_c^2}{c^2}\Big\rangle.
\end{aligned}
\tag{6}
$$

(ω_c is the cyclotron frequency, $\omega_c = qH_0/\gamma$, $\gamma = mc(1 - v_{0z}/c)/\sqrt{1 - v_0^2/c^2}$, R is a constant determined by the initial conditions.

Now that we have obtained the necessary expressions for the particle momentum, let us proceed to formulate the expressions for its coordinates.

For this purpose, we differentiate with respect to the variable ξ:

$$\dot{x} = \frac{qb_{0x}}{\gamma k}\left(\sigma \sin\Phi + \sum_{\substack{i=-I \\ i\neq 0}}^{I} \eta_i \sin\dot{\tilde{\Phi}}_i\right) + \omega_c y + \frac{\omega}{\gamma k}\chi_x, \tag{7}$$

$$\dot{y} = \mp\frac{qb_{0y}}{\gamma k}\left(\sigma \cos\Phi + \sum_{\substack{i=-I \\ i\neq 0}}^{I} \eta_i \cos\dot{\tilde{\Phi}}_i\right) - \omega_c x + \frac{\omega}{\gamma k}\chi_y, \tag{8}$$

where k is the magnitude of the wavevector, $k = \omega/c$.

We define the integration constants χ_x, χ_y by the following expressions:

$$\chi_x = -\frac{qb_{0x}}{\omega}\left(\sigma \sin\Phi_0 + \sum_{\substack{i=-I \\ i\neq 0}}^{I} \eta_i \sin\dot{\tilde{\Phi}}_{0i}\right) - \frac{cH_0}{\gamma} y_0 + \frac{mv_{0x}}{\sqrt{1-\frac{v_0^2}{c^2}}}, \tag{9}$$

$$\chi_y = \pm\frac{qb_{0y}}{\omega}\left(\sigma \cos\Phi_0 + \sum_{\substack{i=-I \\ i\neq 0}}^{I} \eta_i \cos\dot{\tilde{\Phi}}_{0i}\right) + \frac{cH_0}{\gamma} x_0 + \frac{mv_{0y}}{\sqrt{1-\frac{v_0^2}{c^2}}}. \tag{10}$$

Using Eqs. (5), (7), (8), we obtain expressions for the coordinates x, y, z:

$$x = R\cos\Phi_{\tilde{n}} - \frac{q}{\gamma k}\frac{b_{0x}\omega \mp b_{0y}\omega_c}{\omega^2 - \omega_c^2}\sigma\cos\Phi - \\ -\frac{q}{\gamma k}\sum_{\substack{i=-I \\ i\neq 0}}^{I}\frac{b_{0x}(\omega+\omega_i) \mp b_{0y}\omega_c}{(\omega+\omega_i)^2 - \omega_c^2}\eta_i \cos\dot{\tilde{\Phi}}_i + \frac{\omega}{\omega_c \gamma k}\chi_y + x_0, \tag{11}$$

$$y = R\sin\Phi_c + \frac{q}{\gamma k}\frac{b_{0x}\omega_c \mp b_{0y}\omega}{\omega^2 - \omega_c^2}\sigma\sin\Phi + \\ +\frac{q}{\gamma k}\sum_{\substack{i=-I \\ i\neq 0}}^{I}\frac{b_{0x}\omega_c \mp b_{0y}(\omega+\omega_i)}{(\omega+\omega_i)^2 - \omega_c^2}\eta_i \sin\dot{\tilde{\Phi}}_i - \frac{\omega}{\omega_c \gamma k}\chi_x + y_0, \tag{12}$$

$$z = z_0 + ch(\xi - \xi_0) - \frac{q^2\sigma^2(b_{0x}^2 - b_{0y}^2)}{8\gamma^2 k(\omega^2 - \omega_c^2)}\sin 2\Phi - \\ -\frac{q^2 c(b_{0x}^2 - b_{0y}^2)}{8\gamma^2\omega^2}\sum_{\substack{i=-I \\ i\neq 0}}^{I}\frac{\omega + \omega_i}{\left[(\omega+\omega_i)^2 - \omega_c^2\right]^2}\eta_i^2 \sin 2\dot{\tilde{\Phi}}_i + \\ +R\frac{q\sigma\omega_c}{2\gamma(\omega^2 - \omega_c^2)}\left[(b_{0x} \mp b_{0y})\sin(\Phi + \Phi_c) - (b_{0x} \pm b_{0y})\sin(\Phi - \Phi_c)\right] + \\ +R\frac{q\omega_c}{2\gamma\omega^2}\sum_{\substack{i=-I \\ i\neq 0}}^{I}\frac{\omega + \omega_i}{(\omega + \omega_i)^2 - \omega_c^2}\eta_i^2 \times \tag{13}$$

$$\times\left[\left(b_{0x}\mp b_{0y}\right)\sin\left(\dot{\tilde{\Phi}}_i+\Phi_c\right)-\left(b_{0x}\pm b_{0y}\right)\sin\left(\dot{\tilde{\Phi}}_i-\Phi_c\right)\right]+$$

$$+\frac{q^2\sigma c}{2\gamma^2\omega^2\left(\omega^2-\omega_c^2\right)}\sum_{\substack{i=-I\\ i\neq 0}}^{I}\frac{\omega\ +\ \omega_i}{\left(\omega\ +\ \omega_i\right)^2-\omega_c^2}\eta_i\times$$

$$\times\left\langle\left\{\left[\omega\left(\omega+\omega_i\right)+\omega_c^2\right]\left(b_{0x}^2+b_{0y}^2\right)\mp 2b_{0x}b_{0y}\omega_c\left(2\omega+\omega_i\right)\right\}\sin\left(\Phi-\dot{\tilde{\Phi}}_i\right)-\right.$$

$$\left.-\left\{\left[\omega\left(\omega+\omega_i\right)-\omega_c^2\right]\left(b_{0x}^2-b_{0y}^2\right)/\left(2+\omega_i/\omega\right)\right\}\sin\left(\Phi+\dot{\tilde{\Phi}}_i\right)\right\rangle,$$

where expression for z_0, depending on the initial conditions, has the form:

$$z_0=\frac{q^2\sigma^2\left(b_{0x}^2-b_{0y}^2\right)}{8\gamma^2k\left(\omega^2-\omega_c^2\right)}\sin 2\Phi_0+\frac{q^2c\left(b_{0x}^2-b_{0y}^2\right)}{8\gamma^2\omega^2}\sum_{\substack{i=-I\\ i\neq 0}}^{I}\frac{\omega\ +\ \omega_i}{\left[\left(\omega\ +\ \omega_i\right)^2-\omega_c^2\right]^2}\eta_i^2\sin 2\dot{\tilde{\Phi}}_{0i}-$$

$$-R\frac{q\sigma\omega_c}{2\gamma\left(\omega^2-\omega_c^2\right)}\left[\left(b_{0x}\mp b_{0y}\right)\sin\left(\Phi_0+\Phi_{0c}\right)-\left(b_{0x}\pm b_{0y}\right)\sin\left(\Phi_0-\Phi_{0c}\right)\right]-$$

$$-R\frac{q\omega_c}{2\gamma\omega^2}\sum_{\substack{i=-I\\ i\neq 0}}^{I}\frac{\omega\ +\ \omega_i}{\left(\omega\ +\ \omega_i\right)^2-\omega_c^2}\eta_i^2\times$$

$$\times\left[\left(b_{0x}\mp b_{0y}\right)\sin\left(\dot{\tilde{\Phi}}_{0i}+\Phi_{0c}\right)-\left(b_{0x}\pm b_{0y}\right)\sin\left(\dot{\tilde{\Phi}}_{0i}-\Phi_{0c}\right)\right]- \tag{14}$$

$$-\frac{q^2\sigma c}{2\gamma^2\omega^2\left(\omega^2-\omega_c^2\right)}\sum_{\substack{i=-I\\ i\neq 0}}^{I}\frac{\omega\ +\ \omega_i}{\left(\omega\ +\ \omega_i\right)^2-\omega_c^2}\eta_i\times$$

$$\times\left\langle\left\{\left[\omega\left(\omega+\omega_i\right)+\omega_c^2\right]\left(b_{0x}^2+b_{0y}^2\right)\mp 2b_{0x}b_{0y}\omega_c\left(2\omega+\omega_i\right)\right\}\sin\left(\Phi_0-\dot{\tilde{\Phi}}_{0i}\right)+\right.$$

$$\left.+\left\{\left[\omega\left(\omega+\omega_i\right)-\omega_c^2\right]\left(b_{0x}^2-b_{0y}^2\right)/\left(2+\omega_i/\omega\right)\right\}\sin\left(\Phi+\dot{\tilde{\Phi}}_i\right)\right\rangle.$$

Energy characteristics of a charged particle in the electromagnetic field of a multi-tone AM-wave and the constant uniform magnetic field

Obtaining the expressions for the momentum and coordinates of the particle moving in the field, we can start to calculate the energy characteristics of the elementary particle in the field of a multitonal AM wave and in the constant magnetic field; in this case, the initial phase should be averaged, similar to [7]. The corresponding mathematical calculations are given below:

$$\Psi=mc^2\left\langle h+\frac{1}{32\left(1+h\right)}\frac{q^4}{\gamma^4\omega^4}\left(b_{0x}^2-b_{0y}^2\right)\left\{\frac{1}{\left(1-\eta^2\right)^2}\sigma^4+\sum_{\substack{i=-I\\ i\neq 0}}^{I}\frac{\left(1+\alpha_i\right)^4}{\left[\left(1+\alpha_i\right)^2-\eta^2\right]^2}\eta_i^4\right\}+\right.$$

$$+\frac{q^2\sigma^2}{4\left(1+h\right)\gamma^2\omega^2\left(1-\eta^2\right)^2}\frac{R^2\omega_c^2}{c^2}\left[\left(1+\eta\right)^2\left(b_{0x}\mp b_{0y}\right)^2+\left(1-\eta\right)^2\left(b_{0x}\pm b_{0y}\right)^2\right]+ \tag{15}$$

$$\left.+\frac{q^2\sigma^2}{4\left(1+h\right)\gamma^2\omega^2}\frac{R^2\omega_c^2}{c^2}\sum_{\substack{i=-I\\ i\neq 0}}^{I}\frac{\left(1+\alpha_i\right)^2}{\left[\left(1+\alpha_i\right)^2-\eta^2\right]^2}\eta_i^2\times\right.$$

$$\times\left\{\left[\left(1+\alpha_i\right)+\eta\right]^2\left(b_{0x}\mp b_{0y}\right)^2+\left[\left(1+\alpha_i\right)-\eta\right]^2\left(b_{0x}\pm b_{0y}\right)^2\right\}+$$

$$+\frac{q^4\sigma^2}{8\left(1+h\right)\gamma^4\omega^4\left(1-\eta^2\right)^2}\sum_{\substack{i=-I\\ i\neq 0}}^{I}\frac{\left(1+\alpha_i\right)^2}{\left[\left(1+\alpha_i\right)^2-\eta^2\right]^2}\eta_i^2\times$$

$$\times\left\{\left[\left(1+\alpha_i+\eta^2\right)\left(b_{0x}^2+b_{0x}^2\right)\mp 2b_{0x}b_{0y}\eta\left(2+\alpha_i\right)\right]^2+\left(1+\alpha_i-\eta^2\right)^2\left(b_{0x}^2-b_{0x}^2\right)^2\right\}\Bigg\rangle,$$

where $\Psi = \bar{\varepsilon} - mc^2$ is the energy of the particle without taking into account its rest energy; $\eta = \omega_c/\omega$ is the ratio of the cyclotron to the carrier frequency of the wave.

The expression thus obtained characterizes the kinetic energy of the particle in the multitonal AM wave field and in the constant magnetic field.

Influence of a constant magnetic field on the energy characteristics of a particle moving in the electromagnetic field of a circularly and linearly polarized multitonal AM wave with zero initial velocity

After we derive the expression for the average kinetic energy of the particle, we should estimate the effect of the constant magnetic field on the energy characteristics of the particle moving in the field of a multitonal AM wave with zero initial velocity. Consider two particular cases of wave polarization: circular and linear. Then we have:

$$\mathbf{v}_0 = 0,\ \Phi(0) = \Phi_0 = -\frac{\omega}{c}z_0,\ \dot{\tilde{\Phi}}_i(0) = \dot{\tilde{\Phi}}_{0i} = -\frac{\omega}{c}\left(1+\alpha_i\right)z_0.$$

If we substitute expressions (9)–(10) into Eq. (5), we obtain:

$$h = \frac{R^2\omega_c^2}{c^2}+\frac{\mu}{4}\left\{\left(\frac{1\mp\eta}{1-\eta^2}\right)^2\sigma^2+\sum_{\substack{i=-I\\ i\neq 0}}^{I}\frac{\left(1+\alpha_i\right)^2\left[\left(1+\alpha_i\right)\mp\eta\right]^2}{\left[\left(1+\alpha_i\right)^2-\eta^2\right]^2}\eta_i^2\right\}, \tag{16}$$

where $\mu = \dfrac{q^2b^2}{\gamma^2\omega^2} = \dfrac{2q^2}{\pi m^2c^5}I\lambda^2$;

$$\frac{R^2\omega_c^2}{c^2} = \frac{\mu}{4}\Bigg\langle\left(\sigma^2+\sum_{\substack{i=-I\\ i\neq 0}}^{I}\eta_i^2\right)+\eta^2\left\{\frac{1+\eta^2}{\left(1-\eta^2\right)^2}\sigma^2+\sum_{\substack{i=-I\\ i\neq 0}}^{I}\frac{\left(1+\alpha_i\right)^2+\eta^2}{\left[\left(1+\alpha_i\right)^2-\eta^2\right]^2}\eta_i^2\right\}\pm$$

$$\pm 4\eta^3\frac{b_{0y}b_{0y}}{b_{0x}^2+b_{0y}^2}\left\{\frac{1}{\left(1-\eta^2\right)^2}\sigma^2+\sum_{\substack{i=-I\\ i\neq 0}}^{I}\frac{1+\alpha_i}{\left[\left(1+\alpha_i\right)^2-\eta^2\right]^2}\eta_i^2\right\}\Bigg\rangle. \tag{17}$$

Next, we assume that the multitonal AM wave has circular polarization; we then formulate the following conditions:

for circular polarization, $b_{0x} = b_{0y} = b/\sqrt{2}$;

for right-handed polarization,

$$\Psi = mc^2\frac{\mu}{2}\left\langle \frac{1}{2}\left(\sigma^2+\sum_{\substack{i=-I\\ i\neq 0}}^{I}\eta_i^2\right)+\frac{\eta^2}{2}\left\{\frac{1+\eta^2}{\left(1-\eta^2\right)^2}\sigma^2+\sum_{\substack{i=-I\\ i\neq 0}}^{I}\frac{\left(1+\alpha_i\right)^2+\eta^2}{\left[\left(1+\alpha_i\right)^2-\eta^2\right]^2}\eta_i^2\right\}-\right.$$
$$-\eta^3\left\{\frac{1}{\left(1-\eta^2\right)^2}\sigma^2+\sum_{\substack{i=-I\\ i\neq 0}}^{I}\frac{1+\alpha_i}{\left[\left(1+\alpha_i\right)^2-\eta^2\right]^2}\eta_i^2\right\}+$$
$$+\frac{1}{2}\left\{\frac{1}{\left(1-\eta^2\right)^2}\sigma^2+\sum_{\substack{i=-I\\ i\neq 0}}^{I}\frac{\left(1+\alpha_i\right)^2}{\left[\left(1+\alpha_i\right)^2-\eta^2\right]^2}\eta_i^2\right\}+$$
$$+\frac{\mu}{4(1+h)}\left\langle\left(\sigma^2+\sum_{\substack{i=-I\\ i\neq 0}}^{I}\eta_i^2\right)+\eta^2\left\{\frac{1+\eta^2}{\left(1-\eta^2\right)^2}\sigma^2+\sum_{\substack{i=-I\\ i\neq 0}}^{I}\frac{\left(1+\alpha_i\right)^2+\eta^2}{\left[\left(1+\alpha_i\right)^2-\eta^2\right]^2}\eta_i^2\right\}-\right. \tag{18}$$
$$\left.\left.-2\eta^3\left\{\frac{\sigma^2}{\left(1-\eta^2\right)^2}+\sum_{\substack{i=-I\\ i\neq 0}}^{I}\frac{1+\alpha_i}{\left[\left(1+\alpha_i\right)^2-\eta^2\right]^2}\eta_i^2\right\}\right\rangle\left\{\frac{\sigma^2}{\left(1-\eta\right)^2}+\sum_{\substack{i=-I\\ i\neq 0}}^{I}\frac{\left(1+\alpha_i\right)^2}{\left[\left(1+\alpha_i\right)-\eta\right]^2}\eta_i^2\right\}+\right.$$
$$\left.+\frac{\mu}{4(1+h)}\left(\frac{\sigma}{1-\eta}\right)^2\sum_{\substack{i=-I\\ i\neq 0}}^{I}\frac{\left(1+\alpha_i\right)^2}{\left[\left(1+\alpha_i\right)^2-\eta^2\right]^2}\eta_i^2\left[\left(1+\alpha_i\right)+\eta\right]^2\right\rangle;$$

for left-handed polarization,

$$\Psi = mc^2\frac{\mu}{2}\left\langle \frac{1}{2}\left(\sigma^2+\sum_{\substack{i=-I\\ i\neq 0}}^{I}\eta_i^2\right)+\frac{\eta^2}{2}\left\{\frac{1+\eta^2}{\left(1-\eta^2\right)^2}\sigma^2+\sum_{\substack{i=-I\\ i\neq 0}}^{I}\frac{\left(1+\alpha_i\right)^2+\eta^2}{\left[\left(1+\alpha_i\right)^2-\eta^2\right]^2}\eta_i^2\right\}-\right.$$
$$+\eta^3\left\{\frac{\sigma^2}{\left(1-\eta^2\right)^2}+\sum_{\substack{i=-I\\ i\neq 0}}^{I}\frac{1+\alpha_i}{\left[\left(1+\alpha_i\right)^2-\eta^2\right]^2}\eta_i^2\right\}+$$
$$+\frac{1}{2}\left\{\frac{\sigma^2}{\left(1+\eta^2\right)^2}+\sum_{\substack{i=-I\\ i\neq 0}}^{I}\frac{\left(1+\alpha_i\right)^2}{\left[\left(1+\alpha_i\right)^2+\eta^2\right]^2}\eta_i^2\right\}+ \tag{19}$$
$$+\frac{\mu}{4(1+h)}\left\langle\left(\sigma^2+\sum_{\substack{i=-I\\ i\neq 0}}^{I}\eta_i^2\right)+\eta^2\left\{\frac{1+\eta^2}{\left(1-\eta^2\right)^2}\sigma^2+\sum_{\substack{i=-I\\ i\neq 0}}^{I}\frac{\left(1+\alpha_i\right)^2+\eta^2}{\left[\left(1+\alpha_i\right)^2-\eta^2\right]^2}\eta_i^2\right\}+\right.$$
$$\left.+2\eta^3\left\{\frac{\sigma^2}{\left(1-\eta^2\right)^2}+\sum_{\substack{i=-I\\ i\neq 0}}^{I}\frac{1+\alpha_i}{\left[\left(1+\alpha_i\right)^2-\eta^2\right]^2}\eta_i^2\right\}\right\rangle\left\{\frac{\sigma^2}{\left(1+\eta\right)^2}+\sum_{\substack{i=-I\\ i\neq 0}}^{I}\frac{\left(1+\alpha_i\right)^2}{\left[\left(1+\alpha_i\right)+\eta\right]^2}\eta_i^2\right\}+$$

$$+\frac{\mu}{4(1+h)}\left(\frac{\sigma}{1+\eta}\right)^2\sum_{\substack{i=-I\\ i\neq 0}}^{I}\frac{(1+\alpha_i)^2}{\left[(1+\alpha_i)^2-\eta^2\right]^2}\eta_i^2\left[(1+\alpha_i)-\eta\right]^2\Bigg\rangle.$$

Analyzing the obtained expressions, we can conclude that the kinetic energies of the particle moving in the electromagnetic field of the multitonal AM wave with right-handed circular polarization differ considerably from those corresponding to the wave with left-handed polarization. According to the results presented in [8], such a difference is not observed in the absence of a constant magnetic field ($\eta = 0$).

Now suppose that the particle travels in the electromagnetic field of a linearly polarized multitonal AM wave, provided that the initial velocity of the particle equals zero. Then we can formulate the following conditions:

for linear polarization, $b_{0x} = b$; $b_{0y} = 0$;

$$\Psi = mc^2\frac{\mu}{4}\Bigg\langle\left(\sigma^2+\sum_{\substack{i=-I\\ i\neq 0}}^{I}\eta_i^2\right)+\theta+\frac{\mu}{2\sqrt{\theta\mu+4}\sqrt{\left[2\left(\sigma^2+\sum\limits_{\substack{i=-I\\ i\neq 0}}^{I}\eta_i^2\right)+\theta\right]\mu+4}}\Bigg\{\frac{\sigma^4}{\left(1-\eta^2\right)^2}+$$

$$+\left(\frac{2\sigma}{1-\eta^2}\right)^2\sum_{\substack{i=-I\\ i\neq 0}}^{I}\frac{(1+\alpha_i)^2\left[(1+\alpha_i)^2+\eta^4\right]}{\left[(1+\alpha_i)^2-\eta^2\right]^2}\eta_i^2+\sum_{\substack{i=-I\\ i\neq 0}}^{I}\frac{(1+\alpha_i)^4}{\left[(1+\alpha_i)^2-\eta^2\right]^2}\eta_i^4\Bigg\}+$$

$$+\left\{\frac{1+\eta^2}{\left(1-\eta^2\right)^2}\sigma^2+\sum_{\substack{i=-I\\ i\neq 0}}^{I}\frac{(1+\alpha_i)^2\left[(1+\alpha_i)^2+\eta^2\right]}{\left[(1+\alpha_i)^2-\eta^2\right]^2}\eta_i^2\right\}\times \tag{20}$$

$$\times\Bigg\langle\frac{4\mu}{\sqrt{\theta\mu+4}\sqrt{\left[2\left(\sigma^2+\sum\limits_{\substack{i=-I\\ i\neq 0}}^{I}\eta_i^2\right)+\theta\right]\mu+4}}\left\{\frac{\eta^2\left(1+\eta^2\right)\sigma^2}{\left(1-\eta^2\right)^2}+\sum_{\substack{i=-I\\ i\neq 0}}^{I}\frac{\eta^2\left[(1+\alpha_i)^2+\eta^2\right]}{\left[(1+\alpha_i)^2-\eta^2\right]^2}\eta_i^2\right\}+4-$$

$$-\frac{4\theta\mu+16}{\sqrt{\theta\mu+4}\sqrt{\left[2\left(\sigma^2+\sum\limits_{\substack{i=-I\\ i\neq 0}}^{I}\eta_i^2\right)+\theta\right]\mu+4}}\Bigg\rangle\Bigg\rangle,$$

where $\theta=\left(\frac{1+\eta^2}{1-\eta^2}\right)^2\sigma^2+\sum\limits_{\substack{i=-I\\ i\neq 0}}^{I}\left[\frac{(1+\alpha_i)^2+\eta^2}{(1+\alpha_i)^2-\eta^2}\right]^2\eta_i^2.$

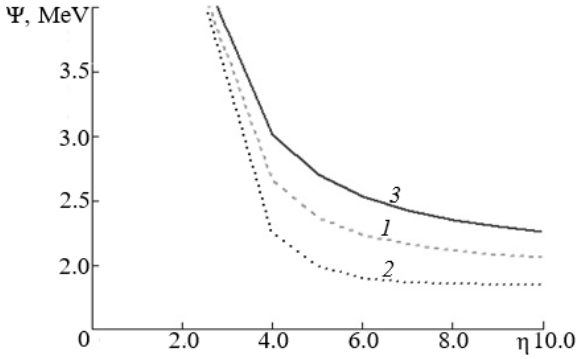

Fig. 2. Dependences of the difference Ψ on the magnitude of the magnetic field of multitonal AM EMW with linear polarization (*1*), right-handed (*2*) and left-handed (*3*) circular polarization; $I\lambda^2 = 10^{19}$ W·μm²/cm²; $\alpha_i = 1$; $\delta_{AM} = 1$

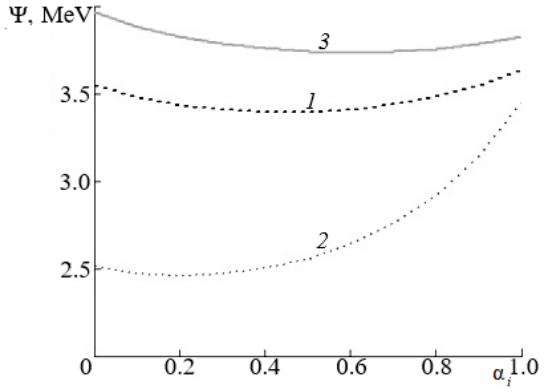

Fig. 3. Dependences of the difference Ψ on the ratio of the carrier to modulation frequency for the multitonal AM wave (the numbering of the curves is identical to that in Fig. 2); $I\lambda^2 = 10^{19}$ W·μm²/cm²; $\alpha_i \gg 1$; $\delta_{AM} = 1$

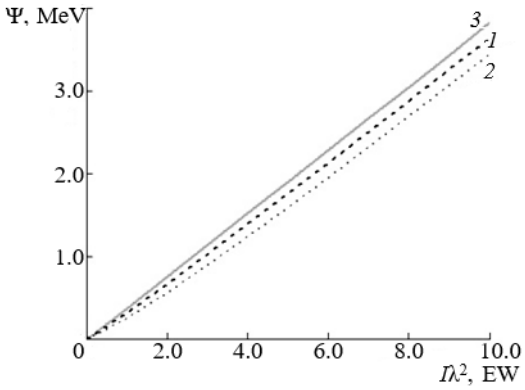

Fig. 4. Dependences of the difference Ψ on the intensity for the multitonal AM wave (the numbering of the curves is identical to that in Figs. 2 and 3); $\alpha_i = 1$; $\eta \gg 1$; $\delta_{AM} = 1$

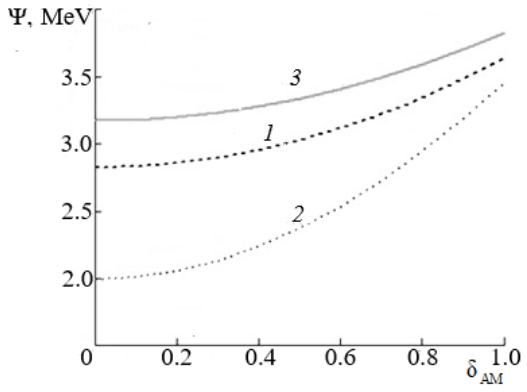

Fig. 5. Dependences of difference Ψ on the modulation depth for a multitonal AM wave (the numbering of the curves is identical to that in Figs. 2–4); $I\lambda^2 = 10^{19}$ W·μm²/cm²; $\alpha_i = 1$; $\eta \gg 1A$,

After obtaining expressions (18)–(20), we proceed to estimate the effect of a constant uniform magnetic field on the energy characteristics of the particle. Let us plot the dependence of Ψ on η (Fig. 2).

Consider also the dependences of Ψ on the quantities α_i, $I\lambda^2$, δ_{AM} (Fig. 3–5).

We can conclude from analyzing all of these dependences that the greatest energy corresponds to the case of particle motion in the wave field with right-handed circular polarization (Ψ_{right}), while the smallest energy corresponds to left-handed circular polarization (Ψ_{left}). The energy of the particle moving in the field of a linearly polarized wave (Ψ_{lin}) lies within the following range:

$$\Psi_{left} < \Psi_{lin} < \Psi_{right}.$$

Conclusion

To conclude, let us summarize our main findings:

we have given an estimate for the influence of a constant magnetic field by constructing the dependence of the particle's differential energy (without taking into account its rest energy) on the magnitude of the magnetic field;

we have obtained the dependences of energy Ψ on such parameters as α_i, $I\lambda^2$, δ_{AM} in the presence of a magnetic field ($\eta \gg 1$).

Notably, if the magnetic field is weak or zero ($\eta \ll 1$, $\delta_{AM} = 0$), all equations take the form of expressions for plane monochromatic electromagnetic waves, given in [6]. On the other hand, as the cyclotron frequency approaches the carrier one, the phenomenon of cyclotron self-resonance is observed, first observed and described by Kolomenskii and Lebedev in [14], as well as (independently) by Davydovskii [15]. Self-resonance is beyond the scope of this study, but a description of this phenomenon can be found, for example, in [16–18].

Thus, this paper continues our earlier studies [12], focusing on the problem of the influence of a constant magnetic field on the dynamics and energy characteristics of a charged particle in an externally applied field of a multitonal amplitude-modulated electromagnetic wave.

REFERENCES

1. **Galkin A. L., Galstyan A. M., Korobkin V. V., et al.,** Charged particle motion in the field of a short laser pulse of relativistic intensity, Bull. Lebedev Phys. Inst. 34 (3) (2007) 84–89.

2. **Galkin A. L., Kalashnikov M. P., Trofimov V. A.,** Angular distribution of electrons in the field of a short laser pulse of relativistic intensity, Bull. Lebedev Phys. Inst. 39 (8) (2012) 84–89.

3. **Wolkow D. M.,** Ьber eine Klasse von Lösungen der Diracschen Gleichung, Z. Phys. 94 (3–4) (1935) 250–260.

4. **Frenkel Ya. I.**, Sobraniye izbrannykh trudov v 3 tt., T. 1. Electrodinamika (Obshchaya teoriya elektrichestva) [Collection of selected works in 3 Vols., Vol. 1. Electrodynamics (General theory of electricity), Acad. Nauk SSSR Publishing, Moscow-Leningrad, 1956 (in Russian).

5. **Landau L. D., Lifshitz E. M.,** The classical theory of fields, Course of theoretical physics, Vol. 2, 4-th ed., Elsevier, USA,1980.

6. **Andreyev S. N., Makarov V. P., Rukhadze A. A.,** On the motion of a charged particle in a plane monochromatic electromagnetic wave, Quantum Electronics. 39 (1) (2009) 68–72.

7. **Kopytov G. F., Martynov A. A., Akintsov N. S.,** The motion of a charged particle in the field by a frequency-modulated electromagnetic wave, Nanosystems: Physics, Chemistry, Mathematics. 6 (5) (2015) 661–671.

8. **Kopytov G. F., Akopyan G. M., Glazkov A. A., Fotiev L. B.,** Investigation of the motion characteristics of a charged particle in the field of a circularly polarized amplitude-modulated electromagnetic wave, In: "Modern Problems of Physics, Biophysics and Infocommunication Technologies" (Multi-author book), CSTP, Krasnodar (5) (2016) 95–104 (in Russian).

9. **Kopytov G. F., Martynov A. A., Akintsov N. S.,** A charged particle moves in the field by a circularly amplitude-modulated electromagnetic wave, Ecological Bulletin of Research Centers of the Black Sea Economic Cooperation. (2) (2014) 39–43 (in Russian).

10. **Kopytov G. F., Martynov A. A., Akintsov N. S.,** The motion of a charged particle in the field of an electromagnetic wave and in the constant magnetic field, St. Petersburg State Polytechnical University Journal. Physics and Mathematics. (4 (206)) (2014) 55–63.

11. **Akintsov N. S., Isaev V. A., Kopytov G. F., Martynov A. A.,** The motion of a charged particle in the field by a frequency-modulated electromagnetic wave and in the constant magnetic field, St. Petersburg State Polytechnical University Journal. Physics and Mathematics. (4 (230)) (2015) 164–174 (in Russian).

12. **Kopytov G. F., Martynov A. A., Akintsov N. S.,** Motion of a charged particle in the field of a circularly polarized amplitude-modulated electromagnetic wave in the presence of a constant magnetic field, Russian Physics Journal. 58 (4) (2015) 508–516.

13. **Batura M. P., Kuznetsov A. P., Kurulev A. P.,** Teoriya electricheskikh tsepey [Theory of electrical circuits], Vysheyshaya Shkola Publishing, Minsk, 2015 (in Russian).

14. **Kolomenskii A. A., Lebedev A. N.,** Self-resonant particle motion in a plane electromagnetic wave, Dokl. Acad. Nauk SSSR. 145 (6) (1962) 1259–1261 (in Russian).

15. **Davydovskii V. Ya.,** Possibility of resonance acceleration of charged particles by electromagnetic waves in a constant magnetic field, Sov. Phys. JETF. 16 (1) (1963) 629–630.

16. **Milant'ev V. P.,** Cyclotron autoresonance and its applications, Phys. Usp. 40 (1) (1997) 1–14.

17. **Milant'ev V. P., Stepina S. P.,** Electron acceleration in the cyclotron autoresonance mode, Journal Dynamics of Complex Systems – XXI century. (4) (2009) 39–51 (in Russian).

18. **Abdulov N. A., Milant'ev V. P.,** The peculiarities of acceleration of ultra-relativistic electrons by the powerful laser radiation at the regime of cyclotron autoresonance, Discrete and Continuous Models and Applied Computational Science. (3) (2016) 66–78.

СПИСОК ЛИТЕРАТУРЫ

1. **Галкин А. Л., Галстян А. М., Коробкин В. В., Романовский М. Ю., Ширяев О. Б.** Движение заряженной частицы в поле короткого лазерного импульса релятивистской интенсивности // Краткие сообщения по физике ФИАН. 3 № .2007. С. 40–31.

2. **Галкин А. Л., Калашников М. П., Трофимов В. А.** Угловое распределение электронов в поле короткого лазерного импульса релятивистской интенсивности // Краткие сообщения по физике ФИАН. 8 № .2012. С. 42–35.

3. **Волков Д. М.** Электрон в поле плоских неполяризованных электромагнитных волн с точки зрения уравнения Дирака // Журнал экспериментальной и теоретической физики. 1937. Т. 11 № .7. С. 1289–1286.

4. **Френкель Я. И.** Собрание избранных трудов. В 3 тт. Т. 1. Электродинамика (Общая теория электричества). Москва-Ленинград: Изд-во АН СССР, 373 .1956 с.

5. **Ландау Л. Д., Лифшиц Е. М.** Теория поля. М.: Наука, 2012. 536 с.

6. **Андреев С. Н., Макаров В. П., Рухадзе А. А.** О движении заряженной частицы в плоской монохроматической электромагнитной волне // Квантовая электроника. 2009. Т. 39. № 1. С. 68 –72.

7. **Kopytov G. F., Martynov A. A., Akintsov N. S.** The motion of a charged particle in the field by a frequency-modulated electromagnetic wave // Nanosystems: Physics, Chemistry, Mathematics. 2015. Vol. 6. No. 5. Pp. 661–671.

8. **Копытов Г. Ф., Акопян Г. М., Глазков А. А., Фотиев Л. В.** Исследование характеристик движения заряженной частицы в поле циркулярно-поляризационной амплитудно-модулированной электромагнитной волны // Современные проблемы физики, биофизики и инфокоммуникационных технологий: Коллективная монография. Краснодар: ЦНТИ, 2016. № 5. С. 95–104.

9. **Копытов Г. Ф., Мартынов А. А., Акинцов Н. С.** Движение заряженной частицы в поле циркулярно-поляризованной амплитудно-модулированной электромагнитной волны // Экологический вестник научных центров Черноморского экономического сотрудничества. 2014. № 2. С. 39–43.

10. **Kopytov G. F., Martynov A. A., Akintsov N. S.** The motion of a charged particle in the field of an electromagnetic wave and in the constant magnetic field // St. Petersburg State Polytechnical University Journal. Physics and Mathematics. 2014. No. 4 (206). Pp. 55–63.

11. **Акинцов Н. С., Исаев В. А., Копытов Г. Ф., Мартынов А. А.** Движение заряженной частицы в поле частотно-модулированной электромагнитной волны и постоянном магнитном поле // Научно-технические ведомости Санкт-Петербургского государственного политехнического университета. Физико-математические науки. 230) 4 № .2015). С. 174–164.

12. **Копытов Г. Ф., Мартынов А. А., Акинцов Н. С.** Движение заряженной частицы в поле циркулярно-поляризованной амплитудно-модулированной электромагнитной волны и постоянном магнитном поле // Известия высших учебных заведений. Физика. 2015. Т. 4 № .58. С. 78–72.

13. **Батура М. П., Кузнецов А. П., Курулёв А. П.** Теория электрических цепей. Минск: Вышейшая школа, 606 .2015 с.

14. **Коломенский А. А., Лебедев А. Н.** Авторезонансное движение частицы в плоской электромагнитной волне // Доклады АН СССР. 1962. Т. 6 № .145. С. 1261–1259.

15. **Давыдовский В. Я.** О возможности резонансного ускорения заряженных частиц электромагнитными волнами в постоянном магнитном поле // Журнал экспериментальной и теоретической физики. 1962. Т. 43. № 3. С. 886–888.

16. **Милантьев В. П.** Явление циклотронного авторезонанса и его применения // Успехи физических наук. 1997. Т. 1 № .167. С. 16–3.

17. **Милантьев В. П., Степина С. П.** Ускорение электронов в режиме циклотронного авторезонанса // Динамика сложных систем – XXI век. 4 № .2009. С. 51–39.

18. **Абдулов Н. А., Милантьев В. П.** Особенности ускорения ультрарелятивистских электронов мощным лазерным излучением в режиме циклотронного авторезонанса // Вестник Российского университета дружбы народов. Серия: Математика, информатика, физика. 2016. № 3. С. 66–78.

THE AUTHORS

KOPYTOV Gennadiy F.
Moscow State University of Technology and Management (The First Cossack University)
73, Zemlyanoy Val St., Moscow, 109004, Russia
rektorat@mgutm.ru
ORCID: 0000-0003-1378-576X

KUDRYAVTSEV Dmitriy I.
Kuban State University
149 Stavropolskaya St., Krasnodar, 350040, Russia.
dmitriy-kudryavtsev-2016@mail.ru
ORCID: 0000-0003-3975-9025

СВЕДЕНИЯ ОБ АВТОРАХ

КОПЫТОВ Геннадий Филиппович – *доктор физико-математических наук, заведующий кафедрой физики Московского государственного университета технологий и управления имени К. Г. Разумовского (Первый казачий университет).*
109004, Россия, г. Москва, ул. Земляной вал, 73.
rektorat@mgutm.ru
ORCID: 0000-0003-1378-576X

КУДРЯВЦЕВ Дмитрий Игоревич – *магистрант физико-технического факультета Кубанского государственного университета.*
350040, Россия, г. Краснодар, Ставропольская ул., 149.
dmitriy-kudryavtsev-2016@mail.ru
ORCID: 0000-0003-3975-9025

Received 30.08.2021. Approved after reviewing 28.01.2022. Accepted 28.01.2022.
Статья поступила в редакцию 30.08.2021. Одобрена после рецензирования 28.01.2022. Принята 28.01.2022.